Electromagnetic Band Gap Technology for Millimetre Wave Applications

Memoria de la Tesis Doctoral realizada por

Iñigo Ederra Urzainqui

Dirigida por

Dr. Ramón Gonzalo García
Dr. Peter de Maagt

Para optar al grado de
Doctor Ingeniero de Telecomunicación

Nafarroako Unibertsitate Publikoa
Universidad Pública de Navarra

Departamento de Ingeniería Eléctrica y Electrónica
Pamplona, Septiembre 2004

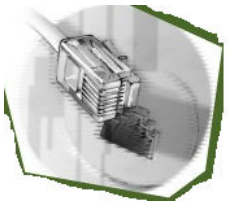

VI PREMIOS ROSINA RIBALTA

A los mejores proyectos de tesis doctoral en el ámbito de las Tecnologías de la Información y de las Comunicaciones

Este trabajo ha sido galardonado con el primer premio de la VI edición de los Premios Rosina Ribalta de la Fundación EPSON IBÉRICA al mejor proyecto de tesis doctoral en el ámbito de las Tecnologías de la Información y de las Comunicaciones. Año 2003-2004.

This work won the first award of the VI edition of the Rosina Ribalta Awards of the EPSON IBÉRICA Foundation to the best PhD thesis project within areas of Information Technologies and Communications. Year 2003-2004.

Agradecimientos/ Acknowledgments

Quisiera desde estas líneas recordar y agradecer a todas las personas que de alguna manera me han ayudado a llevar a cabo esta tesis...

A Ramón, más que un director de tesis un amigo. Gracias por tu apoyo durante estos años. Tu motivación y entusiasmo me han llevado hasta aquí.

Peter, thanks for giving me the opportunity to work with you at ESTEC, and for your advice and guidance. More important than all this, thanks for your friendship.

A los miembros del Grupo de Antenas. A los "históricos", Carlos, siempre dispuesto a apoyarnos y a ayudarnos en cualquier tema, Jorge, compañero en casi todo momento y lugar, y Bea, con quien es fácil combinar Maxwell y Woody... muchas gracias. También a las "nuevas generaciones", Juan Carlos, Ana Belén, Raúl, Diego, Elena, Asier,... gracias por vuestra paciencia, ya no acapararé más ordenadores...

Peter (Huggard), Byron, Luis, Bas, Martijn and Laurent, it has been a pleasure to work and learn with you.

The members of the Electromagnetics Division at ESTEC and of the MMT group at RAL, thanks for your support while working there. Thanks also to Axel Murk for carrying out the detector measurements and being such a friendly host.

A Carlos (Aristóteles), mi guía en el "lado oscuro" y a Eugenio, compañero de tantos buenos momentos.

Al resto de compañeros del departamento y en especial a Mónica, Javier, Miro, Jaione, Ixone, Armando... que habéis hecho tan agradable el rato de la comidas.

Arturo, Nicola, Andy, Peter, Marc, Iñigo, Pablo, David(es), Daniel, Belén, Eduardo, Aitor, Ramón, Elvira, Gloria, Santi(s), Nuria, Jaione... conseguisteis que sienta algo especial cada vez que vuelvo a Holanda.

Chris, Peter, Alfred, Marc, Jorge, Ruben, Alec, Alex, Dave, James, Luisa, Dario, Frank, Derek and Geoff, Startiger was a superb experience because of you.

A la fundación EPSON IBÉRICA por concederme el premio Rosina Ribalta, el último empujón para acabar esta tesis. También a la Universidad Pública de Navarra y al MEC por el apoyo económico.

A mis amigos de Isaba, gracias por acercarme el mundo "real"... y permitirme alejarme de él con vosotros.

A mis padres, Daniel y Amelia y a mi hermana, Anai, pese a la distancia siempre os he sentido a mi lado... gracias por dármelo todo.

Ya solo quedas tú, Ena... me has acompañado en este año tan complicado, nada hubiera sido igual sin ti... eskerrik asko.

Abstract

In this thesis the use of Electromagnetic Band Gap (EBG) structures in the millimetre-wave range has been studied. These frequencies are very suitable for imaging applications due to the different properties of the materials when compared with optical frequencies. The use of planar antennas for these applications, which would be the preferred option in terms of cost and fabrication complexity, can be limited by the losses due to the excitation of substrate modes. These problems could be overcome by using EBG technology, since these modes are inhibited in these periodic structures.

Although some preliminary demonstrations of the use of 3D EBG structures for antenna applications had already taken place, they can be considered mainly as proof-of-concepts. The aim of this thesis was to overcome this initial status and to use configurations based on this technology in the design of receivers. In particular, several aspects related with the RF design of millimetre-wave receivers implementing EBG technology have being studied.

First, the main features of EBG structures when used as substrates for dipole antennas have been analysed. Two EBG structures have been considered, namely the woodpile and the Fan structure. With respect to the dielectric materials used to build them, silicon and a high dielectric constant ceramic, Zr/Sn Titanate (ZTT), where selected. The use of a high dielectric constant material is of great interest, since it allows to reduce the size of the EBG structures and increases their bandwidth. The input impedance and the radiation pattern of the configurations have been studied for different positions of a dipole antenna on top of the EBG structures. Both features have been found to depend very strongly on the position and orientation of the dipole with respect to the dielectric and air areas of the EBG surface. Our studies also showed that the use of high dielectric constant ceramic materials does not lead to a decrease of the size of the radiating elements.

Based on these results, several configurations have been studied in detail

when fed by a Coplanar Stripline (CPS). Only those configurations which present high input impedance can be properly matched, since the CPS is a high characteristic impedance line. The effect of the losses of the dielectric materials has been studied and found to be negligible for these configurations.

In the previous results it became clear that it is difficult to find a configuration of dipole antenna on top of woodpile structure which presents simultaneously good matching and radiation features. Thus a modified woodpile structure has been proposed which improves notably both the radiation pattern and the matching of the initial configurations. The modification of the woodpile is easy to implement, since it is based on the displacement of the bars of the top most layer of the woodpile.

Finally, two receiver configurations implementing EBG technology have been designed: a direct detector and a subharmonic mixer. In both cases the radiating element consists of a dipole antenna placed on top of a silicon woodpile and the perpendicular solid-solid symmetry position was the selected radiating configuration due to its good radiation and matching features. For the direct detector, the design aimed at achieving the best sensitivity, while keeping a non-distorted radiation pattern. Prototypes of this configuration were fabricated and measured which showed good agreement with the predictions. With respect to the subharmonic mixer, it was designed to minimize its noise temperature. In this case, the minimum measured noise temperature was 950K, although some problems due to the presence of harmonic mixing were detected.

Resumen

En esta tesis se ha estudiado el uso de estructuras Electromagnetic Bandgap (EBG) para frecuencias en la banda de las millimétricas. Estas frecuencias son muy apropiadas para aplicaciones de generación de imágenes ("imaging") debido a las diferentes propiedades de los materiales con respecto a las que presentan a frecuencias ópticas. El uso de antenas planas para estas aplicaciones, el cual sería la opción preferida en cuanto a coste y complejidad de fabricación puede verse limitado debido a las pérdidas causadas por la excitación de ondas de sustrato. Estos problemas se pueden superar mediante el uso de la tecnología EBG, dado que dichos modos son inhibidos en estas estructuras periódicas.

A pesar de que algunas demostraciones preliminares del uso de la tecnología EBG para aplicaciones de antenas ya han tenido lugar, éstas pueden considerarse como meras pruebas de concepto. El propósito de esta tesis ha sido tratar de superar este estado inicial y utilizar configuraciones basadas en esta tecnología para el diseño de receptores. En particular, se han estudiado varios aspectos relacionados con el diseño de receptores a frecuencias de milimétricas implementando tecnología EBG.

Primeramente se han estudiado las características principales de los sustratos basados en tecnología EBG. Para ello, se han considerado dos estructuras EBG, el "woodpile" y la estructura de Fan. Con respecto a los materiales dieléctricos utilizados para su construcción, se han utilizado silicio y Titanato de Zr/Sn, ZTT. El uso de un material de elevada constante dieléctrica es de gran interés, ya que permite la reducción del tamaño del EBG y el aumento de su ancho de banda. Se han estudiado tanto la impedancia de entrada como el diagrama de radiación de las configuraciones para las diferentes posiciones de un dipolo sobre el substrato EBG. Se ha encontrado que ambas características dependen fuertemente de la posición y de la orientación del dipolo con respecto de las zonas dieléctricas y de aire en la superficie de la estructura EBG.

Así mismo, nuestros estudios han mostrado que el uso de materiales de alta constante dieléctrica no conlleva una disminución del tamaño de los elementos radiantes.

Basándonos en estos resultados, varias configuraciones han sido estudiadas con más detalle, siendo alimentadas por una línea Coplanar Stripline (CPS). Solamente aquellas configuraciones que presentan alta impedancia de entrada pueden ser adaptadas apropiadamente, dado que la línea CPS presenta alta impedancia característica. Así mismo, el efecto de la las pérdidas de los materiales ha sido estudiado para estas configuraciones, resultando ser despreciables.

Los resultados anteriores mostraron que es difícil encontrar una configuración de dipolo sobre "woodpile" que presente simultáneamente buenas características de radiación y adaptación. Por tanto, se ha propuesto una modificación de esta estructura EBG que mejora notablemente tanto el diagrama de radiación como la adaptación de la configuración inicial. Esta modificación es fácil de implementar, dado que se basa en el desplazamiento de las barras de la capa superior del woodpile.

Finalmente se han diseñado dos configuraciones de receptor implementando tecnología EBG: un detector directo y un mezclador subharmónico. En ambos casos el elemento radiante consiste en un dipolo colocado sobre un "woodpile" de silicio. En el caso del detector directo, el diseño trató de conseguir la máxima sensibilidad, manteniendo al mismo tiempo un diagrama de radiación no distorsionado. Se han fabricado diversos prototipos de estas configuraciones cuyas medidas están de acuerdo con las predicciones. Con respecto al mezclador subharmónico, se diseñó para minimizar su temperatura de ruido. En este caso la mínima temperatura de ruido medida fueron 950K, a pesar de que se detectaron ciertos problemas debido a la presencia de mezclado harmónico.

Contents

Chapter 1

Introduction

1.1 Background

Millimetre wave frequencies have long been recognised as potentially useful frequencies for passive imaging purposes. Although the resolution that can be achieved using these frequencies, given by its wavelength, is smaller than in the visible or the infrared ranges, millimetre wave frequencies present interesting properties which make them very suitable for imaging purposes [Yuj03].

First, the behaviour of most materials is different at millimetre frequencies than it is in the visible range. For instance, many materials which are opaque in the visible region of the spectrum, e.g. paper or clothes, become transparent at this frequency range. Moreover, metallic objects have a very clear signature when compared with dielectric objects. Based on these properties, passive security systems, such as those used in airports, can be developed [Sin01], which allow for the detection of concealed objects. Another application based on these properties can be found in the medical field, since e.g. the response of cancerous and healthy tissues is different [Woo03], which makes it possible to identify them at an earlier stage than it is with other techniques. Also caries could be detected by using this technology [Cra03].

Another advantage of the use of millimetre frequencies is related to the fact that attenuation through fog and other low visibility conditions is much lower for these frequencies than it is in the visible or the infrared region [Yuj03]. This property allows for the development of imaging systems capable of working in low visibility conditions. The applications of these systems in the automotive industry or in aviation are clear.

The realisation of these passive imaging systems can be based on different

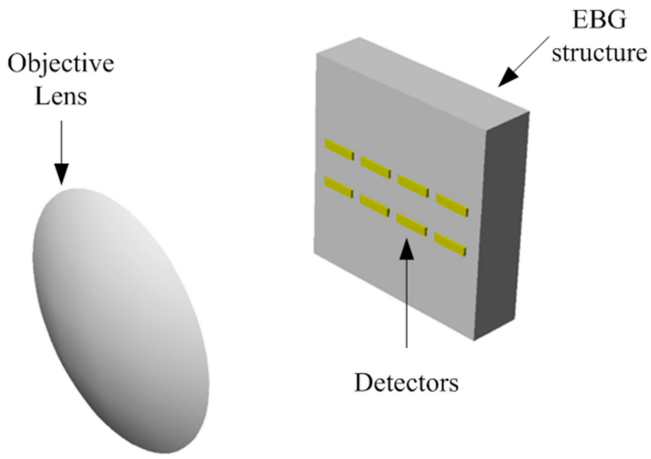

Figure 1.1: Focal plane imaging array configuration.

techniques [Let03] which according to the type of scanning technique can be classified as optical or electronic. In the first case lenses and/or mirrors are used to produce the scanning, whereas in the second one phased arrays or leaky wave antennas can be used to perform the scanning by changing the phase of the detecting elements or the frequency of operation.

In this thesis the first type of configuration will be considered. An schematic of these systems is shown in Figure 1.1. In this case a lens is used to focus the imaged object on the array of detectors placed at its focal plane. The design of these detectors is the objective of this work.

Traditionally, the design of these arrays was based on metallic waveguide technology [Tah83]. These components are expensive to manufacture and, since they are individually fabricated, have to be assembled together, which can be a source of errors and misalignments. These problems can be overcome by using integrated antennas [Reb92; SIQ93], since they are cheaper and the advances in photolithographic techniques allow for the fabrication of the whole array on the same substrate.

However, planar antennas are printed on dielectric substrates which suffer from substrate mode excitation when their thickness increases [Poz83]. In particular, at millimetre frequencies, it is difficult to find substrates thin enough so as to not suffer from substrate modes losses. Moreover, according to [Rut82], for a dipole antenna placed on top of a dielectric half-space the

ratio of the power radiated into the dielectric to the power radiated into the air scales as $\epsilon^{3/2}$. This means that if high dielectric constant materials, such as Si or GaAs, are used as substrate for the antennas, what would be appropriate for its integration with MMIC circuitry, the losses would be even higher. In order to overcome this problem, integrated lens antennas [Rut82] can be used, in which most of the radiation goes through the dielectric material. This approach has been extensively used with a variety of antennas: bow-tie [Rut82], log-periodic [Büt93], Yagi-Uda [Ueh92] and double slots [Fil93; vdV99].

Another technology which can alleviate the problems related with surface waves excitation is based on the use of EBG substrates [dM03; Ede03b; Gon01], in which no electromagnetic radiation can propagate. If a planar antenna is placed of top of the EBG substrate, it will act as a reflector and all the power will be radiated into the air. Moreover, these configurations will provide, in theory, the means to isolate individual pixels from their respective neighbours, which makes them appropriate for their use in imaging array applications [Ede04].

1.2 Electromagnetic Band Gap technology

Electromagnetic Band Gap (EBG) technology is based on the use of periodic structures in order to control the propagation of electromagnetic waves [Joa95]. By properly choosing the dimensions, material and shape of the scattering medium, configurations, where an electromagnetic wave cannot propagate within certain frequency bands, named as the bandgap, can be realised. Due to the analogy with the behaviour of electrons in semiconductors these materials were initially refered to as Photonic Band Gap (PBG) materials or Photonic Crystals (PC). Many people, especially in the microwave community, rejected this name [Oli99] and therefore the term Electromagnetic Band Gap material is now preferred and will be used in this dissertation.

Although the theory of periodic structures was already developed in the 40's [Bri46], interest in them grew considerably in the late 80's and beginning of the 90's after the demonstration of a tri-dimensional structure having a full bandgap was carried out [Joh87]. Due to the inherent scalability of Maxwell's equations, many applications have been proposed in different frequency ranges, from microwaves to optical frequencies.

However, the approaches followed to implement EBG structures in the different frequency regions are different. For instance for optical applications, the research is mainly focussed on the development of planar optical integrated

circuits, based on 2-dimensional (or quasi 2-dimensional) structures [SIQ02]. Using these 2D configurations various components, such as waveguides, bends and couplers have been developed.

Conversely, in the microwave regime, many implementations have been based on planar technologies, mainly microstrip [SIE99a]. In this frequency range EBGs have found its main use in the design of filters [Yan99] and antennas [dM03; Gon99]. As it was mentioned, for antenna applications the use of EBG technology brings advantages related to the suppression of substrate modes, which can degrade the performance of the antennas and reduce their efficiency [dM03; Gon99; Ede03a; Ede03b].

The use of microstrip technology in the millimetre and sub-millimetre ranges is limited due to its high losses. Therefore, other alternative EBG configurations have been proposed. In particular, for antenna applications, three-dimensional EBG structures have been used. In these configurations the antennas are placed on top of the EBG structure which acts as a reflector.

Several configurations combining planar antennas and three-dimensional EBG structures have been studied, showing improvements in the radiation features of the antenna, such as higher directivity and lower back-radiation [Bro93; Bro94; Bro96; Sig96; Kes96; Sig97; Leu97; Smi99; Gon01; Bur04]. Although only [Gon01] and [Bur04] performed their study at millimetre frequencies, the results at microwaves are scalable to higher frequencies. The EBG structures used in these experiments are the woodpile or layer-by-layer [Ho94; Söz94] and the Yablonovite [Yab91]. These structures, together with those proposed by the MIT group are shown in Figure 1.2

Besides the abovementioned configurations, other more elaborated designs have been proposed based on the use of resonant cavities [Bis01; The99; Che02]. They allow to obtain larger directivities, but at the expense of a more complex system. Based on them, new applications have been proposed, such as the design of multibeam antennas with overlapping feeds [Cha04].

With respect to the fabrication of systems based on EBG technology in the millimetre range, it may involve less processing steps than conventional micro machined solutions while preserving system performance. It is also foreseen that by using this technology it should be possible to make fully 3-dimensional circuitry allowing one to build more complex systems [Man03b], in which radiation, filtering, signal distribution and phase shifting may be realised within the same medium, with negligible losses. An example of these proposed configurations is shown in Figure 1.3, in which different types of waveguiding architectures are shown.

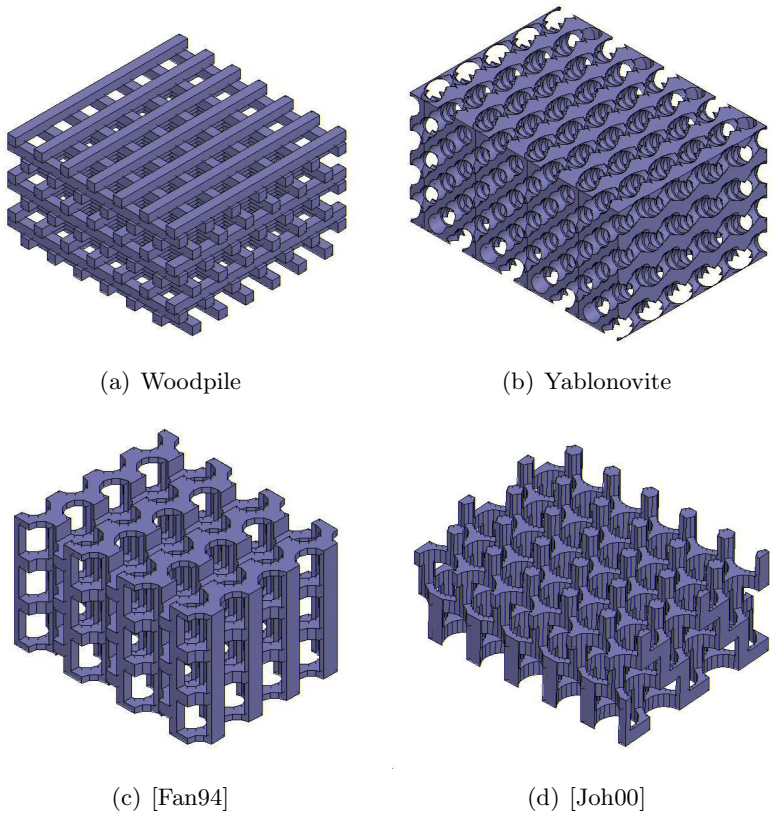

(a) Woodpile (b) Yablonovite

(c) [Fan94] (d) [Joh00]

Figure 1.2: Several three-dimensional EBG structures.

Another advantage of EBG technology is that it opens the possibility of using high dielectric constant materials. As it was mentioned, the losses due to surface waves excitation are very large in these materials. These losses can be avoided by using EBG structures, allowing for the design of more compact components based on these materials.

1.3 Framework of the research

This Ph.D. research has been carried out within the framework of an European Space Agency (ESA) contract entitled "Photonic Antenna Front-Ends: Photonic Crystals: Material selection and fabrication. RF design of a Photonic BandGap Antenna" (ESTEC Contract N 15632/01/NL/JA) in close

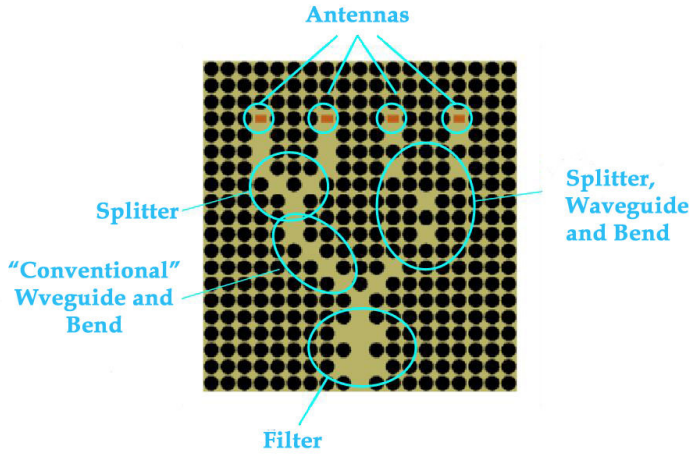

Figure 1.3: Schematic showing an integrated EBG system.

collaboration with the Rutherford Appleton Laboratory (RAL), UK, and the Eindhoven University of Technology (TU/e), The Netherlands.

This contract is a continuation of the contracts "Submm-wave Heterodyne Receiver and Integrated Antenna Technology Development, CCN5 and CCN6", in which the first demonstration of the improvements in the radiation pattern of a dipole antenna when placed on top of an EBG structure at millimetre wave frequencies was performed [Gon01].

In those proof-of-concept projects the sensitivity of the detectors was not optimised. Now, in this project the goal is to develop optimised detectors in terms of sensitivity, based on EBG technology. These detectors will be used to design an imaging array in the millimetre range (500 GHz).

Therefore, the project covers all the developments required to design this imaging array:

- development of modelling tools to predict the performance of EBG structures and of antennas placed on top of them;
- study and optimisation in terms of bandwidth of the different EBG structures suitable for application in the millimetre range;
- assessment of high dielectric constant materials;

- assessment of different fabrication technologies for the different EBG structures and materials;
- modelling of the properties of planar antennas placed on top of EBG structures;
- modelling of the properties and optimisation of the sensitivity of configurations based on the combination of planar antennas on EBG substrates and diode detectors;
- design and experimental verification of an 8 element imaging array implementing EBG technology.

In this contract the Universidad Pública de Navarra is the prime contractor of the project and responsible for the modelling and RF design, TU/e for the development of modelling tools and RAL for the manufacturing of EBG structures and circuits.

1.4 Scope of the thesis and survey of its contents

This thesis deals with the use of EBG technology for millimetre wave applications. In particular, the use of dipole antennas placed on top of EBG structures is studied in terms of matching and radiation features. Based on these results different detecting configurations are designed using the combination of dipole antennas and EBGs as radiating elements.

Configurations similar to those studied in this thesis, i.e. planar antennas placed on top of EBG structures, have been already presented [Bro93; Bro94; Bro96; Sig96; Kes96; Sig97; Leu97; Smi99; Gon01; Bur04]. However, in most cases the antennas used were ideal dipoles, not being printed on a substrate, as they would be the case in any real configuration. Moreover, in most cases only the radiation features were studied and when the matching was investigated, either the antennas were ideal [Sig97] or just the change in return loss was reported [Bur04]. Therefore, to our understanding, there was a lack on complete characterisation of this type of configurations that limited its use in any real application. This thesis will try to gain some insight into the behaviour of the combination of dipole antennas and EBG structures and based on it, use them to build detecting configurations which could be an alternative to the conventional front ends used in this frequency range.

With respect to the EBG structures, beside the woodpile, which has already been used as substrate for planar antennas, the Fan structure will be considered for the first time for this application. Moreover, the use of high dielectric constant ceramic materials to manufacture these EBG structures and its impact on the dipole performance will be studied. These materials, although very appealing due to the reduction in size that could be achieved by their use, have been hardly explored in the millimetre wave range due to the losses caused by the excitation of substrate modes. This problem does not exist for the EBG structures constructed out of these materials, since the excitation of substrate modes is inhibited in them. Besides, a modified woodpile will be proposed, which improves both the matching and the radiation features of a dipole placed on top of it.

The main contents of the thesis are organised as follows:

First, in Chapter 2 the main features of EBG structures when used as substrates for dipole antennas are studied. In this case, and as an initial stage dipoles without feeding lines printed on quartz substrates have been considered. Three different EBG structures have been studied: silicon and ceramic woodpile and so-called "Fan" structure. Firstly, the symmetry positions of each EBG structure have been identified, so that a dipole antenna could be placed at them keeping the symmetry of the radiation pattern. Dipole antennas have been placed at these positions and the input impedance and the radiation pattern obtained with each configuration have been investigated. The behaviour of the configurations has been found to depend very strongly on the dipole orientation with respect to the dielectric areas. In particular, some configurations have been found to be nearly "short-circuited" by the reflection at the EBG surface, being very difficult to match.

Based on the results obtained in Chapter 2, the matching of dipole antennas fed by Coplanar Striplines placed on top of EBG structures is studied in Chapter 3. Since Coplanar Striplines present high characteristic impedance only those dipole configurations which have a large enough input resistance can be easily matched. Examples of those configurations are given showing also the effect of the feeding lines on the radiation pattern of the configurations.

Since the radiation and matching features of a dipole antenna on top of an EBG structure depend very strongly on its position, a modified woodpile is proposed in Chapter 4, which allows obtaining simultaneously an improved radiation pattern and better matching. The modification proposed is easy to implement since it only affects to the first layer of bars.

A detector configuration using a Schottky diode as detecting element and a dipole placed on top of a silicon woodpile as antenna has been designed. The dipole was placed at the "perpendicular solid-solid" symmetry position, which showed the best compromise between radiation and matching features. The design process, together with the characterisation of the configuration in terms of radiation pattern and sensitivity are presented in Chapter 5.

A step forward is given in Chapter 6, focused on the design of an improved detecting configuration consisting of a subharmonic mixer using EBG technology. A dipole antenna placed on top of the woodpile is used to implement the radiating part of the receiver. The mixer design, fabrication and characterisation in terms of noise temperature and conversion loss are fully described.

Finally, in Chapter 7 the main results of this thesis are summarised and some guidelines for future research are given.

Chapter 2

Features of a dipole antenna on top of an EBG structure

2.1 Introduction

One of the proposed applications of EBG structures is their use as substrates for planar antennas. Since EBG structures do not allow the propagation of any electromagnetic wave if the operating frequency is inside the gap of the structure, they will act as a perfect reflector, avoiding the losses due to the excitation of substrate modes.

This chapter deals with the evaluation of the performance of a dipole antenna placed on top of different EBG structure. In particular the input impedance of the dipole and the resulting radiation pattern will be studied. The combination of planar antennas and 3-dimensional EBG structures has already shown to improve the radiation features of a dipole antenna [Bro93; Bro94; Bro96; Sig96; Kes96; Sig97; Leu97; Smi99; Gon01; Bur04]. In these references two different EBG structures were used, namely the woodpile structure [Ho94; Söz94] and the so-called Yablonovite [Yab91]. Due to their simplicity, dipole antennas were the preferred radiating elements, although slots [Leu97; Bur04] and bow-tie [Bro93] antennas have also been employed. Most of these studies were focussed on the radiation features of the configurations. In all cases, the directivity of the configurations increased with respect to the isolated radiating element and the back radiation was reduced.

However, in most of these studies the radiating configurations were ideal, i.e. dipole or slot antennas without substrate or feeding lines, instead of more

real configurations, based on printed antennas. In [Bur04] a slot antenna printed on silicon is studied, but only the change of the antenna matching when it is placed on top of the EBG is observed. In the other cases in which the input impedance of the antenna was analysed [Sig99; Smi99], the studies considered ideal configurations in which the dipole was at a certain height over the EBG structure, without a substrate to support it. Therefore, to our understanding, there was a lack of complete studies of the radiating features of configurations consisting of a printed antenna on top of an EBG.

In this chapter and as an inital stage towards the study of dipoles fed by Coplanar Striplines, dipole antennas printed on quartz substrates and placed on top of EBG structures will be analysed. Since in our case the matching performance of the antennas is very important in order to improve the efficiency of the detectors, a study will be carried out, focussing not only on the radiation features but also on their input impedance. In particular, since the characteristic impedance of a Coplanar Stripline is quite high we would be interested in finding configurations which comply with this feature.

2.1.1 EBG structures

As it was mentioned in Chapter 1, this thesis focuses on three-dimensional EBG structures. In particular, two different EBG structures have been considered, the woodpile or layer-by-layer [Ho94; Söz94] and Fan's structure [Fan94]. The names woodpile and Fan structure will be used along this thesis to make reference to them.

For the sake of compactness, both of them will be constructed out of a very high dielectric constant material. In particular, Zr/Sn Titanate, ZTT, with $\epsilon_r = 37$ [HB03] will be the selected ceramic material. In the case of the woodpile structure, also silicon will be used, since its fabrication procedures can be relatively simple [Gon02].

Increasing the dielectric constant of the constituents of an EBG structure has two effects on its performance. First, the width of the band gap increases provided that the dielectric contrast is larger. Second, the normalised frequency of the gap decreases. This means that the dimensions of the resulting configuration are smaller. Both effects are of great interest since more compact, broader band devices can be designed using these materials.

In the case of the three EBG structures considered, this effect can be observed in Figure 2.1 and Table 2.1. The size of the woodpile structure has been greatly reduced by the use of the high dielectric constant material and

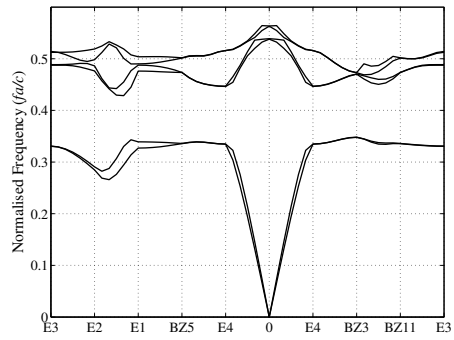

(a) Si woodpile

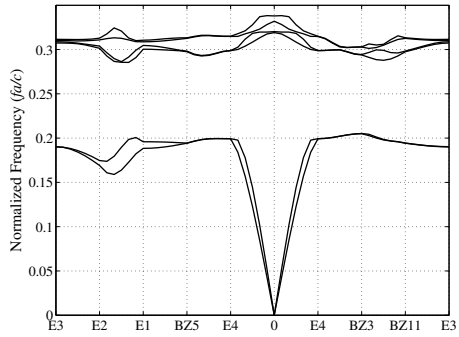

(b) ZTT woodpile

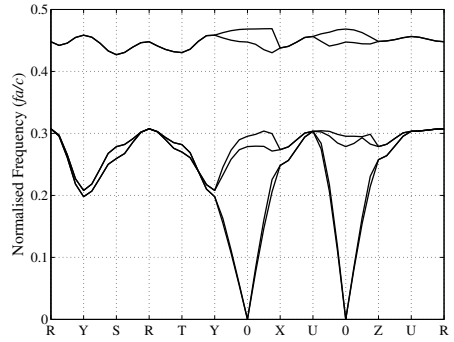

(c) ZTT Fan

Figure 2.1: Band diagram of the used EBG structures.

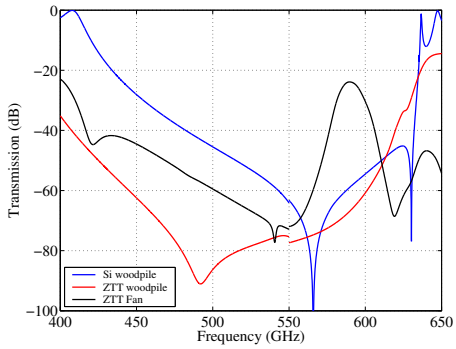

Figure 2.2: Transmission through 3 periods of the used EBG structures.

its bandwidth has also increased. Regarding Fan structure, its bandwidth is similar to that of the ZTT woodpile [Mar04]. However, its bandgap takes place at a much higher normalised frequency, very close to that of the Si woodpile. Thus, the dimensions of both EBG structures are similar.

A comparison between the performance of the three EBG structures is presented in Figure 2.2, where transmission through 3 periods of the structures is shown. The lowest transmission corresponds to the ZTT woodpile, which at 500 GHz is lower than -85 dB. For the Fan structure and the Si woodpile values of -60 dB and -45 dB are respectively achived.

Photographs of manufatured prototypes of the three EBG structures with central frequency of the gap at 500 GHz are shown in Figure 2.3. For each of the EBG structures, its symmetries will be discussed, since they are important in order to achieve symmetric radiating configurations. Once the symmetry positions of each structure have been identified, a planar dipole will be placed

EBG	**Normalised frequency**	**Fractional bandwidth (%)**	$\boldsymbol{a}$ **(**$\boldsymbol{\mu m}$**)**
Si woodpile	0.3882	21.0	232.9
ZTT woodpile	0.2350	32.8	141.0
ZTT Fan	0.3692	32.5	221.5

Table 2.1: Normalised frequency of the gap, fractional bandwidth and size of the used EBG structures.

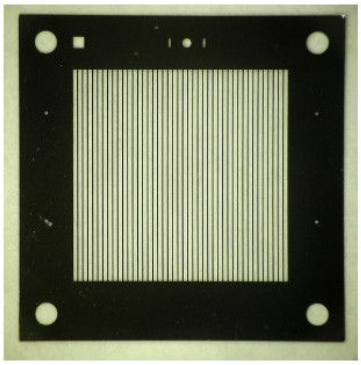

(a) Si woodpile, top view

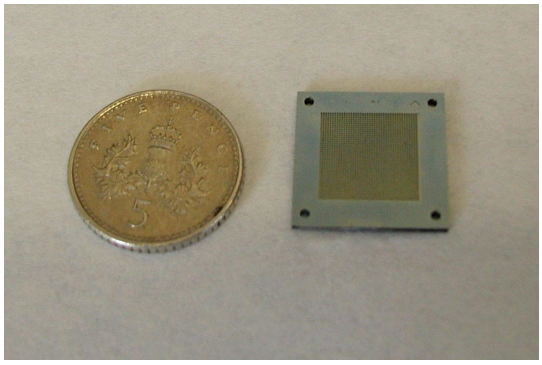

(b) Si woodpile

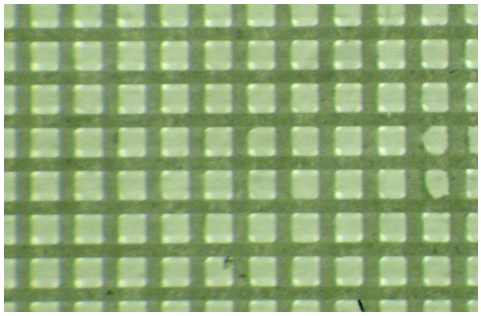

(c) ZTT woodpile, top view

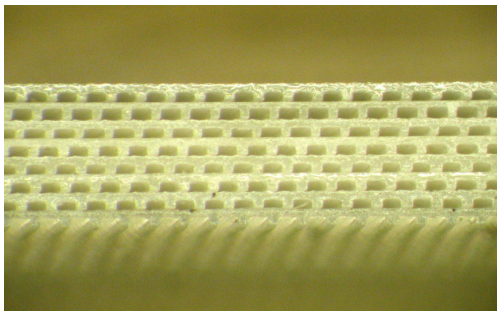

(d) ZTT woodpile, lateral view

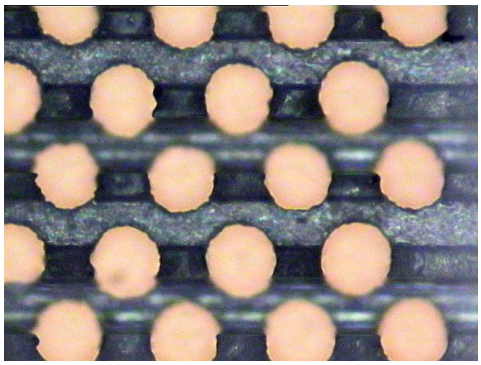

(e) ZTT Fan, top view

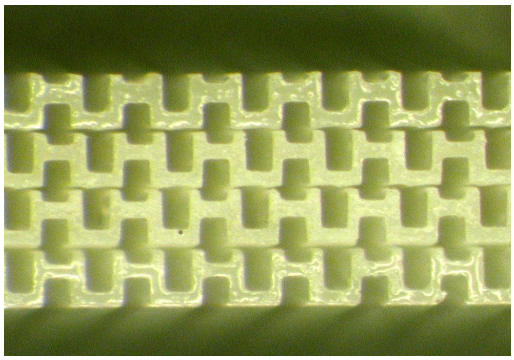

(f) ZTT Fan, lateral view

Figure 2.3: Photographs of different prototypes of EBG structures in the millimetre range.

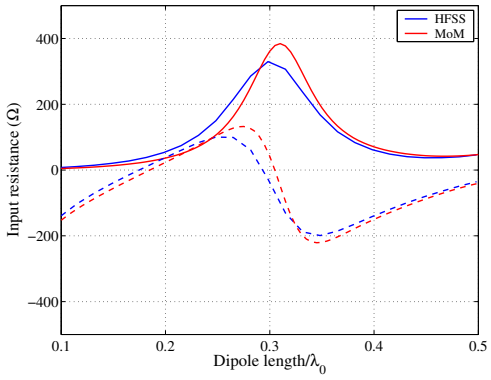

Figure 2.4: Comparison between the input impedance ($R_i + jX_i$) obtained with HFSS and using the Method of Moments [vdV99]. The solid line represents the input resistance (R_i) and the dashed line the input reactance (X_i).

on top of the EBG structures in each of these positions and both the input impedance and its radiation features will be studied.

2.1.2 HFSS validation

In order to validate the input impedance results obtained with Ansoft HFSS, a planar dipole antenna on top of a semi-infinite dielectric substrate was analysed. The dielectric constant of the substrate was 12.8. The dipole width was $0.02L$, where L is the dipole length. The results obtained are compared with those obtained using the Method of Moments (MoM) [vdV99]. The first resonant length and the input impedance at resonance obtained in both cases are compared in Table 2.2. Although there is a small shift in the resonant length, both results are in good agreement.

	l_r/λ_0	$R_i\,(\Omega)$)
HFSS	0.175	34.1
MoM	0.185	27.0

Table 2.2: Resonant lengths (l_r) and input resistance at resonance (R_i) of a the test configuration obtained with HFSS and the Method of Moments (MoM).

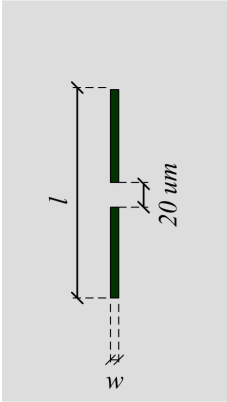

Figure 2.5: Dimensions of the printed dipole configuration. The grey area represents the substrate.

2.2 Dipole printed on quartz glass

The aim of this chapter is to study the performance of a dipole antenna printed onto a quartz substrate when placed on top of different EBG structures. For the sake of comparison, first the results obtained for a dipole antenna printed on a quartz substrate and without EBG structure will be shown. The dipole is fed by a lumped gap source ($Z_0 = 170\,\Omega$) placed between the dipole arms. The gap between the arms of the dipole is 20 microns, which corresponds to the gap between the strips of a Coplanar Stripline with approximately the characteristic impedance used in the lumped gap source. The dielectric constant of the quartz glass has been taken as 3.78. Finally, the width of the dipole, w, was taken arbitrarily as 10 microns. See Figure 2.5 for a description of the dipole parameters.

Configurations using different thickness of the quartz substrate were analysed, namely 20, 30 and 40 microns and an infinitely thick substrate. For each of them the dipole length was varied and the input impedance and the radiation pattern at 500 GHz where computed using Ansoft HFSS.

2.2.1 Input impedance

The effect of the substrate thickness and the dipole length on the input impedance of the dipole is shown in Figure 2.6. The input impedance depends very strongly on its length. The lengths corresponding to the first

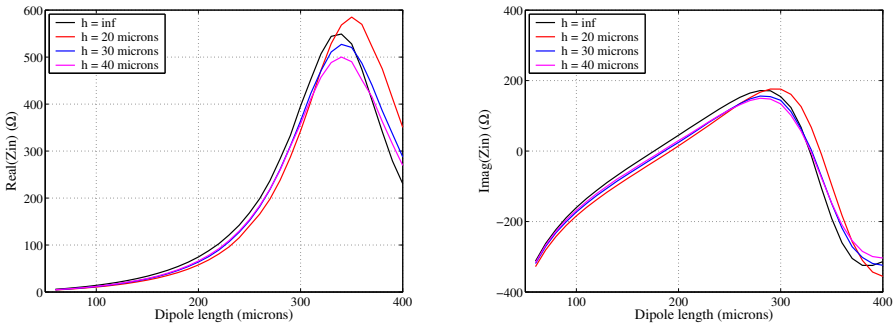

(a) R_i (b) X_i

Figure 2.6: Input impedance ($R_i + jX_i$) of a dipole printed on a quartz substrate as a function of its length and of the substrate thickness, h.(a) Real part; (b) Imaginary part.

two resonances are shown in Table 2.3. As it was expected the resonance length decreases when the thickness of the quartz substrate increases, due to the higher effective dielectric constant. This holds for both the first and the second resonances.

Since the configurations we are analysing are rather simple, approximated analytical solutions can be used to further check the accuracy of our results. In particular, the resonant length of a dipole antenna printed on a semi-infinite substrate can be calculated as $0.48A\lambda_0$ [Kra88],where the correction factor A for a flat element of width w and length L on a dielectric interface is $A = \frac{1}{\sqrt{1+\epsilon_e}(1+w/L)}$ and $\epsilon_e = \frac{1+\epsilon_{r,quartz}}{2}$, and $\epsilon_{r,quartz}$ is the dielectric constant of quartz. Using these expressions a resonant length of 183 microns was obtained,

$h\,(\mu m)$	$l_{r,1}\,(\mu m)$	$R_{i,1}\,(\Omega)$	$l_{r,2}\,(\mu m)$	$R_{i,2}\,(\Omega)$
20	192.2	50.7	339	564
30	186.4	50.9	330	511
40	183.8	50.5	329	485
inf	176.1	51.2	328	537

Table 2.3: Resonant lengths (l_r) and input resistance at resonance (R_i) of a dipole antenna printed on a quartz substrate.

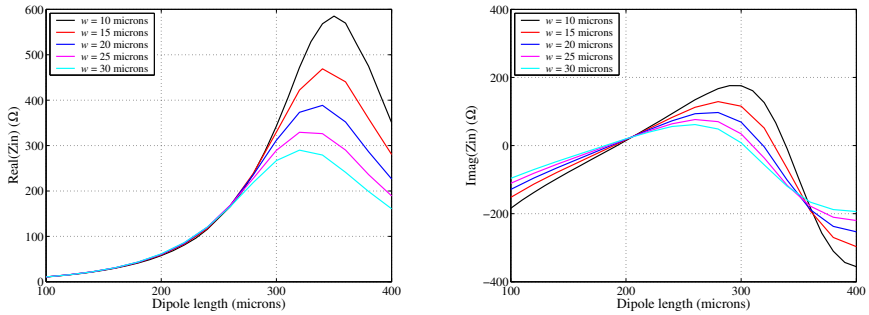

(a) R_i (b) X_i

Figure 2.7: Input impedance ($R_i + jX_i$) of a dipole printed on a 20 microns thick quartz substrate as a function of its length and width.(a) Real part; (b) Imaginary part.

not far from the result obtained in our simulations.

The results above were obtained using a 10 microns wide dipole. If the width of the dipole is different the input impedance changes as it is shown in Figure 2.7. These results correspond to a dipole printed onto a 20 microns substrate. They agree with the results obtained for a cylindrical dipole as the peak at the parallel resonance becomes less pronounced when the width of the dipole increases [Bal97]. Since the change in impedance is smaller, the bandwidth increases. Also the reactance curves cross when the dipole is half a wavelength, as it happens for cylindrical dipoles [Bal97].

2.2.2 Radiation features

The radiation patterns obtained for dipoles of different lengths printed onto quartz substrates of different thickness are presented in Figure 2.8. If the substrate is finite, the radiation patterns are similar to the radiation pattern of an ideal dipole, although the H-plane is not a perfect circle due to the substrate influence. This asymmetry causes the radiation pattern to be more directive in the endfire direction than at boresight. As it was mentioned in the introduction, for an infinitely thick substrate the dipole radiates mainly in the substrate. In theory, this effect should increase with its dielectric constant.

The effect of the change in the length of the dipole on its radiation pattern is quite small. For lengths smaller than the dipole first resonance, the radiation pattern slightly changes. If the dipole is longer than half a wavelength, the

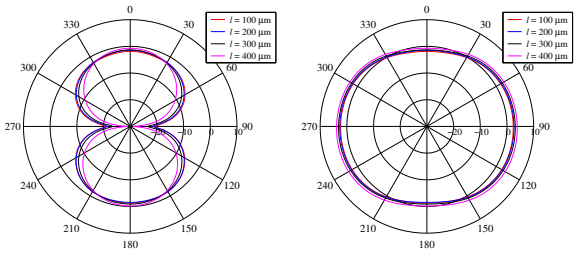

(a) $h = 20$ microns (b) $h = 20$ microns

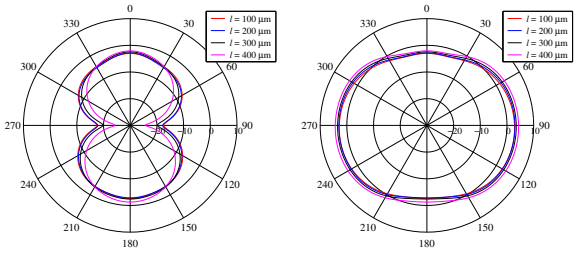

(c) $h = 30$ microns (d) $h = 30$ microns

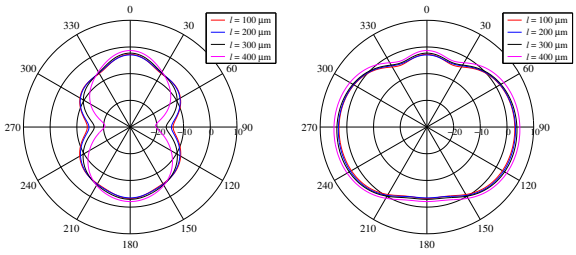

(e) $h = 40$ microns (f) $h = 40$ microns

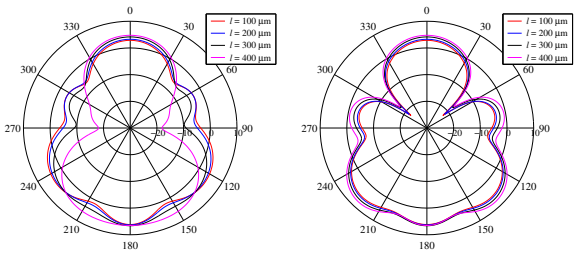

(g) $h = inf$ (h) $h = inf$

Figure 2.8: Radiation pattern of a dipole printed on a quartz substrate as a function of its length and of the substrate thickness, h. $f = 500$ GHz.

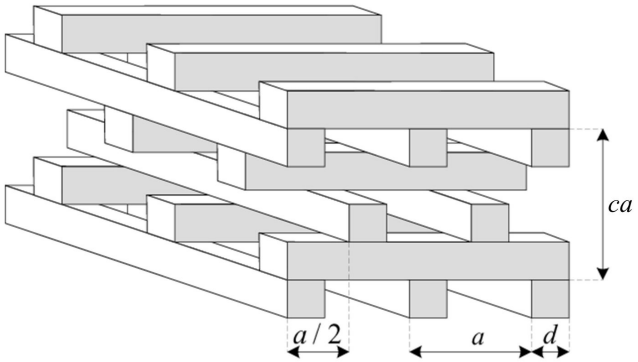

Figure 2.9: Geometry of the woodpile structure.

radiation pattern starts to be more directive. These results agree with the basic antenna theory that states that for dipoles shorter than half a wavelength the radiation pattern hardly changes [Bal97].

2.3 Dipole on top of a silicon woodpile structure

2.3.1 Description of the woodpile structure and symmetry considerations

The first structure that will be studied is the silicon woodpile. This structure is a good candidate for this frequency range, since it is robust and the manufacturing processes involved in its fabrication using silicon are well-known and can be relatively straightforward [Gon02; Azc03]. The parameters that define the woodpile structure are shown in Figure 2.9. They can be optimize in order to achieve the largest bandwidth, which for silicon is 21% [Mar04].

Taking into account the woodpile symmetries, there are 8 different positions that will keep the symmetry of the radiation pattern of a dipole antenna placed on top of this type of EBG structure, see Figure 2.10. These symmetry positions can be classified according to the dipole orientation with respect to the top layer of bars, i.e. “parallel” or “perpendicular”, and to the position of the centre of the dipole with respect to the bars of the two upper layers of the woodpile. In the last case the positions are labelled as “void” if the dipole centre is on air or “solid” in case it is on a dielectric bar.

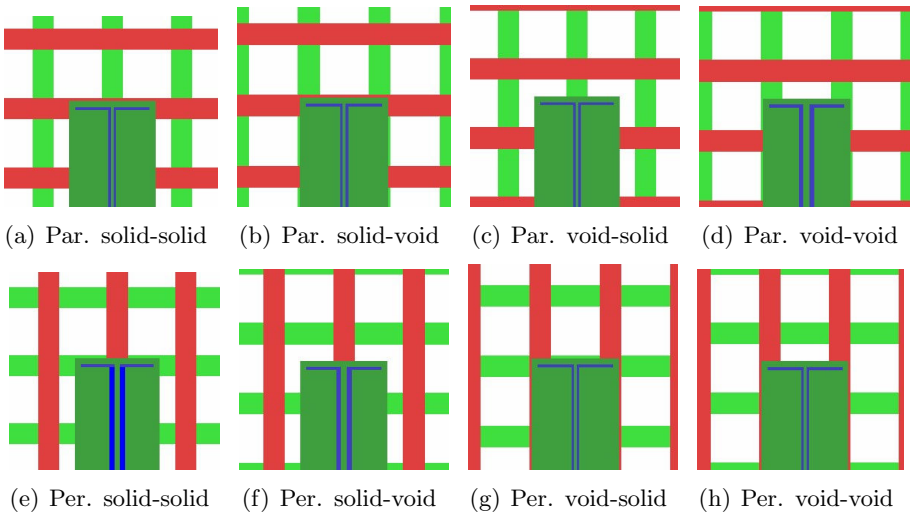

(a) Par. solid-solid (b) Par. solid-void (c) Par. void-solid (d) Par. void-void

(e) Per. solid-solid (f) Per. solid-void (g) Per. void-solid (h) Per. void-void

Figure 2.10: Dipole antenna placed at the symmetry positions of a woodpile structure. The red and green bars correspond to the bars in the first and second layer of the woodpile respectively.

Due to the large number of symmetry positions, carrying out a complete analysis and discussion of the results obtained for all of them would be tedious. Therefore, the following sections will be mainly focussed on the results obtained with two of these configurations, namely the "parallel void-void" and "perpendicular solid-solid". The reason for choosing them is that they represent both orientations and extreme cases in terms of position. For the sake of completeness, the full set of results for all the configurations is presented in Appendix A.

2.3.2 Optimized woodpile

The woodpile parameters can be optimised in order to maximize its fractional bandwidth, defined as BW/f_0, where BW is the bandwidth of the bandgap and f_0 is its central frequency. For the square bars case woodpile these optimum values are $ca = 1.22$ and $d_1 = d_2 = \frac{ca}{4}$ [Mar04]. Using these values, the dimensions for a central frequency of the gap of 500 GHz are: $a = 233\,\mu m$, $ca = 284.1\,\mu m$ and $d = d_1 = d_2 = 71\,\mu m$. The band diagram corresponding to these dimensions is shown in Figure 2.1(a). As it was mentioned, the bandwith obtained with this configuration is 21%.

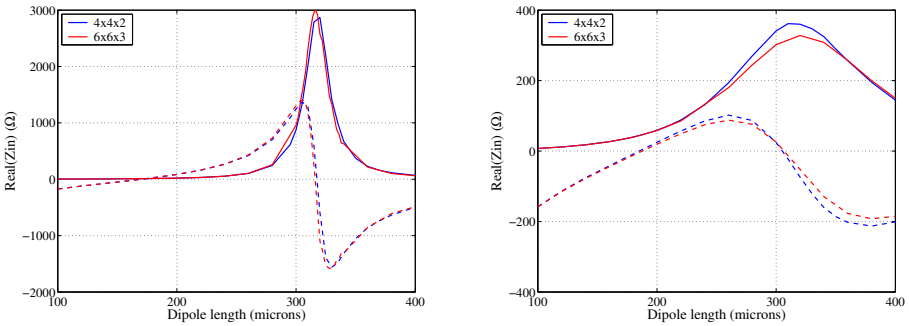

(a) Par. void-void

(b) Perp. solid-solid

Figure 2.11: Input impedance ($R_i + jX_i$) of a printed dipole placed on top of the optimized silicon woodpile as a function of its length and the number of periods considered in the analysis. The solid line represents R_i and the dashed line X_i.

Input impedance

A dipole printed on a quartz substrate was placed on top of a silicon woodpile. The dipole width, w, was arbitrarily taken as 10 microns and it was fed by a lumped gap source ($Z_0 = 170\,\Omega$). The size of the used woodpile was 4 woodpile periods in the $x-$ and $y-$directions and 2 periods in the stacking direction (z). Although this number of periods is small and would not be sufficient in order to characterize the radiation features of these configurations it is enough in order to compute the input impedance of the dipoles. An example of this is given Figure 2.11 where the input impedance obtained using $4 \times 4 \times 2$ and $6 \times 6 \times 3$ periods woodpiles are compared. The results obtained in both cases for lengths around the first resonance are identical.

Both the dipole length and the thickness of the quartz substrate were swept. The results obtained are shown in Figure 2.12 for the "parallel void-void" and "perpendicular solid-solid" configurations.

The impedance curves of both configurations are very different, being the second resonance of the "parallel void-void" more steep. This fact is common to all the "parallel" and "perpendicular" configurations, as can be seen in Figure A.1 and A.2 (Appendix A).

Moreover, within the "parallel" configurations the input impedance is mainly determined by the position of the dipole with respect to the first layer of bars. In particular, the "parallel solid-solid" and "parallel solid-void" con-

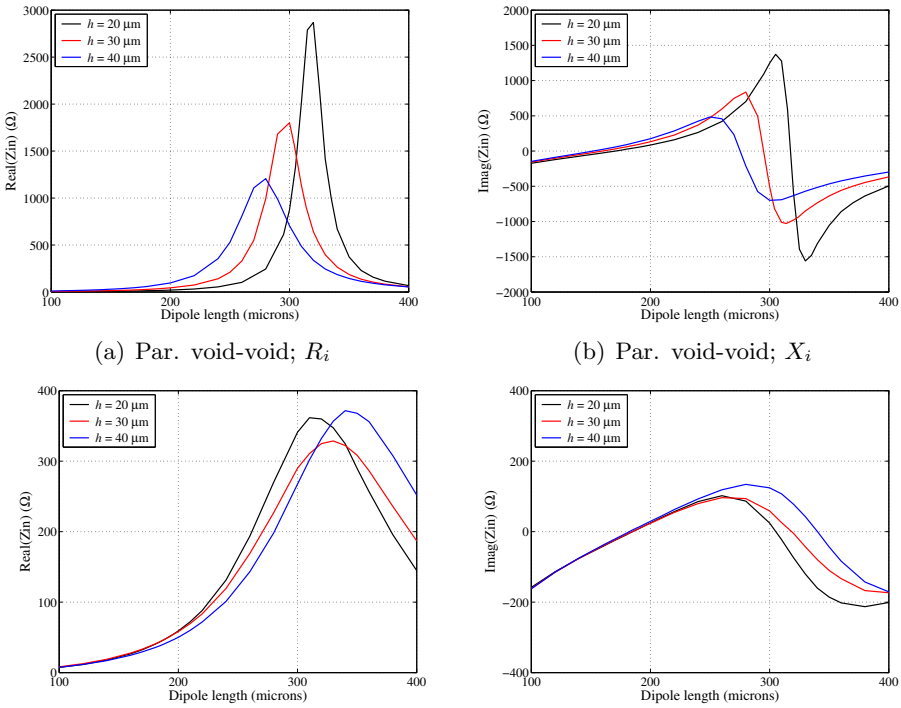

(a) Par. void-void; R_i

(b) Par. void-void; X_i

(c) Per. solid-solid; R_i

(d) Per. solid-solid; X_i

Figure 2.12: Input impedance ($R_i + jX_i$) of a printed dipole placed on top of the optimized silicon woodpile in the "parallel void-void" and "perpendicular solid-solid" symmetry positions as a function of its length and of the substrate thickness, h. f = 500 GHz.

figurations present very similar input impedance. In both cases, the second resonance of the dipole is very close for the different thicknesses of the substrate. For the other "parallel" configurations, i.e. "parallel void-void" and "parallel void-solid", the input impedance is different, being the second resonance for the different thicknesses of the substrate more separated.

This difference can be explained by the fact that the if the dipole is placed on top of a bar, it "sees" the bar mainly as a load, whereas if it is in between two bars it "sees" them as scatterers and therefore the influence of the distance, given by the thickness of the substrate is larger.

To clarify this issue a dipole has been placed on top of a layer of silicon bars parallel to it. Two cases were analysed: the dipole placed on one of the

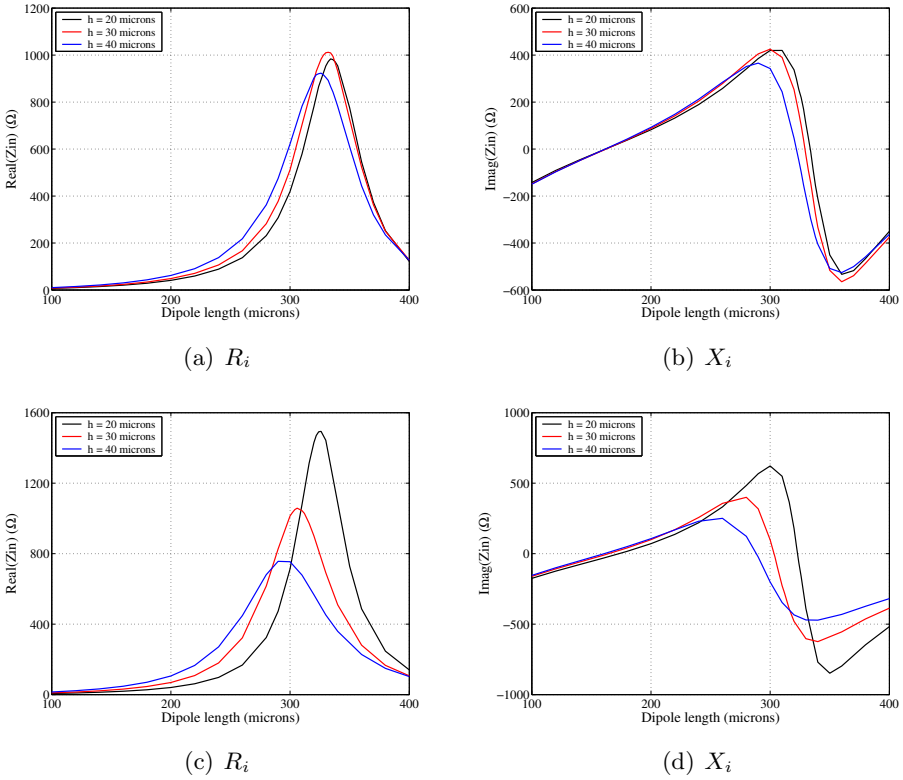

(a) R_i (b) X_i

(c) R_i (d) X_i

Figure 2.13: Input impedance ($R_i + jX_i$) of a printed dipole placed on a layer of silicon bars parallel to it as a function of its length and the substrate thickness, h. $f = 500$ GHz. (a) and (b) Dipole on one bar; (c) and (d) Dipole in between two bars.

bars, as if it were in a "parallel solid" configuration or in between two of the bars, similar to the "parallel void" configurations. The results obtained are presented in Figure 2.13. They are similar to those previously presented: if the dipole is on the bar, (a) and (b), the input impedance hardly depends on the substrate thickness, but if the dipole is between the bars, (c) and (d), the difference between the input impedances is larger. However, there is a difference between these results and those obtained using the woodpile structure: the input resistance at resonance is much lower if the woodpile is used. This effect is due to the reflection caused by the periodicity.

The "perpendicular" configurations behave similarly. In this case, the input impedance is very similar for the "solid-void" and "void-void" configura-

	$h = 20\,\mu m$		$h = 30\,\mu m$		$h = 40\,\mu m$	
Symmetry position	l_r (μm)	R_i (Ω)	l_r (μm)	R_i (Ω)	l_r (μm)	R_i (Ω)
Par. solid-solid	151.6	8.7	151.5	17.6	151.5	31.9
Par. solid-void	169.7	5.3	168.2	7.4	165.1	13.1
Par. void-solid	167.7	13.9	156.7	22.6	149.1	39.1
Par. void-void	170.5	10.8	159.5	17.9	151.8	30.9
Per. solid-solid	182.3	36.6	184.7	43.9	185	44.0
Per. solid-void	179.0	67.9	214.8	141.9	-	-
Per. void-solid	181.9	131.5	233.8	197.5	208.3	99.6
Per. void-void	175.7	158.9	-	-	-	-

Table 2.4: Resonant lengths (l_r) and input resistance at resonance (R_i) of a printed dipole antenna printed on a quartz substrate placed on top of the optimized silicon woodpile. $f = 500$ GHz.

tions, but the other two configurations have two different types of curves. This agrees with the previous results since what determines the input impedance is the bars parallel to the dipole. In the "void-solid" and "solid-solid" cases, there is a bar parallel to the dipole under it, which acts as a load. In the "void-solid" case the load is separated from the dipole by air, whereas in the "solid-solid" there is another silicon bar in between them. Thus, the load is different in the two cases and so is the input impedance.

The resonant lengths and the input resistance at resonance are presented in Table 2.4 for the different substrate thicknesses and configurations. For the "parallel" configurations the input resistance is very low for a 20 microns substrate, with values between 5 and 14 Ω. If the thickness of the substrate is increased, the impedance increases as well, but the values are still quite low. With respect to the resonant lengths, they decrease with the thickness of the substrate. In the "perpendicular" configurations the input resistance at resonance is higher and also increases when the substrate is thicker. For some configurations, namely the "perpendicular void-void" with 30 and 40 microns substrate and the "perpendicular void-solid" with 40 microns substrate, there is not a resonance. In those cases the input impedance is always capacitive.

If the phase of the wave reflected by a silicon woodpile EBG structure is

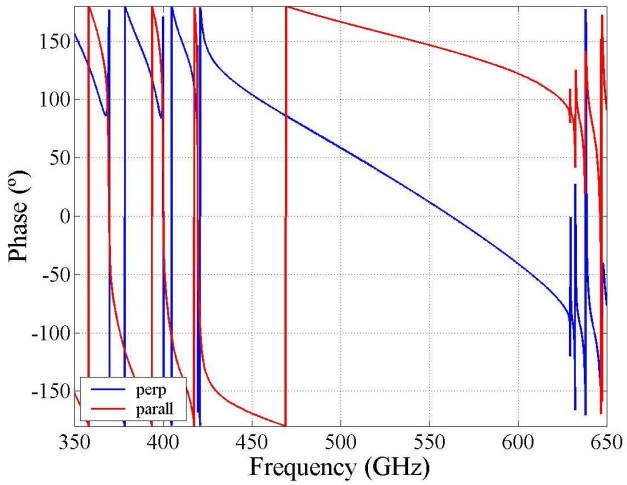

Figure 2.14: Phase of the reflected wave when a plane wave impinges normally on the optimised silicon woodpile.

computed it can be seen that for a perpendicularly polarised incident wave, i.e. E-field perpendicular to the silicon bars, the phase of the reflection coefficient is close to 0 deg, see Figure 2.14, which is similar to the behaviour of an Artificial Magnetic Conductor (AMC) [Mar04]. Conversely, for the parallel polarised incident wave, i.e. E-field parallel to the woodpile bars, the phase of the reflected wave is close to 180 deg. This could explain the different input impedance that a dipole antenna presents when is placed at these symmetry positions.

The "parallel" configurations are nearly short-circuited by the EBG substrate, what agrees with the very low input impedance of these configurations. The effect of the thickness of the quartz substrate was also predicted by the phase of the reflection coefficient, since if a quartz substrate is considered on top of the woodpile, the phase moves towards 0 deg as the substrate becomess thicker [Mar04]. However, although the phase helps to understand the general behaviour, the differences in terms of input impedance between the configurations make clear that the influence of the relative position of the dipole with respect to the surface of the EBG must also be taken into account.

With respect to the resonant lengths obtained with the different configurations, they are slightly shorter than if no woodpile is considered. If the woodpile is taken as an effective medium, its average dielectric constant is

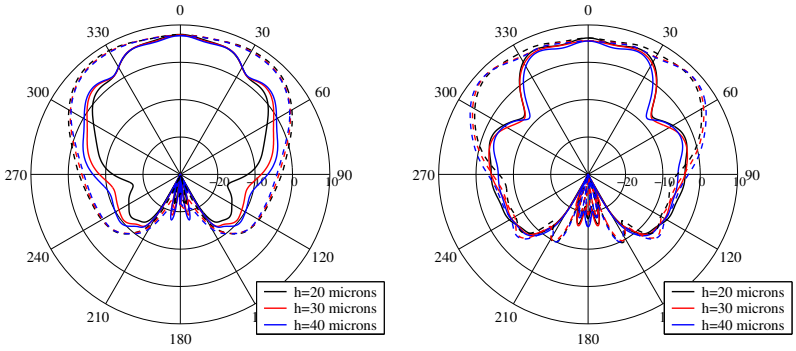

(a) Parallel void-void (b) Perp. solid-solid

Figure 2.15: Radiation patterns of a printed dipole placed on top of the optimized silicon woodpile in the "parallel void-void" and "perpendicular solid-solid" symmetry positions as a function of the thickness of the quartz substrate, h. $l = 250\,microns$; $f = 500$ GHz. Solid line: E-Plane; Dashed line: H-Plane.

4.41, which is quite close to the dielectric constant of quartz, 3.78. This could explain the small change in resonant lengths.

To summarize the results obtained in this section, it can be concluded that the input impedance of a dipole antenna on top of the optimised silicon woodpile is mainly determined by its orientation with respect to the bars in the first layer. The "parallel" symmetry positions have a very low input impedance, which can be attributed to the short-circuiting effect of the EBG. Conversely, the "perpendicular" configurations have higher impedance and could be more easily matched.

Radiation features

The radiation patterns of a dipole antenna placed on top of a woodpile in the different symmetry positions at 500 GHz were computed using Ansof HFSS. First, a $250\,\mu m$ long dipole printed on a $2a \times 2a$ (where a is the lattice constant of the woodpile structure) quartz substrate was used as radiating element. This dipole length was chosen arbitrarly and will be modified later on in order to determine its influence on the radiation pattern of the configuration. As in the previous cases, the dipole was fed by a lumped gap source ($Z_0 = 170\,\Omega$) placed between the dipole arms. The radiation pattern using a $12 \times 12 \times 3$ periods woodpile structure was computed for the same substrate thicknesses

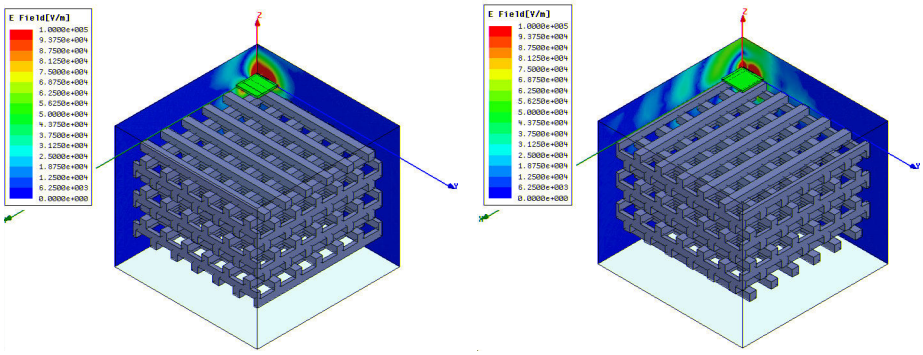

(a) Par. void-void (b) Per. solid-solid

Figure 2.16: Electric field distribution when a printed dipole is placed on top of the optimized silicon woodpile.

considered in the input impedance analysis: 20 microns, 30 microns and 40 microns. The results obtained for the "parallel void-void" and "perpendicular solid-solid" configurations are presented in Figure 2.15. The results for the rest of the configurations can be found in Figure A.3.

The radiation patterns of the configurations are very different due to the interference patterns created by the EBG structures. The perpendicular configurations are more affected, and the radiation patterns present larger ripples. For most of the configurations there is hardly any difference between the results obtained with the different thicknesses. Only in the "parallel void-solid" and "parallel void-void" symmetry position the E-plane is slightly affected by the change of thickness, becoming narrower in the endfire direction for thinner substrates. In the "perpendicular solid-void" case, the behaviour is the opposite, the radiation pattern being more directive in the endfire direction when the substrate is thinner.

The directivity of the configurations has also increased and it is larger in the "parallel" configurations. The boresight directivities obtained ranged from 2.76 dBi in the "perpendicular void-void" case to 7.42 dBi in the "parallel void-void" configuration. In general, the "perpendicular" configurations do not have its maximum at boresight due to the interference pattern. For this reason, the pattern on the "parallel" configurations is generally more symmetric.

In all cases the radiation patterns shows a large reduction of the back radiation due to the presence of the EBG. This reduction is larger in the "parallel" configurations. The reason for this is the different amount of power diffracted

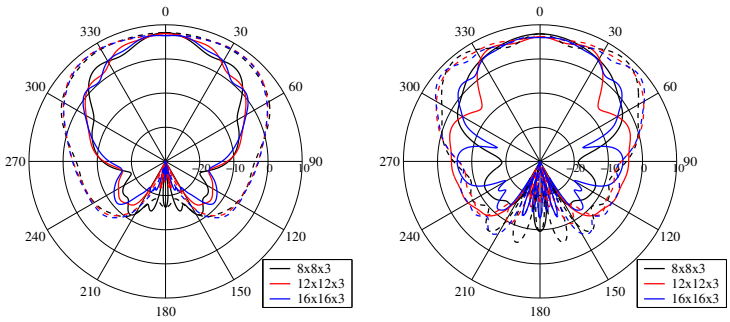

(a) Parallel void-void (b) Perp. solid-solid

Figure 2.17: Radiation patterns of a printed dipole placed on top of the optimized silicon woodpile in the "parallel void-void" and "perpendicular solid-solid" symmetry positions as a funtion of number of periods of the woodpile structure. $l = 250\,\mu m$*;* $h = 20\,\mu m$*;* $f = 500$ *GHz. Solid line: E-Plane; Dashed line: H-Plane.*

at the woodpile edges. In the "parallel" configurations the field in the H-Plane is attenuated due to the bars of the top layer, which are perpendicular to this plane. In the "perpendicular" configurations, the fields in the H-Plane are less attenuated and reach the edges of the woodpile, getting diffracted. This effect can be seen in Figure 2.16 where the field distributions for the "parallel void-void" and the "perpendicular solid-solid" are compared. In the first case the field is confined in the region close to the dipole, whereas in the other case the field reaches the edge of the woodpile, especially in the H-plane direction.

It is interesting to note in the field distribution of the "parallel void-void" configuration that the scattering mainly takes place at the bars closer to the dipole. This effect will be used in Chapter 4 to improve the radiation features of this configuration.

If the number of periods of the woodpile structure is changed, the results shown in Figure 2.17 are obtained. In this case only the 20 microns thick substrate has been considered. When the number of periods is increased from 8×8 to 12×12 there is quite a large change in the radiation patterns. If the number of periods is further increased up to 16×16 periods, the results tend to stabilize for the "parallel void-void" configuration. For the "perpendicular solid-solid" the results still change, due to the previously mentioned diffraction effect. However, the difference between these two cases is smaller than with the 8×8 case, showing that the pattern tends to stabilize also in this case. These effects are common to all the "parallel" and "perpendicular" configurations as

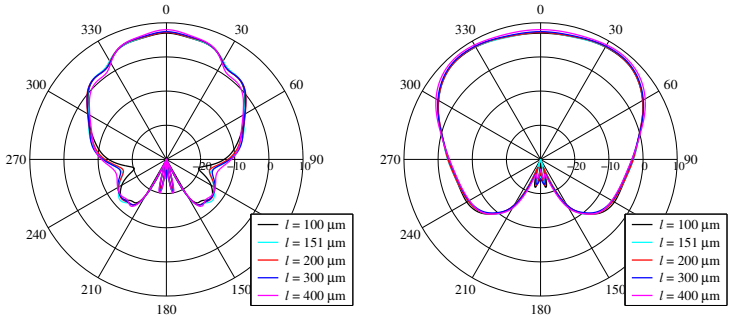

(a) Par. void-void, E-Plane (b) Par. void-void, H-Plane

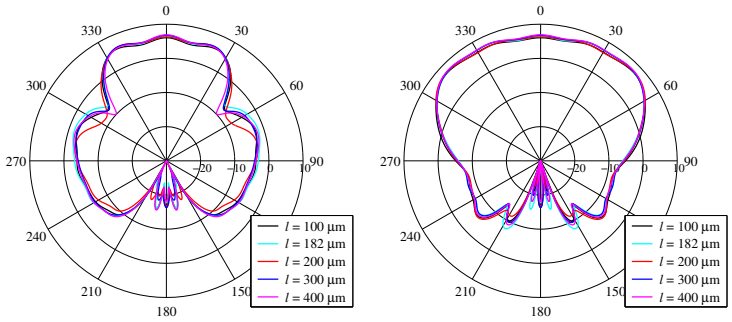

(c) Perp. solid-solid, E-Plane (d) Perp. solid-solid, H-Plane

Figure 2.18: Radiation patterns of a printed dipole placed on top of the optimized silicon woodpile structure for different lengths of the dipole. $h = 20\,\mu m$; $f = 500$ GHz.

can be seen in in Figure A.4.

In the previous results, the length of the dipole was set to 250 microns. If this length is different the patterns remain unchanged, even for dipoles longer than $\lambda_0/2$, see Figure 2.18. For the sake of comparison the radiation pattern of the resonant dipoles, i.e. 151 microns for the "parallel void-void" configuration and 181 for the "perpendicular solid-solid", has also been included in the plots. They are also similar to the other radiation patterns, showing that also for a dipole on top of a woodpile the radiation pattern does not change very much with the dipole length. These results are in agreement with those obtained for a dipole without EBG substrate.

Frequency dependence of the input impedance and radiation pattern

The previous results were computed at 500 GHz, what is the central frequency of the bandgap of the woodpile considered. In this section, the changes of the input impedance and the radiation pattern with frequency will be analysed. To carry out this analysis only a 20 microns thick substrate was considered. The width of the dipole was 10 microns and its length was swept at each frequency.

With respect to the input impedance, the results obtained for the "parallel void-void" and "perpendicular solid-solid" configurations are shown in Figure 2.19. In both cases, the shape of the curves is similar to those obtained previously. The dependence on the frequency is larger for the "parallel void-void" configuration, that losses the sharp resonance when the frequency increases. The "perpendicular solid-solid" configuration is less affected and the change in impedance is smaller.

The resonant lengths and the input resistance at resonance are summarised in Table 2.5. As it would be expected, the resonant length decreases with frequency. However, this change is different for the two configurations, as can be seen in Figure 2.20, the reason being the different interaction of the dipole radiation with the EBG structure.

With respect to the input resistance at resonance, the behaviour of both configurations is also different. In the "parallel void-void" configuration the input resistance increases with frequency, whereas in the "perpendicular solid-solid" it remains nearly constant. This can also be explained by the phase curve, shown in Figure 2.14, since the phase of the "parallel" polarisation moves further away from 180 deg when the frequency increases. This leads to the increase of the input impedance, which changes from $5\,\Omega$ to $30.5\,\Omega$. For the "perpendicular solid-solid" configuration the change frequency does not affect the inpedance so much. The oscilatory behaviour is similar to the change in the impedance of a dipole when placed close to a metallic plane at a distance close to $\lambda/4$ [Mar04].

The influence of the phase in the matching of a dipole antenna on top of an EBG structure of the "mushroom" type [Sie99b] has been studied in [Yan03]. In this case the optimum frequency range, determined in terms of the matching to a $50\,\Omega$ impedance, was that where the phase of the reflected wave was 90 ± 45 deg. Although a further study is still required, in our case the results seem to be different, since the optimum phase is closer to 0 deg. Also the influence of the position of the dipole with respect to the structure

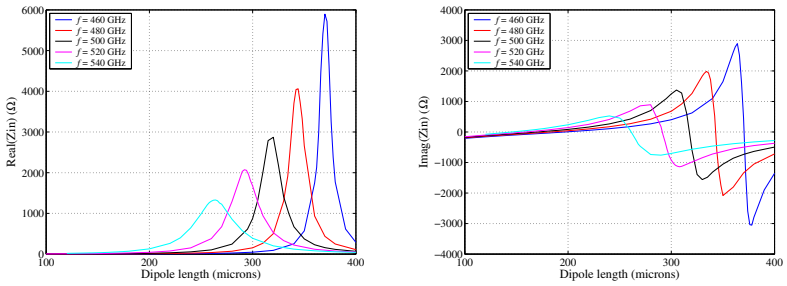

(a) Par. void-void; R_i (b) Par. void-void; X_i

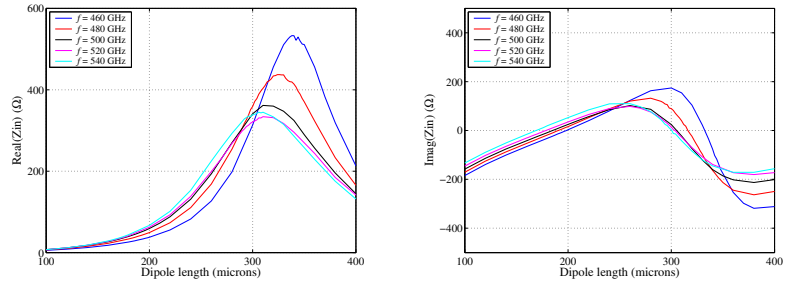

(c) Perp. solid-solid; R_i (d) Perp. solid-solid; X_i

Figure 2.19: Input impedance ($R_i + jX_i$) of a printed dipole placed on top of the optimized silicon woodpile when the analysis frequency is changed. $h = 20\,\mu m$

	Parallel void-void		**Perpendicular solid-solid**	
$f_c\ (GHz)$	$l_r\ (\mu m)$	$R_i\ (\Omega)$	$l_r\ (\mu m)$	$R_i\ (\Omega)$
460	197	5.0	198	36.5
470	190	6.0	194	41.0
480	183	7.3	193	41.0
490	177	7.85	188	42.0
500	170.5	10.8	182	36.6
510	165	13.6	182	43.0
520	159	17.0	178	40.0
530	152	22.0	175	37.3
540	145	30.5	169	34.7

Table 2.5: Resonant length (l_r) and input resistance at resonance (R_i) of a dipole antenna printed on a h=20 microns substrate placed on top of the optimized silicon woodpile as a function of frequency.

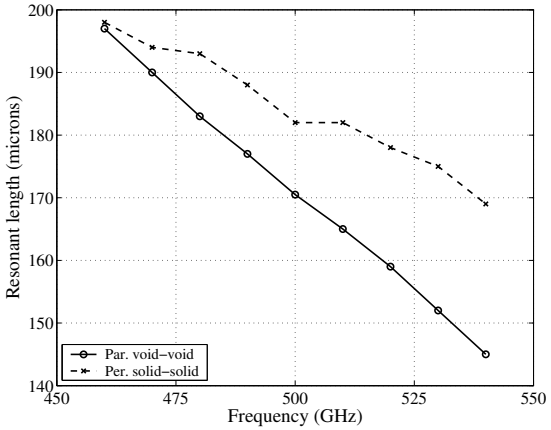

Figure 2.20: Resonant length vs. frequency of a dipole antenna printed on a quartz substrate and placed on top of the optimized silicon woodpile in the "parallel void-void" and "perpendicular solid-solid" symmetry positions. $h = 20\,\mu m$

seems to be larger in our case.

Regarding the radiation patterns, the results obtained for a 250 microns dipole on a 20 microns substrate are presented in Figure 2.21. The woodpile dimensions considered are $12 \times 12 \times 3$ periods. For the "parallel void-void" configurations the directivity is slightly higher for frequencies lower than 500 GHz than for higher frequencies. This also agrees with the reflected phase being closer to 180 for these frequencies, since in this case the directivity should be maximum [Bal97]. For the "perpendicular solid-solid" configuration the radiation patterns are also more directive at lower frequencies. Note that the pattern at 540 GHz is quite distorted due to the fact that this frequency lies very close to the end of the gap.

2.3.3 Dependence with woodpile parameters

In the previous results the dimensions of the woodpile that was used corresponded to the optimized design in terms of fractional bandgap. However, there are many combinations of woodpile parameters that create a bandgap, although not as large as this one. It could be the case that the performance of a non optimum (in terms of bandwidth) woodpile were better than the performance of the optimum one. Therefore, in this section, the influence of the woodpile dimensions on the performance of a dipole antenna will be studied.

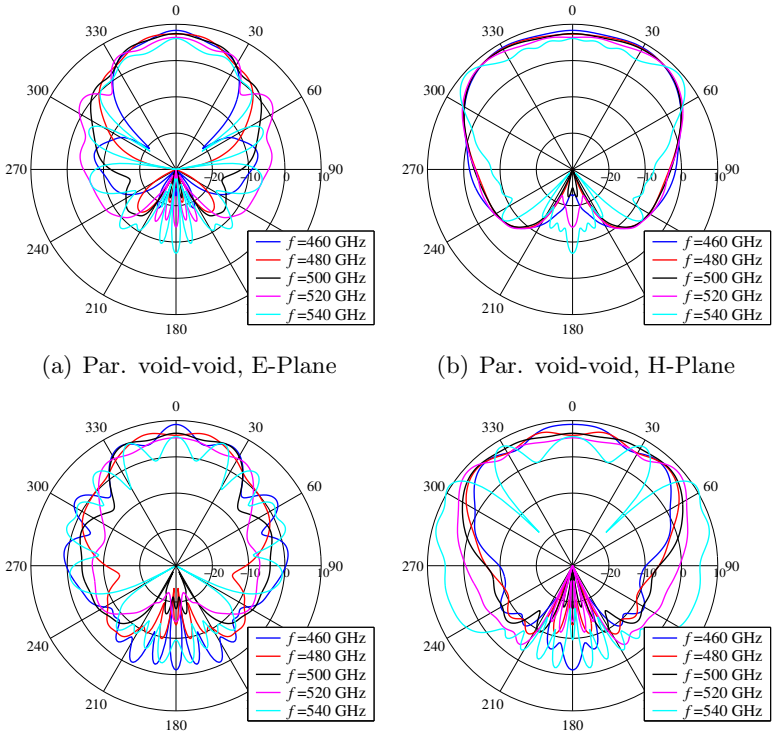

(a) Par. void-void, E-Plane

(b) Par. void-void, H-Plane

(c) Perp. solid-solid, E-Plane

(d) Perp. solid-solid, H-Plane

Figure 2.21: Radiation patterns of a printed dipole placed on top of the optimised silicon woodpile EBG structure when the frequency is changed. $l = 250\,microns$*;* $h = 20\,microns$*.*

The modification of the woodpile is based on the change of the parameter c, keeping the bars square, i.e. $d_1 = d_2 = ca/4$. For each c, the central frequency of the gap changes and the lattice constant, a, was chosen, so that the gap was centred at 500 GHz. With these restrictions the bandgap is a maximum for $c = 1.22$, which was the value that was previously used. The values of a used in each case along with the bandgap obtained can be found in Table 2.6. Only values of c larger than 0.8 have been considered, since for lower values the gap closes very rapidly.

As in the frequency dependence study, only the "parallel void-void" and the "perpendicular solid-solid" configurations will be considered.

c	a (μm)	Bandgap (%)
0.8	302.9	10.0
0.9	282.7	15.9
1.0	266.2	19.9
1.1	250.7	20.2
1.3	223.4	20.3
1.4	214.6	19.7
1.5	202.4	18.9

Table 2.6: Dimensions of the woodpile structure for different values of c. The central frequency of the gap is 500 GHz.

Input impedance

The results obtained for the different woodpile dimensions are presented in Figure 2.22. In both cases the second resonance is more affected than the first one. If we focus on the first resonance, the resonant lengths and input resistances obtained are shown in Table 2.7. For the "parallel void-void" configuration the resonant length increases with c and at the same time the input resistance is lower. The change in resonant length is very small, from 167.2 microns at $c = 0.8$ to 171.3 at $c = 1.5$. In these two limit cases the input impedance takes values of $21.7\,\Omega$ and $11.3\,\Omega$ respectively. In the case of the "perpendicular void-void" configuration the resonance length also increases with c, from 181.5 to 188.8 microns, whereas the input impedance gets higher. The change in input impedance is larger in this case, varying from $17.9\,\Omega$ to $55.3\,\Omega$. The relation of these results with the phase of the reflected wave in the different configurations has not been investigated yet.

Radiation features

The radiation patterns obtained with these configurations, using a 250 microns long dipole printed on a 20 microns thick substrate and placed on top a $12 \times 12 \times 3$ periods woodpile are presented in Figure 2.23.

For the "parallel void-void" configuration, the directivity increases with c. This change in the directivity is caused by the change of the lattice constant of the woodpile, a, which makes the bars be closer to the dipole when c increases.

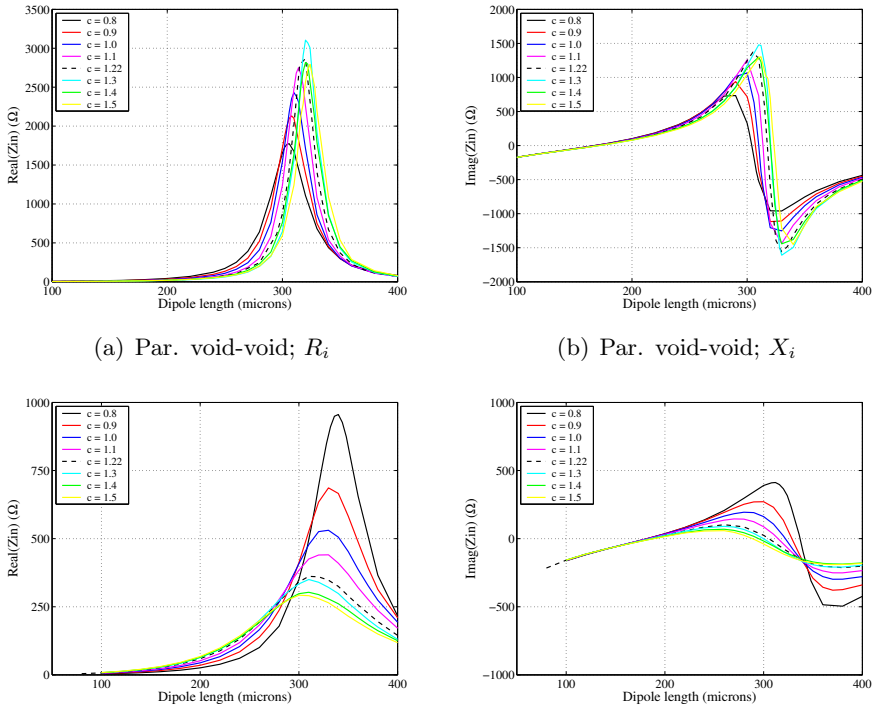

(a) Par. void-void; R_i

(b) Par. void-void; X_i

(c) Perp. solid-solid; R_i

(d) Perp. solid-solid; X_i

Figure 2.22: Input impedance ($R_i + jXi$) of a printed dipole placed on top of a silicon woodpile for different values of c. $h = 20$ microns; $f = 500$ GHz.

	Parallel void-void		**Perpendicular solid-solid**	
$\boldsymbol{c}$	$\boldsymbol{l_r}$ **(**$\boldsymbol{\mu m}$**)**	$\boldsymbol{R_i}$ **(**$\boldsymbol{\Omega}$**)**	$\boldsymbol{l_r}$ **(**$\boldsymbol{\mu m}$**)**	$\boldsymbol{R_i}$ **(**$\boldsymbol{\Omega}$**)**
0.8	167.2	21.7	181.5	17.9
0.9	167.6	17.2	181.7	24.7
1.0	168.2	14.7	182.1	31.1
1.1	169.2	12.3	183.2	37.2
1.3	171.4	10.0	185.3	47.7
1.4	170.6	11.4	188.0	52.2
1.5	171.3	11.3	188.8	55.3

Table 2.7: Resonant lengths (l_r) and input impedance at resonance (R_i) of a dipole antenna printed on a quartz substrate placed on top of a silicon woodpile for different values of c. $h = 20$ microns; $f = 500$ GHz.

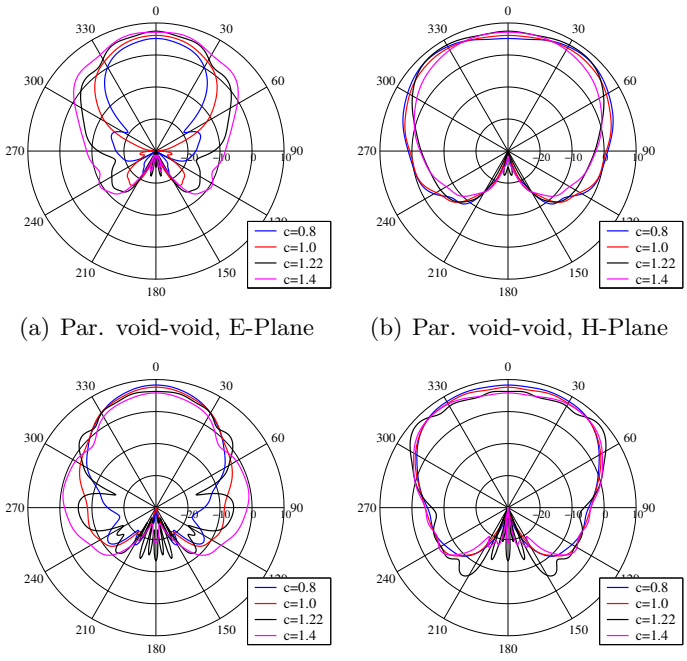

(a) Par. void-void, E-Plane (b) Par. void-void, H-Plane

(c) Perp. solid-solid, E-Plane (d) Perp. solid-solid, H-Plane

Figure 2.23: Radiation patterns of a dipole placed on top of a silicon woodpile EBG structure for different values of c. $l = 250\,\mu m$; $h = 20\,\mu m$; $f = 500$ GHz.

With respect to the "perpendicular solid-solid" symmetry position, there is a slight change in directivity, which also becomes larger when c decreases.

2.4 Dipole on top of ZTT woodpile structure

2.4.1 Description of the EBG structure and symmetry considerations

As it was mentioned, by increasing the dielectric constant the width of the band gap of an EBG structure can be widen and its physical size can be reduced. In this case, the ZTT ceramic material ($\epsilon_r = 37$) will be used to create the woodpile structure. The dispersion diagram of the optimised in terms of bandwidth ZTT woodpile can be seen in Figure 2.1(b). In this case the dimensions of the woodpile are (see Figure 2.9 for a description of the

woodpile parameters): $a = 141\,\mu m$, $ca = 172\,\mu m$ and $d_1 = d_2 = 43\,\mu m$. With these dimensions a fractional bandwidth of 32.8% is achieved.

Since we are dealing with the same EBG structure, the same symmetry positions that were explained for the silicon woodpile apply in this case. Also in this case we will focus on the "parallel void-void" and "perpendicular solid-solid" configurations, the full set of results being showed in Appendix B.

2.4.2 Input impedance

A similar study as for the silicon woodpile was carried out for the ceramic woodpile. A planar dipole, printed on a quartz substrate was placed on top of the ceramic woodpile at the different symmetry positions and the input impedance of the dipole was determined. In this case the dipole was surrounded by 6 woodpile periods in both x and y directions and 2 periods in the stacking direction, z. A larger number of periods is used in this case so that the total area of the configuration is similar to that in the case of the silicon woodpile. Both the dipole length and the thickness of the quartz substrate were swept. The results obtained for the "paralell void-void" and "perpendicular solid-solid" configurations are shown in Figure 2.24. The results for the rest of the "parallel" and "perpendicular" configurations are presented in Figure B.1 and Figure B.2 (Appendix B) respectively.

The behaviour for the "parallel" configurations is the same as in the case of the silicon woodpile. The input impedance depends mainly on the position of the dipole with respect to the first row of bars, which are parallel to the dipole. The input resistance in this case is even lower than for the silicon woodpile, see Table 2.25. This effect can be related to the phase of the reflected wave under normal incidence as it was pointed out in the silicon woodpile section, since also in this case the phase of the reflected wave is close to 180 deg for this polarisation [Mar04].

In the "perpendicular" configurations the results are quite different from the silicon case, especially in the "perpendicular void-solid" and the "perpendicular void-void" configurations. The reason for this behaviour is that the lattice constant is smaller than the dipole and thus there is a bar under the dipole which distorts the current distributions and that creates a resonance. In the "perpendicular void-solid" case, and for $h = 40$ microns this effect is even stronger, as can be seen in Figure 2.26. In this plot, the field distribution for the different "perpendicular" polarisations is compared, showing a completely different behaviour in the case of the "perpendicular void-solid"

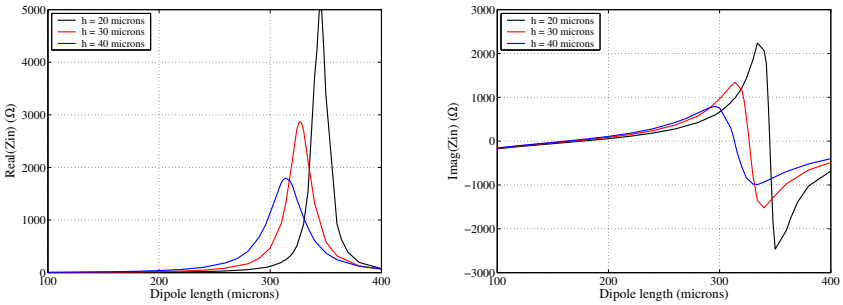

(a) Par. void-void; R_i (b) Par. void-void; X_i

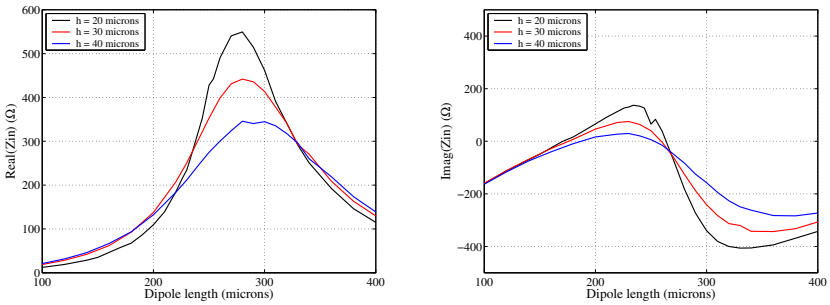

(c) Per. solid-solid; R_i (d) Per. solid-solid; X_i

Figure 2.24: Input impedance ($R_i + jX_i$) of a printed dipole placed on top of a ZTT woodpile in the "parallel void-void" and "perpendicular solid-solid" symmetry positions as a function of its length and of the substrate thickness, h. $w = 10\,\mu m$; $f = 500$ GHz.

	$h = 20\,\mu m$		$h = 30\,\mu m$		$h = 40\,\mu m$	
Symmetry position	l_r (μm)	R_i (Ω)	l_r (μm)	R_i (Ω)	l_r (μm)	R_i (Ω)
Par. solid-solid	158.8	3.9	159.0	8.9	157.0	17.0
Par. solid-void	166.3	4.1	160.2	20.2	163.5	9.8
Par. void-solid	175.7	5.5	166.0	10.2	160.6	17.8
Par. void-void	176.1	5.6	166.9	10.6	161.4	18.2
Per. solid-solid	170.7	58.2	175.8	86.1	187.2	107.3
Per. solid-void	171.9	70.7	181.2	93.3	185.7	92.1
Per. void-solid	134.0	57.1	131.0	67.6	-	-
Per. void-void	133.0	76.5	136.2	84.1	262.1	309.0

Figure 2.25: Resonant lengths (l_r) and input resistance at resonance (R_i) of a dipole antenna printed on a quartz substrate and placed on top of a ZTT woodpile. $w = 10\,\mu m$; $f = 500$ GHz.

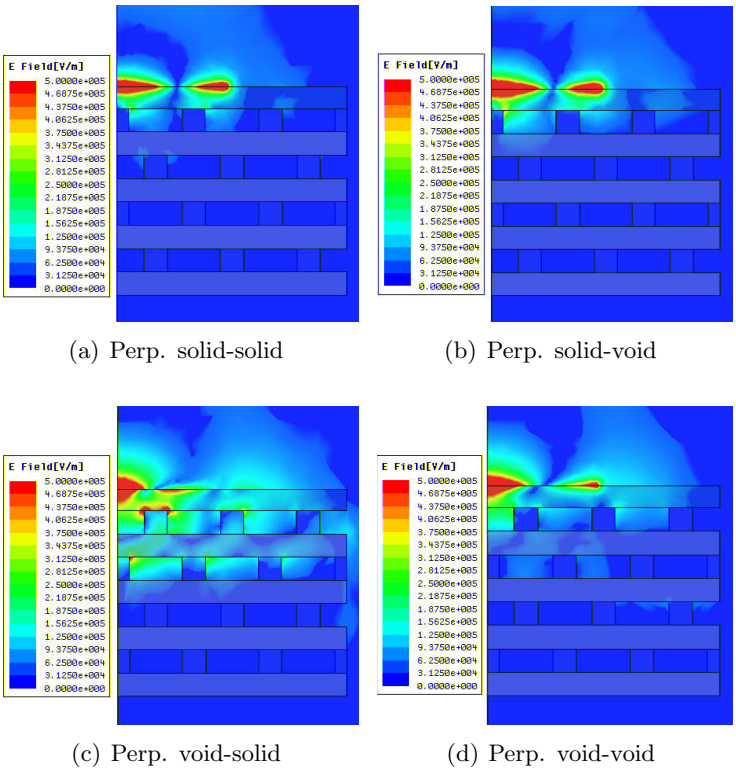

(a) Perp. solid-solid (b) Perp. solid-void

(c) Perp. void-solid (d) Perp. void-void

Figure 2.26: Electric field distributions of a dipole placed on top of the ZTT woodpile EBG structure. $h = 40\,\mu m$; $l = 250\,\mu m$; $f = 500$ GHz.

configurations. However, the input impedance at resonance is also higher for these symmetry positions, which can also be related with the reflected phase, close to 0 deg.

The resonant lengths in these configurations are slightly shorter than for the silicon woodpile. In this case the effective dielectric constant of the woodpile is 12, what would justify a larger decrease of the resonant length. This indicates that the effective medium theory is not applicable for this kind of configurations.

2.4.3 Radiation pattern

The radiation patterns of a dipole antenna placed on top of a woodpile in the different symmetry positions at 500 GHz have been obtained, using the

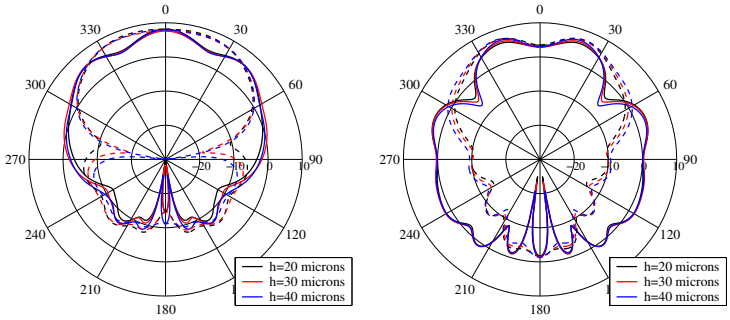

(a) Parallel void-void (b) Perp. solid-solid

Figure 2.27: Radiation patterns of a printed dipole placed on top of the optimised ZTT woodpile as a function of the substrate thickness. $12 \times 12 \times 2$ *periods;* $l = 250\,\mu m$*;* $f = 500$ *GHz. Solid line: E-Plane; Dashed line: H-Plane.*

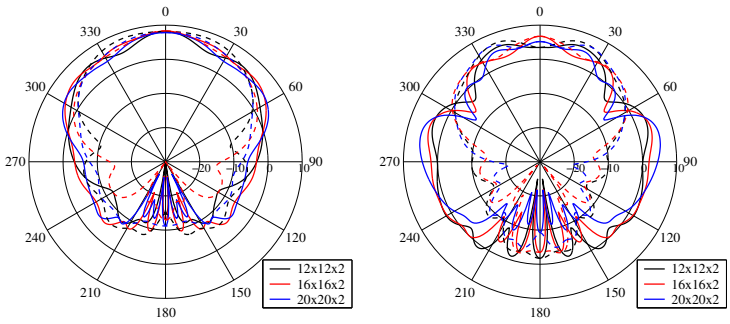

(a) Parallel void-void (b) Perp. solid-solid

Figure 2.28: Radiation patterns of a printed dipole placed on top of the optimised ZTT woodpile as a function of the number of periods of the EBG structure. $l = 250\,\mu m$*;* $h = 20\,\mu m$*;* $f = 500$ *GHz. Solid line: E-Plane; Dashed line: H-Plane.*

same configuration as for the silicon woodpile. The woodpile consisted of $12 \times 12 \times 2$ periods and the dipole width and length were 10 and 250 microns respectively. Three different substrate thickness are compared, namely 20, 30 and 40 microns.

First, the radiation patterns obtained in the "parallel void-void" and "perpendicular solid-solid" configurations are shown in Figure 2.27. In these two cases there is hardly no difference in the radiation patterns when the thickness of the substrate is changed. The radiation pattern obtained with the rest of

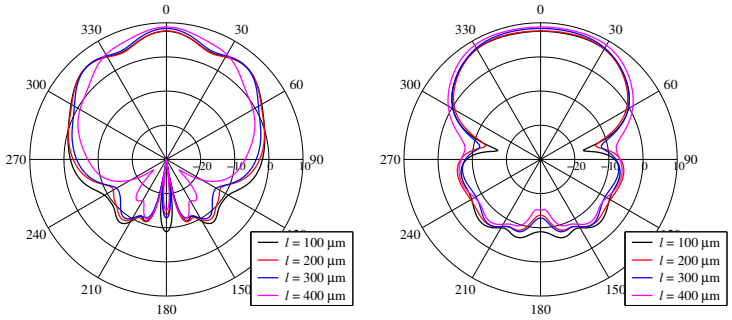

(a) Par. void-void, E-Plane (b) Par. void-void, H-Plane

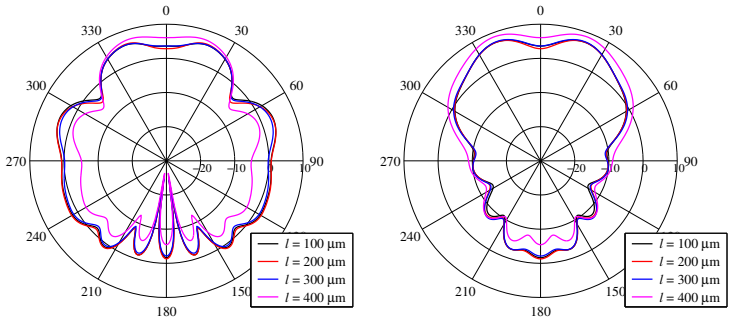

(c) Perp. solid-solid, E-Plane (d) Perp. solid-solid, H-Plane

Figure 2.29: Radiation patterns of a printed dipole placed on top of the optimised ZTT woodpile for different lengths of the dipole. $h = 20\,\mu m$; $f = 500$ GHz.

the configurations are presented in Figure B.3. In these cases, only for the "perpendicular void-solid" and "void-void" configurations there is a different pattern when the 40 microns thick substrate is used. As it was already pointed out when the input impedance was studied, in both cases there is a resonance for this thickness which also creates a very different radiation pattern.

As it was the case in the silicon woodpile, the "parallel" configurations show lower levels of back-radiation. The reason is the same as in the previous case: the field in the "perpendicular" polarisations can arrive more easily to the edge of the woodpile, getting diffracted and increasing the back-radiation.

The results obtained when the number of woodpile periods was changed are presented in Figure 2.28 for the "parallel void-void" and "perpendicular solid-solid" configurations and in Figure B.4 for the rest of them. In this case, the dependence on the size of the EBG structure is larger than for the Si woodpile

and only the "parallel void-solid" and "void-void" configurations seem to have converged to the pattern corresponding to the infinite configuration. In the rest of the configurations the patterns show larger difference between plots. According to these results, the number of periods required for a stabilised radiation pattern is larger for the ceramic woodpile than for the silicon one. Since this effect is related with the diffraction at the edges of the EBG, it depends on the real size of the structure and not on the number of periods. As the period of the ceramic woodpile is smaller than the period of the silicon woodpile, the number of periods required in order to have the same physical dimensions is larger.

In the previous results, the length of the dipole was set to 250 microns. If this length is varied the patterns remain unchanged for the shortest dipoles, see Figure 2.29. In the case of the longest dipole considered, i.e. $l = 400$ microns, the pattern is slightly different from the other ones.

2.5 Dipole on top of ZTT Fan EBG structure

The Fan EBG structure was proposed in 1994 [Fan94]. To the best of our knowledge, since then little work has been carried out on its use in any practical application. In particular, in the field of antennas, it seems that it has not examined yet as substrate. In this section its performance when combined with printed dipole antennas will be studied.

2.5.1 Description of the EBG structure and symmetry considerations

This section describes the implementation of Fan's EBG structure that has been considered in the simulations. As in the woodpile case, its dimensions can be optimised in order to obtain the largest bandgap. However, the dimensions of the optimum structure for a central frequency of 500 GHz and using ZTT as dielectric material are quite difficult to manufacture due to the tight tolerances required. These are particularly demanding for the spacing between cylinders [Azc03; Mar04].

Therefore, the dimension that have been used in this study, do not correspond to the optimum structure in terms of bandwidth but to the optimum if a trade-off is carried between manufacturability and performance [Azc03]. The dimensions of this particular Fan structure are (see Figure 2.30): $a = 221.51\,\mu m$, $r = 50.95\,\mu m$, $w = 79.74\,\mu m$, $d = 112.97\,\mu m$, $b = 157.27\,\mu m$,

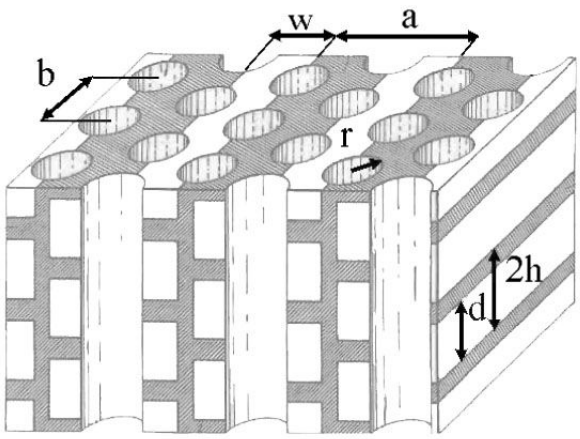

Figure 2.30: Geometry of Fan EBG structure. The grey and white areas represent the dielectric material and the air regions respectively.

$h = 77.53\,\mu m$. With these parameters a gap of 32.5% is achieved as it is shown in its band diagram, Figure 2.1(c). Note that in this case, as it was previously mentioned, although a high dielectric constant material has been used, the size of the EBG structure is similar to the size of the silicon woodpile.

With respect to the determination of its symmetry positions, this structure is more complicated than the woodpile. If the structure is cut by a plane that is perpendicular to the axis of the air cylinders, such as the top plane in Figure 2.30, there is only one symmetry plane, which is perpendicular to the square holes and cuts the centre of the circles. These planes are represented by the dashed lines in Figure 2.31. Since there is only one symmetry plane, only one of symmetry planes of the dipole will coincide with it and the symmetry of the radiation pattern of the dipole will be lost.

Taking this into account, the symmetry positions that have been identified are presented in Figure 2.31, showing the two different dipole orientations. The different configurations can be classified in two groups. The first group is formed by the configurations in which the dipole is perpendicular to the symmetry plane and thus parallel to the dielectric areas of the top layer ("parallel" configurations from here on, see Figure 2.31.a)). Those configurations in which the dipole is parallel to the symmetry plane and thus perpendicular to the dielectric regions will be named as "perpendicular" configurations, see Figure 2.31.b) and c). This definition of the dipole orientations is similar to that used

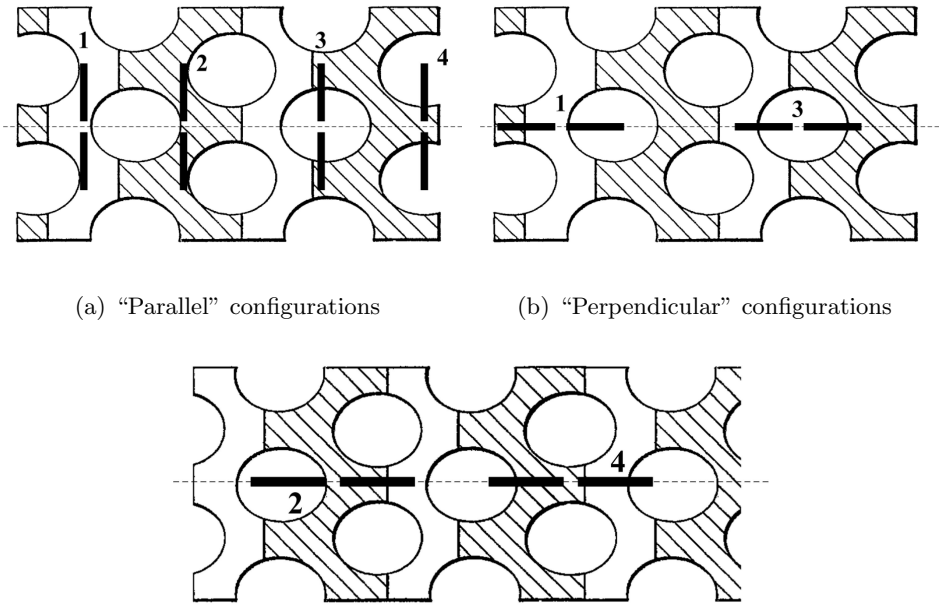

(a) "Parallel" configurations

(b) "Perpendicular" configurations

(c) "Perpendicular" configurations

Figure 2.31: Dipole placed on the symmetry positions of Fan EBG structure. The black rectangles are the two arms of the dipole. The shaded regions correspond to any dielectric material and the white ones to air. The dashed line represents a symmetry plane.

for the woodpile structure.

Inside these two groups there are no real symmetry positions and some positions on top of the structure have been selected, based on a combination of the symmetry positions of the hexagonal lattice and the areas of air and high dielectric constant material. Although this set of positions is arbitrary, their features will give a good insight into the performance of Fan structure as substrate for dipole antennas.

As in the previous EBG structures, in the following sections we will concentrate on two of the symmetry positions, namely the "parallel #1" and the "perpendicular #1". Again, the reason for choosing them is that they represent both orientations and extreme cases in terms of position. The full set of results obtained for all the configurations can be found in Appendix C.

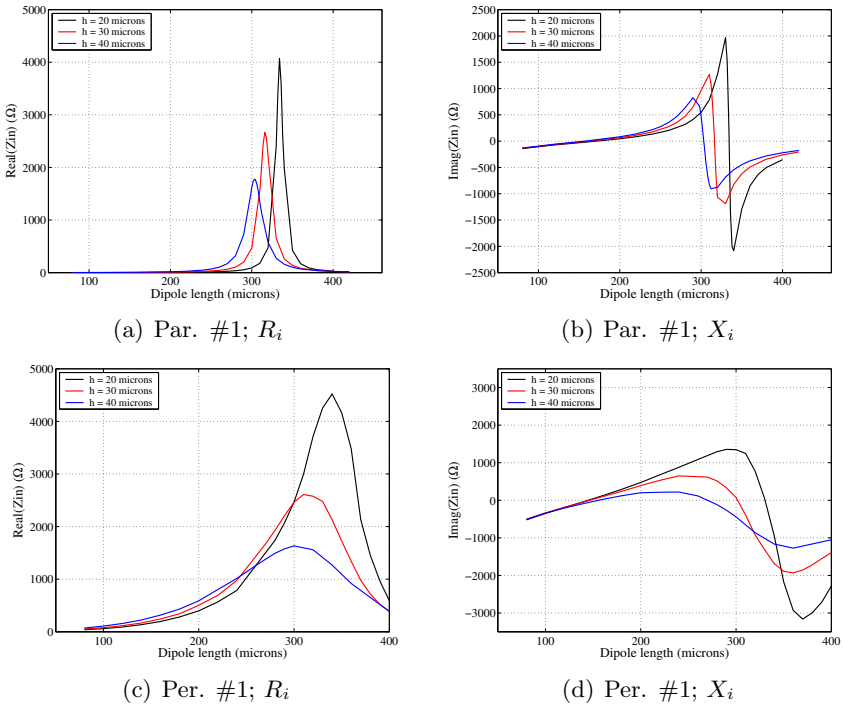

(a) Par. #1; R_i

(b) Par. #1; X_i

(c) Per. #1; R_i

(d) Per. #1; X_i

Figure 2.32: Input impedance ($R_i + jXi$) of a printed dipole placed on top of a ZTT Fan EBG structure, $\epsilon_r = 37$, in the "parallel #1" and "perpendicular #1" symmetry positions as a function of its length and of the substrate thickness. $w = 10\,\mu m$; $f = 500$ GHz.

2.5.2 Input impedance

As for the previous EBG structures, the input impedance of a dipole antenna when placed on top of Fan structure has been studied. Also in this case the dipole antenna was also fed by a lumped gap port ($Z_0 = 170\,\Omega$) and its width was arbitrarily set to 10 microns.

The variation with the length of the input impedance of the dipole for the two selected configurations is presented in Figure 2.32. As it happened in the previously studied EBG structures, in this case the behaviour of the two polarisations is also very different. The "perpendicular" configurations present high input impedance, whereas the "parallel" ones are nearly short-circuited. The reason can also be found in the phase of the reflected wave, since it is close to 180 deg for the "parallel" configurations, whereas it is closer to 0 deg

	$h = 20\,\mu m$		$h = 30\,\mu m$		$h = 40\,\mu m$	
Symmetry position	l_r (μm)	R_i (Ω)	l_r (μm)	R_i (Ω)	l_r (μm)	R_i (Ω)
Par. #1	170.7	2.8	162.3	4.1	156.4	6.5
Par. #2	211.8	0.6	196.1	1.0	185.1	2.5
Par. #3	159.6	0.8	158.3	1.3	158.3	2.6
Par. #4	184.0	1.0	174.4	1.4	167.4	2.6
Perp. #1	144.8	149.7	146.3	191.5	155.8	297.6
Perp. #2	181.0	35.6	174.1	51.5	172.2	87.5
Perp. #3	159.6	90.0	158.6	122.0	187.5	269.8
Perp. #4	147.8	132.2	149.0	175.7	155.8	261.2

Table 2.8: Resonant length (l_r) and input resistance at resonance (R_i) of a printed dipole on top of a ZTT Fan EBG structure. $w = 10\,\mu m$; $f = 500$ GHz.

for the "perpendicular" ones [Mar04].

The resonant lengths and the input resistance values at resonance are given in Table 2.8. With respect to the resonant lengths, they are not shorter than those of the dipole without EBG. This result also shows that the effective medium can not be used in this configuration, since in this case the effective dielectric constant for this structure is 10.7, but the dipole size is not reduced accordingly.

The input resistance at resonance is very low for the "parallel" polarisations whereas it is higher for the "perpendicular" ones. As for the previous EBG structures it increases when the quartz substrate is thicker.

2.5.3 Radiation patterns vs. symmetry position

In order to check the radiation properties of a dipole on top of Fan EBG structure the same configuration used for the input impedance analysis has been used. Initially, the dipole length has been set arbitrarly to $250\,\mu m$ and the substrate thickness has been varied. The results corresponding to the "parallel #1" and "perpendicular #1" symmetry positions are presented in Figure 2.33. The dimensions of the EBG structure were $6 \times 6 \times 2$ periods in the $x-$, $y-$ and $z-$directions. The reason for using a smaller number of periods than in the woodpile case is that the structure is more intricate than

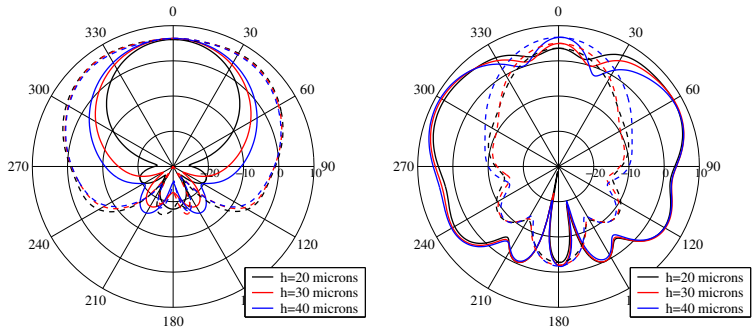

(a) Par. #1 (b) Perp. #1

Figure 2.33: Radiation pattern of a printed dipole dipole placed on top of a ZTT Fan EBG structure at the "parallel #1" and "perpendicular #1" symmetry positions as a function of the thickness of the quartz substrate. $l = 250\,\mu m$; $f = 500$ GHz. Solid line: E-Plane; Dashed line: H-Plane.

the woodpile, what makes its analysis more difficult due to the large memory requirements.

Both configurations present very different radiation pattern, which are similar in the rest of the the "perpendicular" and "parallel" configurations, as can be seen in Figure C.3. According to these results, the radiation patterns depend mainly on the orientation of the dipole with respect to the symmetry plane and not on its position with respect to the dielectric and air regions.

Dipoles placed in "perpendicular" symmetry positions show a very broad E-Plane, whereas their H-plane is rather narrow. For these configurations the maximum directivity does not correspond to boresight, but to approximately 60 deg. The patterns are not very dependent on the thickness of the quartz substrate, except in the position "perpendicular #3" in which the pattern becomes more asymmetric when the thickness of the substrate increases.

The radiation patterns corresponding to the "parallel" symmetry positions have a more symmetric and directive radiation pattern. However, for some of these configurations there is a null at boresight, depending on the thickness of the quartz substrate. These configurations are more sensitive to the substrate thickness than the "perpendicular" ones.

The reason for the changes of the radiation pattern can be understood by inspecting Figure 2.34, where the field distributions for the configurations "perpendicular #3" is shown. In this plot it can be seen that the field distri-

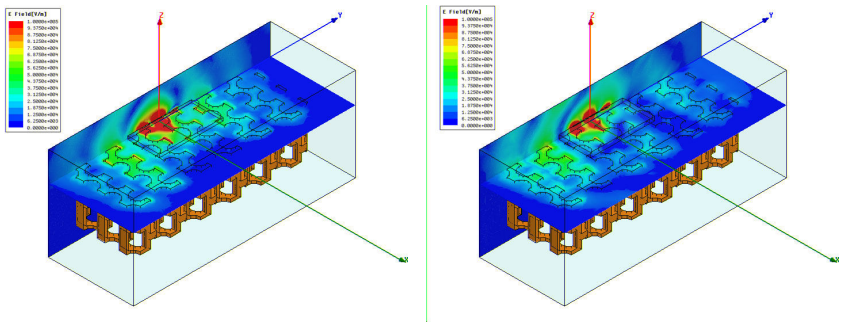

(a) $h = 20$ microns (b) $h = 30$ microns

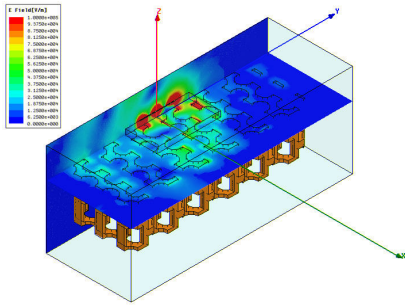

(c) $h = 40$ microns

Figure 2.34: Electric field distributions corresponding to the "perpendicular #3" symmetry position for different thickness of the quartz substrate.

bution depends very strongly on the thickness of the substrate, what justifies the changes in the radiation pattern.

The back radiation levels are lower in the "parallel" polarisations. This fact is similar to the behaviour of a dipole on top of a woodpile. In Fan structure dipoles placed at "perpendicular" configurations are perpendicular to the dielectric areas and their radiation in the H-Plane "sees" less discontinuities than the H-Plane radiation of the "parallel" configurations. Therefore, the field arrives more easily to the edge of the EBG substrate, contributing to the back-radiation.

With respect to the influence of number of periods of the EBG structure, a comparison between the results with $6 \times 6 \times 2$ periods and $8 \times 8 \times 2$ can be found in Figure 2.35. For the two studied configurations the results are very similar in both cases. However, the difference between curves is larger in the

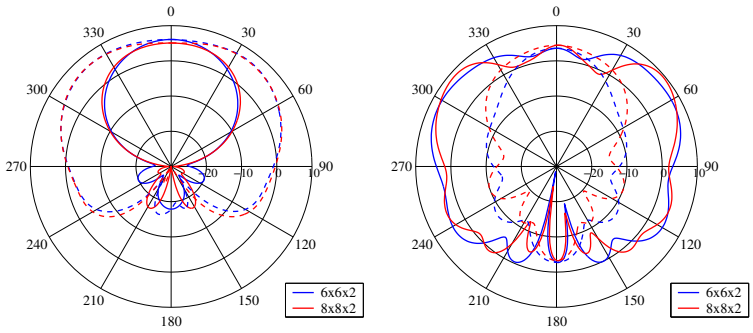

(a) Par. #1 (b) Perp. #1

Figure 2.35: Radiation pattern of a printed dipole placed on top of a ZTT Fan EBG structure at the "parallel #1" and "perpendicular #1" as function of the number of periods of the EBG structure. $h = 20\,\mu m$; $f = 500$ GHz. Solid line: E-Plane; Dashed line: H-Plane.

"perpendicular" configuration, being related with the orientation of the dipole with respect to the dielectric areas, as it was just discussed.

Although the number of periods used is much smaller than the number of periods used with the woodpile structure, the results seem to have converged. This fact can be related with the intricate surface of this particular EBG structure, which has discontinuities in all directions and does not allow the field to propagate easily on the surface. With respect to the number of periods in the "stacking direction", two periods have been shown to be enough for all the configurations.

If the length of the dipole antenna is varied, a similar effect to that observed with the woodpile structure can be found (see Figure 2.36). For both configurations the dipole length has no influence on the radiation pattern, provided the dipole length is shorter than λ_0. The rest of the configurations behave similarly, except the "perpendicular #3" and "#4" configurations, see Figure C.6, in which the radiation pattern changes. In both cases there is a null at broadside depending on the dipole length. Since for these configurations the radiation pattern also changed with the substrate thickness, it seems that the interaction of the radiated field with the EBG surface is responsible for these results.

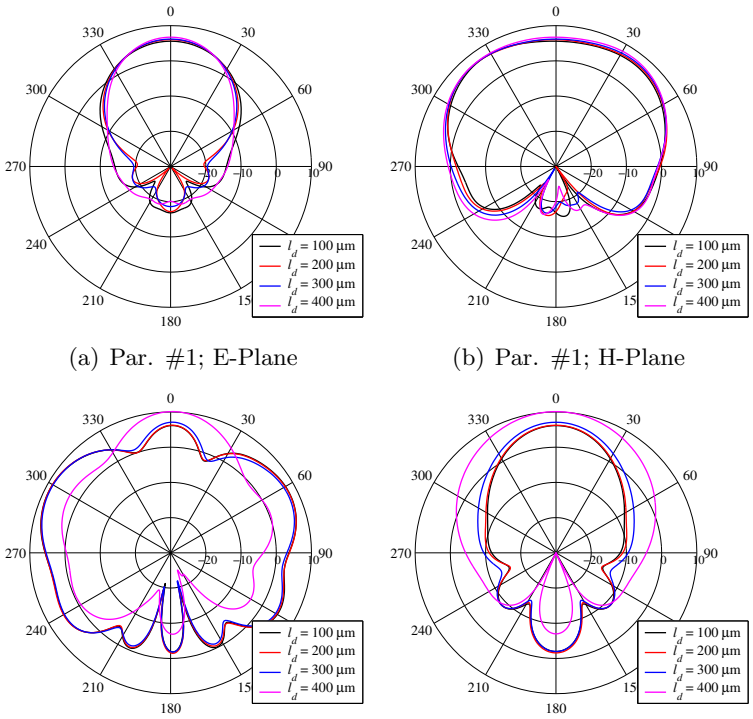

(a) Par. #1; E-Plane

(b) Par. #1; H-Plane

(c) Perp. #1; E-Plane

(d) Perp. #1; H-Plane

Figure 2.36: Radiation pattern of a printed dipole placed on top of a ZTT Fan EBG structure at the "parallel #1" and "perpendicular #1" symmetry positions as function of the length of the dipole. $h = 20\,\mu m$; $f = 500$ GHz.

2.6 Comparison between the different configurations

In the results presented above some similarities can be found between the results obtained with the different EBG structures which are now discussed.

With respect to the input impedance of the dipoles, all the EBG structures studied behave similarly. In all cases the input impedance is mainly determined by the orientation of the dipole with respect the dielectric bars in the top layer of the EBG. As a consequence, "parallel" configurations present very low input resistance. Conversely, "perpendicular" configurations show much higher input resistance. The difference between both orientations seems to be linked to the phase of the reflected wave under normal incidence. This phase is close to 180 deg for the "parallel" configurations, what justifies its

low input resistance.

The phase of the reflected wave under normal incidence can be used as a design tool in order to identify the orientations of the dipole which will have very low input impedance. If the phase is close to 180 deg, the EBG structure will short-circuit the antenna and reduce its input impedance. These configurations will be difficult to match using a high characteristic impedance line, such as the Coplanar Stripline. However, although the phase helps to understand the general behaviour, there are differences in terms of input impedance between configurations which have the same orientation. This indicates that the influence of the relative position of the dipole with respect to the surface of the EBG must also be taken into account.

Also for both EBG structures the use of a high dielectric constant material does not lead to a significant reduction of the size of the dipoles. Therefore, the increase of manufacturing complexity due to the use of the ceramic material with respect to the use of silicon is not justified for the EBG structures studied.

Regarding the radiation pattern, it is mainly determined by the scattering at the surface of the EBG and is difficult to predict a priori. In general, more directive radiation patterns are obtained with the woodpile structure. For both EBG structures, "parallel" configurations present normally higher directivities than the "perpendicular" ones. For the woodpile structure, "perpendicular" configurations need larger structures to avoid diffraction at the edges, due to the smaller attenuation of the fields in this direction of the surface of the EBG. For this EBG structure, the results obtained show that the size of the structure in terms of λ_0 determines the diffraction at the edges. This property counteracts the reduction of size achieved by using the ceramic material. With respect to the size, Fan structure needs a smaller number of periods in order to have a stabilized radiation pattern. The reason for this is the larger attenuation at the surface of the EBG. However, the interaction of the radiation with the structure is larger and for some configurations it is more sensitive to the substrate thickness and dipole length than the woodpile.

Chapter 3

Dipole fed by Coplanar Stripline on top of an EBG structure

3.1 Introduction

In the previous chapter the features of a dipole antenna placed on top of different EBG structures was studied. In particular the woodpile structure and Fan's structure were analysed. According to these results, the different symmetry positions of these structures present very different radiation and input impedance features.

However, the study carried out used ideally fed dipoles as radiating elements. In any real configuration the dipole will be connected to the rest of the circuitry via any kind of transmission line or waveguide that should be matched to the dipole impedance in order to reduce the losses. At the same time this transmission line will have an impact on the radiation pattern of the dipole, since it introduces an asymmetry and consequently will degrade the performance.

In this chapter, Coplanar Striplines (CPS) will be used to feed the dipoles and the matching features of some of the configurations discussed in the previous chapter will be studied. The main objective is to find the best configuration in terms of matching and radiation pattern to be used as our detecting element.

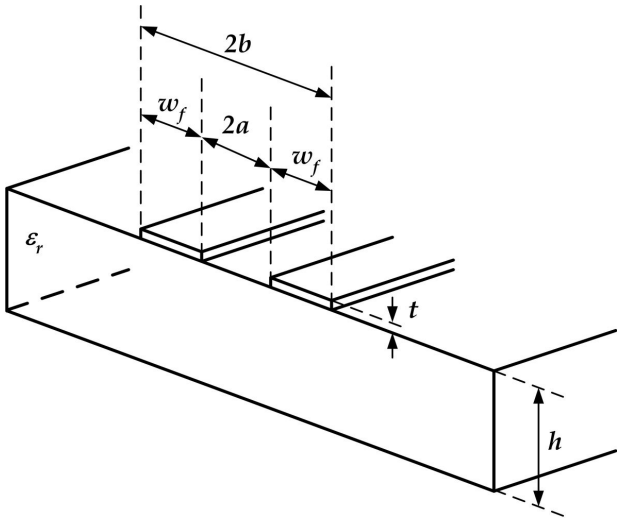

Figure 3.1: Geometry of the coplanar stripline (CPS).

3.2 Coplanar striplines

The coplanar stripline is a planar waveguide that consists of two metallic strips printed on a dielectric slab, see Figure 3.1. It presents some advantages, such as being a balanced transmission line and the possibility of series and shunt mounting of devices. The main drawback is that due to the lack of a ground plane, it can support two parasitic modes, TE_0 and TM_0 of a dielectric slab, which do not have a cut-off frequency. Since the electric field in the CPS is mainly parallel to the dielectric air interface, the TE_0 mode, which also has its electric field predominantly parallel to this interface, can be strongly excited at discontinuities.

The characteristic impedance of the Coplanar Stripline can be calculated using [Sim01]:

$$Z_0 = \frac{120\pi}{\sqrt{\epsilon_{eff}}} \frac{K\left(k'\right)}{K\left(k\right)}, \tag{3.1}$$

where K is the complete elliptical integral of the first kind. The other parameters are defined as follows:

$$k = \sqrt{1 - (a/b)^2}, \tag{3.2}$$

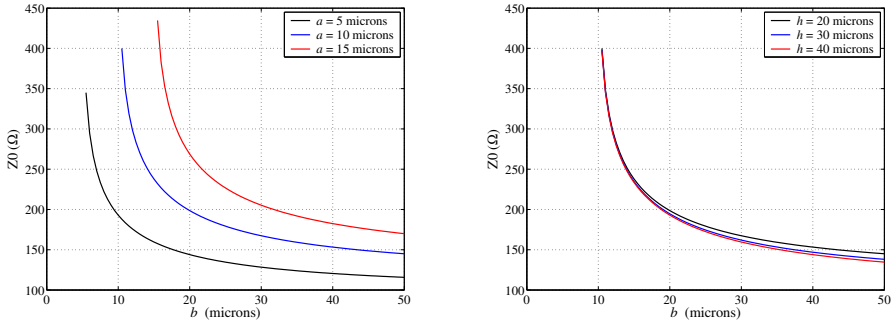

(a) (b)

Figure 3.2: Characteristic impedance of a CPS line printed on a quartz substrate. (a) $h = 20$ microns. (b) $a = 10$ microns.

$$k' = \sqrt{1 - k^2} = \frac{a}{b}, \tag{3.3}$$

$$\epsilon_{eff} = 1 + \frac{1}{2}(\epsilon_r - 1)\frac{K(k)}{K(k')}\frac{K(k_1')}{K(k_1)}, \tag{3.4}$$

and

$$k_1 = \sqrt{1 - \frac{sinh^2(\pi a/2h)}{sinh^2(\pi b/2h)}}. \tag{3.5}$$

In these formulas the metal strips have been supposed to have zero thickness.

Examples of the range of impedances that can be obtained with this transmission line are shown in Figure 3.2. The impedance of this line is quite high, which will require a high impedance of the dipole in order to be able to match it. The characteristic impedance depends inversely on the width of the strips and directly on the separation between them. It also decreases with the thickness of the substrate.

3.3 Dipole on quartz slab

As in the previous chapter and for the sake of comparison, first the matching of a dipole antenna printed on a quartz substrate and fed by a CPS will be studied. The dimensions of the CPS used have been taken arbitrarily as: $a = 10$ microns, $b = 30$ microns. Again, the same different thickness of the

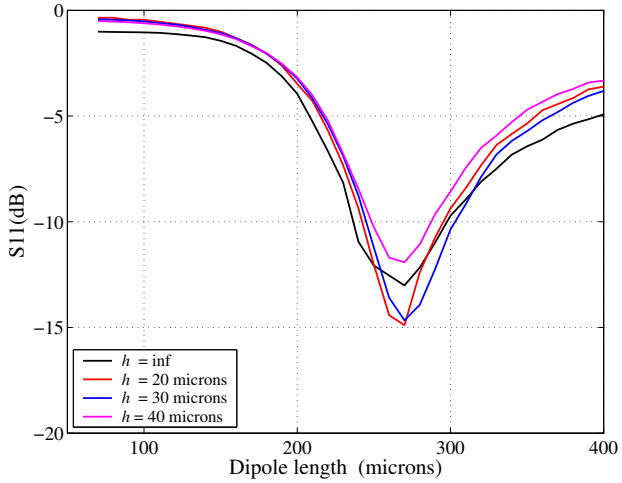

Figure 3.3: S_{11} of a dipole fed by a CPS and printed on a quartz substrate as a function of its length and the substrate thickness, h.

quartz substrate were considered, namely 20, 30, 40 microns and an infinite substrate. The characteristic impedance of these CPS calculated using eqn. (6.4) is 167.4, 162.0, 159.6 and 156.0 Ω respectively. If these lines are analysed using HFSS the impedances are 168.4, 163.1, 160.2 and 158.3 Ω, in good agreement with the theoretic values.

The results obtained when the length of the dipole is swept are shown in Figure 3.3. The matching peak has shifted to longer lengths with respect to the resonant length obtained when the dipole was fed by a lumped gap source (Table 2.3). The reason is that the transition from the CPS to the dipole adds some reactance that can only be compensated with a larger length. Similar results can be found in Coplanar Waveguides [Net03]. The increase in length will also improve the matching of the dipole, since the input resistance is larger for longer dipoles, see Figure 2.6. Moreover, for the lengths where the minimum of the reflection coefficient takes place, i.e. around 270 microns, the input resistance of the ideal dipole is higher than the characteristic impedance of the CPS. This justifies the better matching of the configuration built on a 20 microns thick substrate, since it presents the lowest characteristic impedance.

The radiation patterns corresponding to different configurations are shown in Figure 3.4. In this case the shortest length presents a very different radi-

ation pattern compared to the other configurations. Since this dipole is very mismatched, the standing wave created in the feeding lines degrades the radiation pattern. For the rest of the configurations the radiation patterns for different substrate thicknesses are very similar. If these patterns are compared with those obtained in the previous chapter, where an ideal dipole was used, certain degradation is observed, mainly in the H-Plane. The reason is the asymmetry caused by the feeding lines.

3.4 Dipole fed by CPS on top of silicon woodpile

In this study a quartz-backed dipole was placed on top of a woodpile structure and fed by a CPS. The initial dimensions of the CPS were the same used in the previous case, i.e. $a = 10$ microns, $b = 30$ microns. In this case the dipoles were 10 microns wide and were printed on 20, 30 and 40 microns substrates.

3.4.1 Matching

The results obtained for the different configurations are shown in Figure 3.5. As in the previous section, the minimum of the reflection coefficient shifts to larger dipole lengths with respect to the resonant lengths obtained using an ideal dipole, presented in Table 2.4. The reason is the same that was pointed out previously: the discontinuity at the end of the CPS creates a capacitance that shifts the resonant length to longer values.

In the previous chapter it was shown that the input impedance of an ideal dipole on top of a woodpile structure in any of the "parallel" configurations presented very low input impedance, due to the short-circuiting effect of the woodpile structure. This result is in agreement with the matching results, since it is not good for any of these configurations. Also the matching improves when the substrate thickness increases, what is also in agreement with the increasing input impedance of the dipoles for thicker substrates, obtained in the previous section. Note that although the impedances at resonance computed in the previous chapter were very low, the shift to larger resonant lengths increase the input resistance and the S_{11} for some configurations can be improved up to -10 dB.

On the other hand, the "perpendicular" configurations present better matching levels, specially the "solid-solid" and "void-solid" configurations. In these two cases, and for these particular dimensions of the CPS lines, the best matching results are obtained with the thinner substrates, i.e. 20 microns.

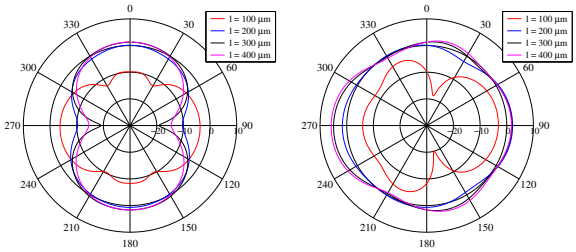

(a) $h = 20$ microns (b) $h = 20$ microns

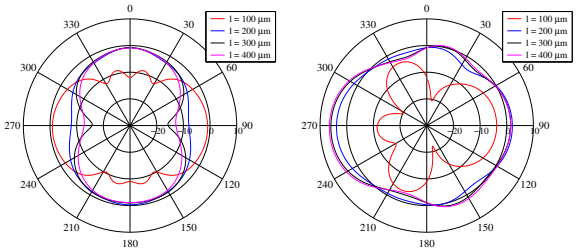

(c) $h = 30$ microns (d) $h = 30$ microns

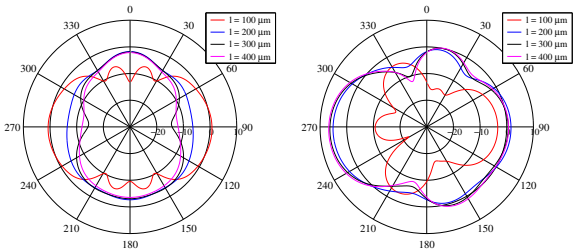

(e) $h = 40$ microns (f) $h = 40$ microns

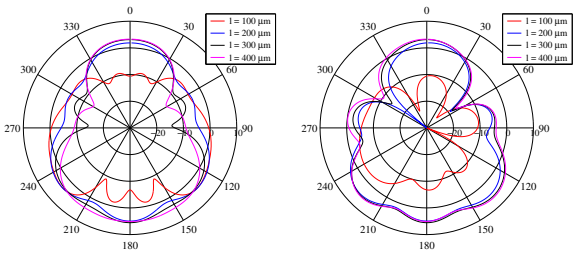

(g) $h = inf$ (h) $h = inf$

Figure 3.4: Radiation pattern of a dipole fed by a CPS and printed on a quartz substrate as a function of its length, l, and of the substrate thickness, h. $f = 500$ GHz.

Although the input resistance at resonance is larger for thicker substrates, as it was shown in Table 2.4, it increases much faster for thinner substrates, what helps to the matching of these configurations.

In the "solid-void" and "void-solid", there is not a clear resonance for the thicker substrates. This is related with the fact that the input impedance in these configurations was always capacitive, and therefore the reactance of the discontinuity takes the configurations even further away from resonance.

The matching results that have been presented correspond to a particular CPS line. Actualy, the "perpendicular solid" solid configuration is so well matched because the dimensions on the line were very close to the optimum dimensions for this configuration, as it will be shown in the next section. If another line were used, the results would be different and another "perpendicular" configuration could be better matched. However, for the "parallel" configurations it is not possible to achieve the same return loss levels, since the input impedance of the dipole is very low.

3.4.2 Radiation pattern

With respect to the radiation patterns, results corresponding to the "parallel void-void" and "perpendicular solid-solid" symmetry positions are presented in Figure 3.6 and 3.7. These two configurations were chosen as representatives of the two orientations since the "parallel void-void" showed a quite good radiation pattern when a dipole was studied in the previous chapter and the "perpendicular solid-solid" shows good matching features.

As in the case of a dipole on quartz, the matching of the configuration plays a very important role on the shape of the radiation pattern, since the standing wave created in the CPS when the dipole is not matched interferes with the radiation pattern of the dipole.

In the "parallel void-void" configuration, if the substrate is 20 microns thick, the return loss are quite low for a 100 microns long dipole, see Figure 3.5(g), and the radiation pattern is very bad in this case. If the dipole is enlarged up to 200 microns, the radiation pattern improves. For longer dipoles, i.e. 300 and 400 microns, the radiation pattern is nearly the same, due to the similar return losses. In these later cases the radiation pattern shows several nulls in the H-plane due to the interference pattern. The results for the other thickness are similar to the ones with a thickness of 20 microns.

For the "perpendicular solid-solid" configuration the matching, shown in Figure 3.5(b), is better except for the shortest dipole (100 microns). There-

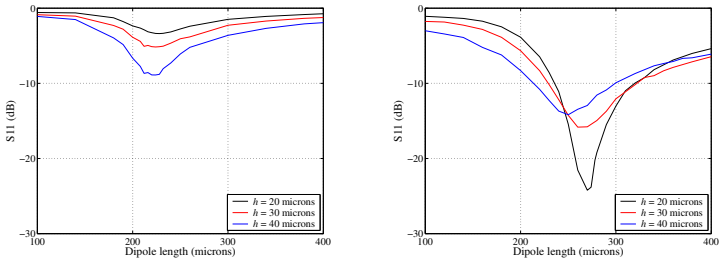

(a) Par. solid-solid (b) Perp. solid-solid

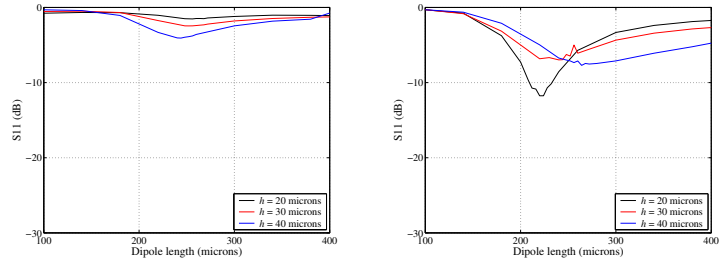

(c) Par. solid-void (d) Perp. solid-void

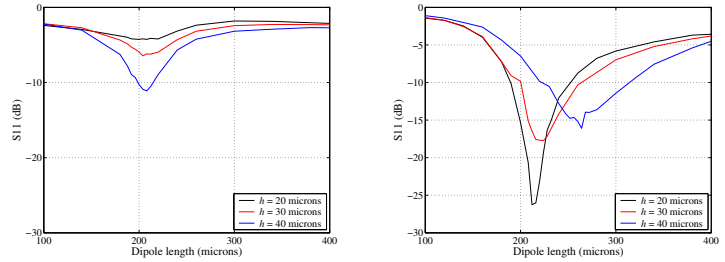

(e) Par. void-solid (f) Perp. void-solid

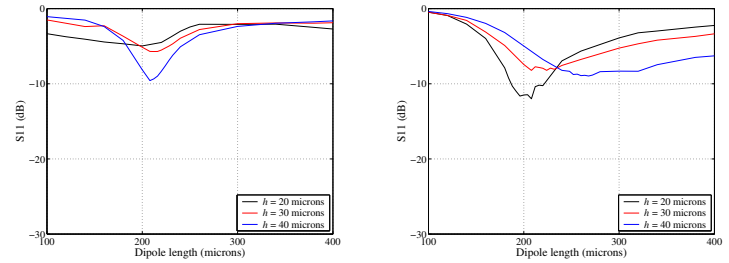

(g) Par. void-void (h) Perp. void-void

Figure 3.5: S_{11} of a dipole fed by a CPS and placed on top of a silicon woodpile in the different symmetry positions. $f = 500$ GHz.

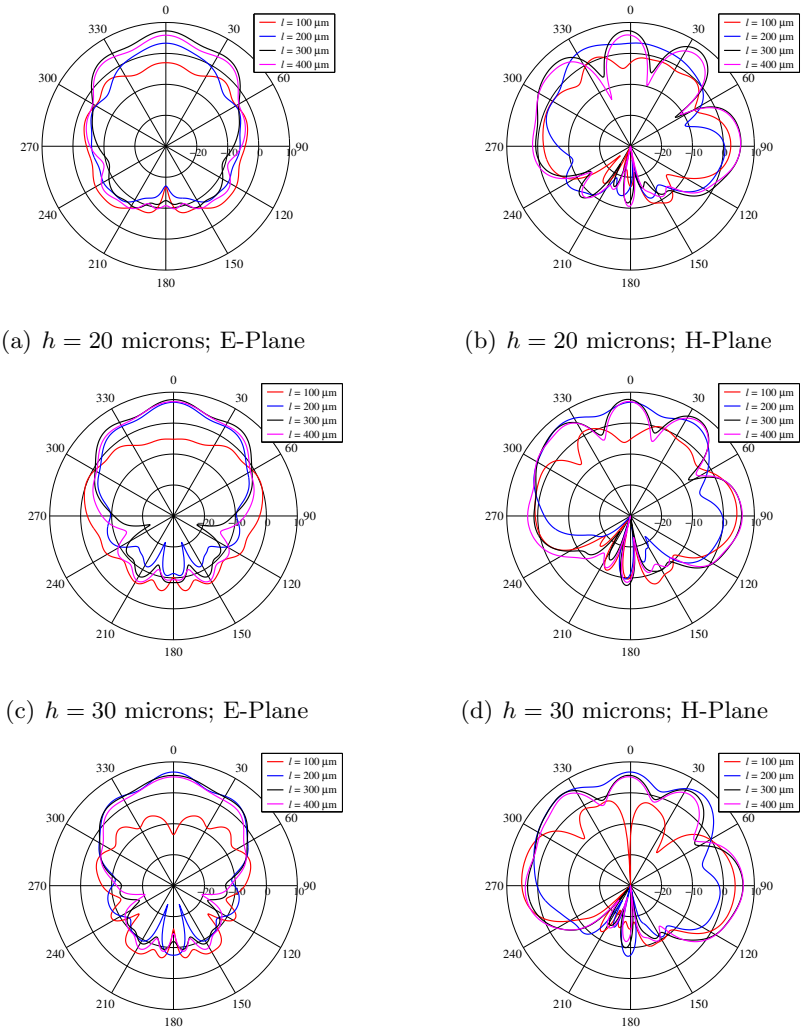

(a) $h = 20$ microns; E-Plane

(b) $h = 20$ microns; H-Plane

(c) $h = 30$ microns; E-Plane

(d) $h = 30$ microns; H-Plane

(e) $h = 40$ microns; E-Plane

(f) $h = 40$ microns; H-Plane

Figure 3.6: Radiation pattern a dipole fed by a CPS and placed on top of a silicon woodpile in the "parallel void-void" symmetry position as a function of its length and of the substrate thickness, h. $f = 500$ GHz.

fore, the radiation patterns are more similar and their degradation is smaller. However, the radiation patterns corresponding to the thicker substrates show

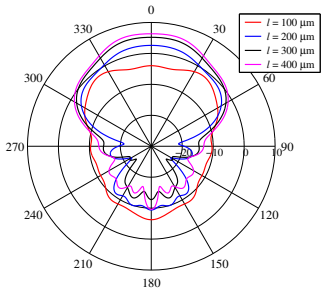

(a) $h = 20$ microns; E-Plane

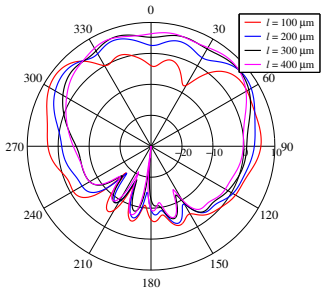

(b) $h = 20$ microns; H-Plane

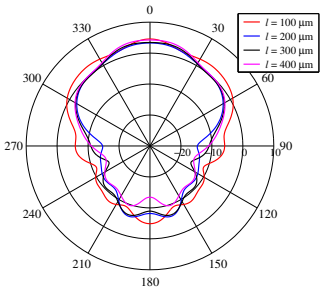

(c) $h = 30$ microns; E-Plane

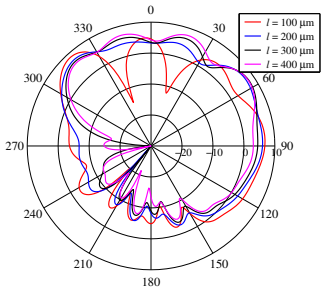

(d) $h = 30$ microns; H-Plane

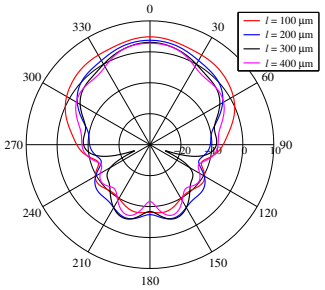

(e) $h = 40$ microns; E-Plane

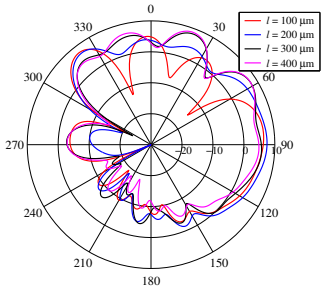

(f) $h = 40$ microns; H-Plane

Figure 3.7: Radiation pattern a dipole fed by a CPS and placed on top of a silicon woodpile in the "perpendicular solid-solid" symmetry position as a function of its length and of the substrate thickness, h. $f = 500$ GHz.

deeper nulls due to the fact that they are worse matched than the configurations using thinner substrates.

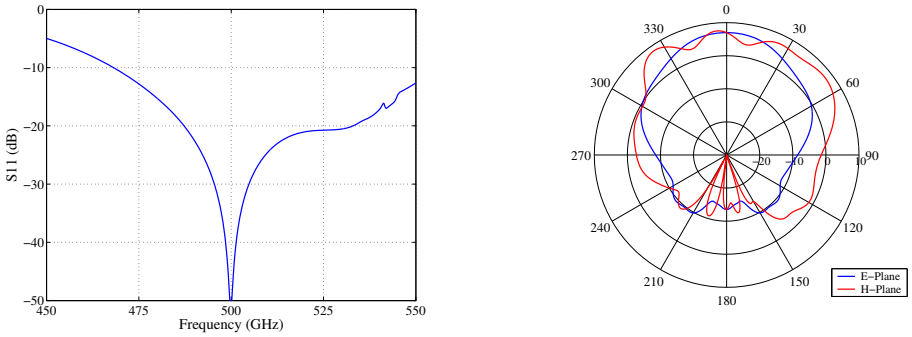

(a) (b)

Figure 3.8: (a) S_{11} parameter of the optimised dipole fed by CPS line configuration. (b) Radiation pattern at $f = 500$ GHz.

3.4.3 "Perpendicular solid-solid" symmetry position

The previous results show that it is difficult to achieve a good matching of a dipole placed in the "parallel" configurations. Moreover, the radiation of these configurations is largely degraded by the standing wave created in the feeding line. Thus, these configuration present a worse radiation pattern than the "perpendicular" configurations, although the radiation pattern of the dipole without feeding lines was better. For these reasons these configurations were discarded and it was decided to select a "perpendicular" configuration.

From the "perpendicular" configurations, the "perpendicular solid-solid" symmetry position was the selected one, since its radiation pattern was less dependent on the woodpile dimension and substrate parameters than the "void-solid" configuration, the other configuration that showed good matching features.

Matching

The matching results presented for the "perpendicular solid-solid" configuration were not optimum, since they were computed with certain CPS parameters. Although according to the input impedance results, similar levels of return loss could be obtained with other substrate thicknesses, we decided to use this thin substrate in order to avoid any possible substrate mode excita-

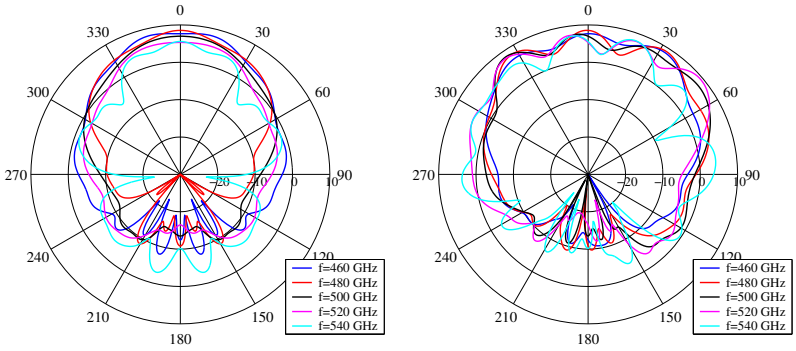

(a) E-Plane (b) H-Plane

Figure 3.9: Radiation pattern of the optimised dipole fed by CPS line as a function of frequency.

tion, since according to [Ale83] the power in substrate modes is small only if $h << \lambda_0/10$. Moreover, the substrate with thickness 20 microns already showed very good matching performance, what made the optimisation process faster. Finally, this substrate was still within practical limits in terms of its fabrication.

The return loss of the configuration was optimised by modifying the CPS parameters, a and b, and the dipole length. The optimum values were found to be $a = 10$ microns, $b = 34$ microns and $l = 235$ microns. The S_{11} of this configuration is shown in Figure 3.8(a). The return loss at the design frequency, 500 GHz, is close to 50 dB.

Radiation pattern

With respect to the radiation pattern of this configuration at the design frequency, it is shown in Figure 3.8(b). Although it is slightly distorted by the feeding circuit, it is quite symmetric with low back radiation levels. Note that since the structure is finite, $11 \times 11 \times 2$ periods, in a real configuration these levels should be smaller, due to the reduction of the diffraction at the edges.

The frequency dependence of the radiation pattern is studied in Figure 3.9 for several frequencies inside the gap. For frequencies higher than 500 GHz the radiation pattern tends to degrade faster than for lower frequencies. This way, the pattern at 540 GHz shows higher levels of back radiation, and deeper nulls. Note that this degradation is not caused by the bad matching, since the

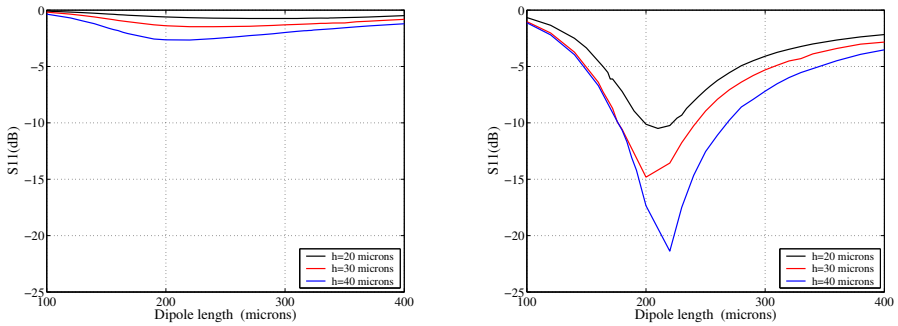

(a) Par. solid-solid (b) Perp. solid-solid

Figure 3.10: S_{11} of a dipole fed by a CPS and placed on top of a ZTT woodpile in different symmetry positions. $f = 500$ GHz.

S_{11} is increases faster for lower frequencies, but for the interaction with the EBG structure. Note that a similar radiation pattern was obtained for the dipole without feeding lines, see Figure 2.21. If the frequency is lower than the central frequency the radiation pattern is slightly more directive. This effect was already observed in Chapter 2 when the frequency dependence of the input impedance and of the radiation pattern was studied.

3.5 Dipole fed by CPS on top of ZTT woodpile

As it was concluded in the previous chapter, the performance of a dipole antenna placed on top of a ceramic woodpile was similar to its performance if a silicon woodpile is used. In this case, and based on the results previously obtained for the silicon woodpile case, only a limited number of configurations will be studied. The two selected configurations are the "parallel void-void" and the "perpendicular solid-solid", since they represent both orientations and limit cases in terms of placement.

3.5.1 Matching

According to the input impedance results shown in Chapter 2, the "parallel void-void" configuration should be difficult to match, due to the very low impedance of a dipole placed at it (see Table 2.25). Conversely, the "perpendicular solid-solid" will be easier to match since its input impedance is much higher.

The results obtained in this section, see Figure 3.10, verify our assumptions. The return loss for the "parallel void-void" configuration is not better than 3 dB, even for the thicker substrates. On the contrary, the "perpendicular solid-solid" configuration allows achieving S_{11} values lower than -20 dB. The dimensions of the used CPS are the same found to be optimum for the silicon woodpile case, i.e. $a = 10$ microns, $b = 34$ microns, $w = 10$ microns. These dimensions could be optimised in order to improve the matching as they were in that case.

These results are consistent with those obtained in the previous section for the silicon woodpile. In both cases the "perpendicular" configurations can be matched, whereas the "parallel" configurations can not. In the "parallel" case, the return loss is better in the silicon woodpile, due to the higher input impedance predicted in section 2.3.2.

3.5.2 Radiation pattern

With respect to the radiation patterns obtained with both configurations, they are shown in Figure 3.11 and Figure 3.12, for the "parallel void-void" and the "perpendicular solid-solid" configurations respectively. In both cases the size of the analysed woodpile structures was $6 \times 6 \times 2$ periods, since larger configurations could not be analysed due to the high dielectric constant. The levels of back radiation obtained are larger than with the silicon woodpile, due to the smaller size of the structure in terms of λ_0.

For the "parallel void-void" configuration the radiation patterns are different when the length of the dipole is changed. This is due to the bad matching of the configuration, which makes the radiation pattern depend on the interference with the standing wave generated in the feeding lines. Since the matching did not improve significantly by increasing the thickness of the substrate, neither do the radiation patterns.

In the "perpendicular solid-solid" configuration the radiation patterns are more similar when the length of the dipole changes, due to the higher return losses. Only a 100 microns long dipole gives a different radiation pattern, due to the much worse matching. This configuration can be better matched when the thickness of the substrate increases. However, this is not shown in the radiation patterns, since the return loss are already high enough not to affect them.

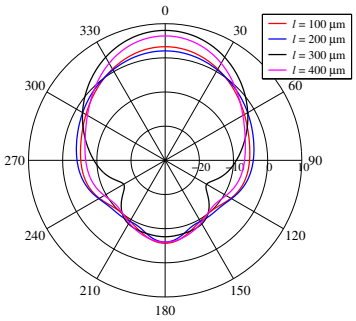

(a) $h = 20$ microns; E-Plane

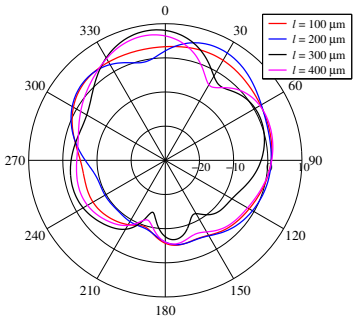

(b) $h = 20$ microns; H-Plane

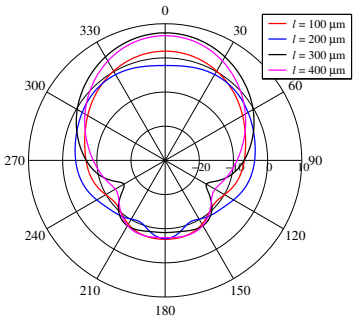

(c) $h = 30$ microns; E-Plane

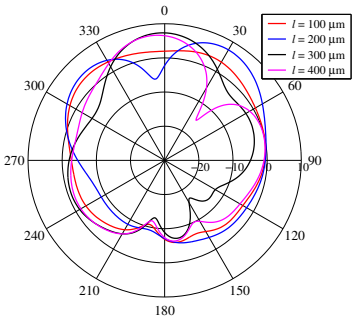

(d) $h = 30$ microns; H-Plane

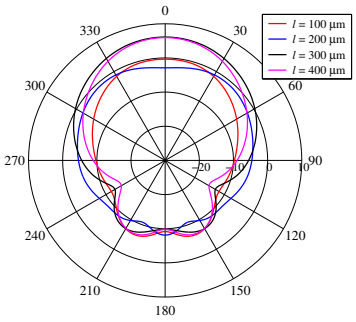

(e) $h = 40$ microns; E-Plane

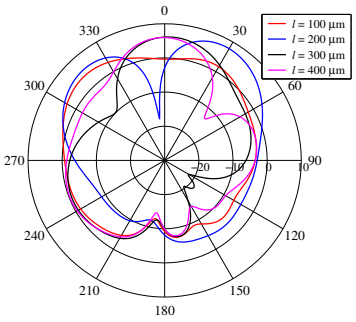

(f) $h = 40$ microns; H-Plane

Figure 3.11: Radiation pattern a dipole fed by a CPS and placed on top of a ZTT woodpile in the "parallel void-void" symmetry position as a function of its length and of the substrate thickness, h. $f = 500$ GHz.

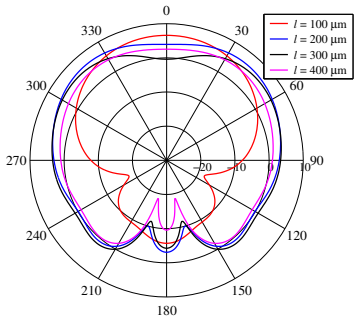

(a) $h = 20$ microns; E-Plane

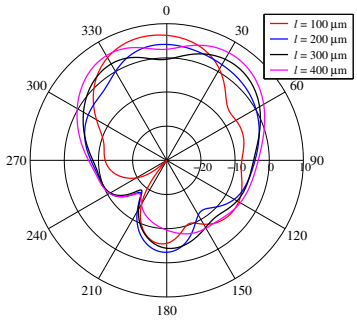

(b) $h = 20$ microns; H-Plane

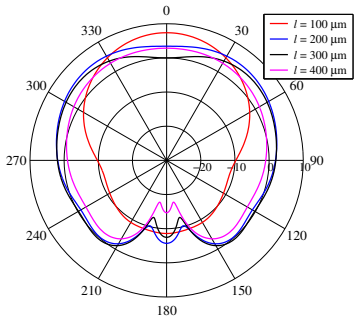

(c) $h = 30$ microns; E-Plane

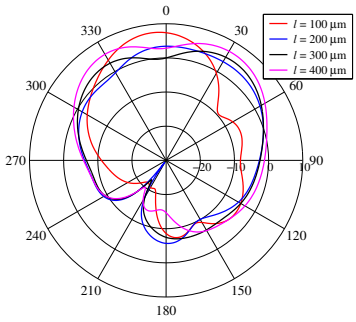

(d) $h = 30$ microns; H-Plane

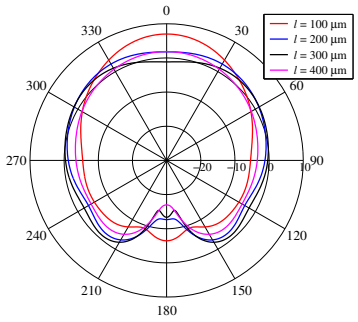

(e) $h = 40$ microns; E-Plane

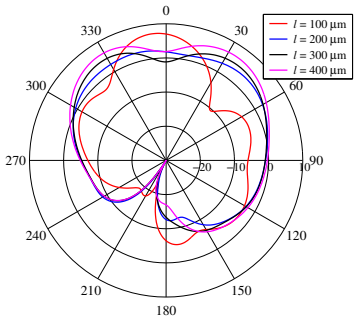

(f) $h = 40$ microns; H-Plane

Figure 3.12: Radiation pattern a dipole fed by a CPS and placed on top of a ZTT woodpile in the "perpendicular solid-solid" symmetry position as a function of its length and of the substrate thickness, h. $f = 500$ GHz.

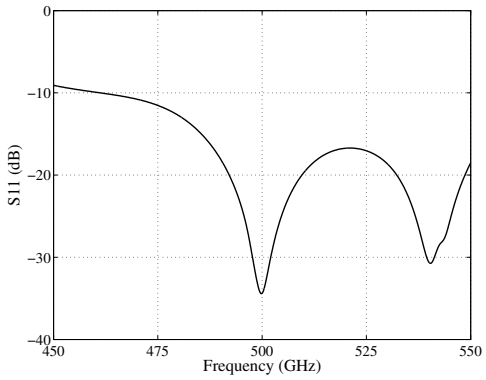

(a)

Figure 3.13: S_{11} parameter of the optimised dipole fed by CPS line on top of a ZTT woodpile.

3.5.3 "Perpendicular solid-solid" symmetry position

In order to study the frequency dependence of the return loss and of the radiation pattern, the "perpendicular solid-solid" configuration has been selected due to its good matching features. In particular, the thickness of the substrate was taken as 40 microns and the dipole length was 230 microns, so that the matching was best.

The S_{11} parameter obtained for this configuration is presented in Figure 3.13. Although there is a minimum of return loss at 500 GHz, the curve could be shifted, so that a larger bandwidth was achieved.

With respect to the frequency dependence of the radiation patterns, results at different frequencies are shown in Figure 3.14. Although the bandwidth of the ceramic woodpile is much larger than the bandwidth of the silicon woodpile, the bandwidth in terms of radiation features of the dipole antenna placed on top of it has not improved. As for the Si woodpile, the radiation patterns at frequencies larger than 500 GHz tend to degrade faster than for lower frequencies.

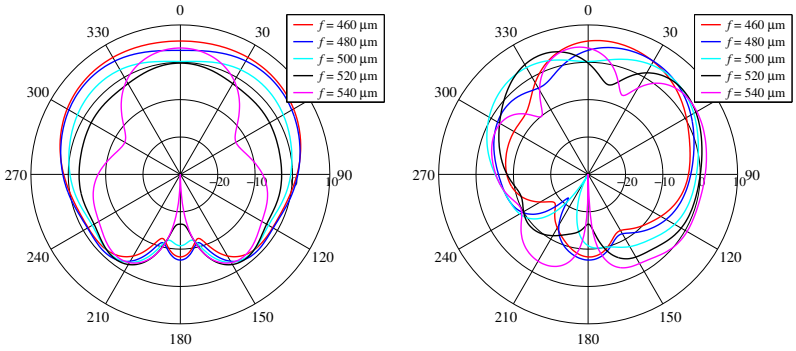

(a) E-Plane (b) H-Plane

Figure 3.14: Radiation pattern of the optimised dipole fed by CPS line on top of the ZTT woodpile as a function of frequency.

3.6 Dipole fed by CPS on top of ZTT Fan structure

As for the woodpile structure, the input impedance of a dipole placed on top of Fan structure depends very strongly on the type of symmetry position on which it us placed. If it is placed on a "parallel" symmetry position, the dipole is nearly short circuited, whereas if it is placed on a "perpendicular" symmetry position the input impedance is much higher. Thus, "perpendicular" configurations seem to be much better candidates to be well matched when fed by CPS lines.

However, for these configurations, there is another circumstance that must be taken into account. The surface of the structure is such that the dielectric distribution under the lines can break the symmetry of the transmission line, distorting its mode. In order to avoid this problem, the configuration "perpendicular #1" has been selected, since in it the feeding lines are equally separated from the dielectric parts of the surface. For the comparison purposes the "parallel #1" configuration will also be studied. See Figure 3.15 for a schematic drawing of both configurations.

3.6.1 Matching

The matching obtained for both configurations as a function of the length of the dipole and of the thickness of the substrate is shown in Figure 3.16. As it was expected the "parallel #1" configuration is very mismatched, as its

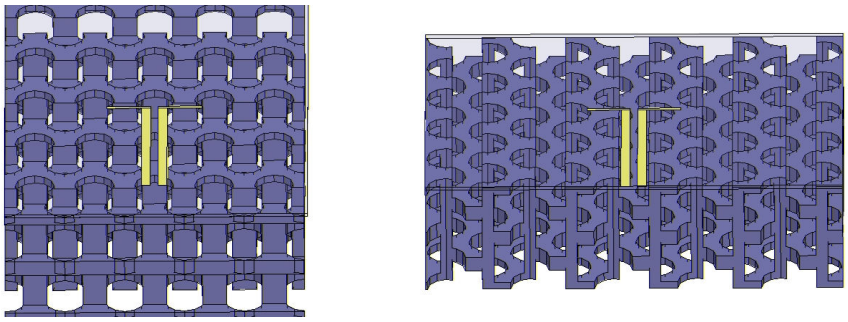

(a) Par. #1 (b) Perp. #1

Figure 3.15: Configurations of the dipole on top of Fan structure that will be analysed.

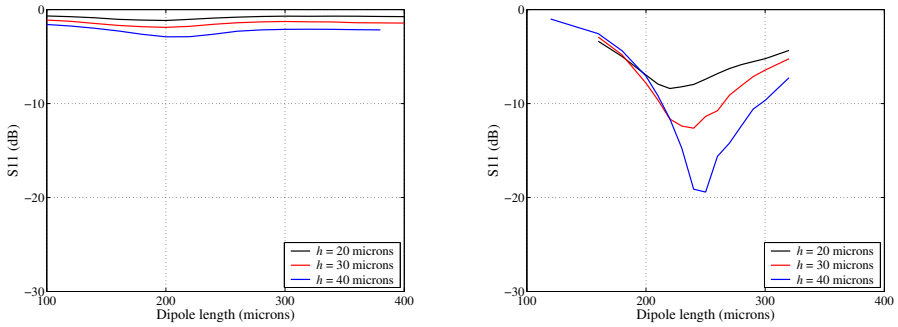

(a) Par. #1 (b) Perp. #1

Figure 3.16: S_{11} of a dipole fed by a CPS and placed on top of a ZTT Fan EBG structure in different symmetry positions. $f = 500$ GHz.

input impedance was very low, see Table 2.8. The minimum S_{11} with this configuration was -4 dB, obtained with the thickest substrate, 40 microns.

With respect to the "perpendicular #1" configuration, the return losses obtained are much higher, being a maximum for a 40 microns thick substrate and a dipole length of 250 microns. In both cases the matching improves when the thickness of the substrate is increased, as it was predicted by the input impedance results shown in Chapter 2 (Table 2.8).

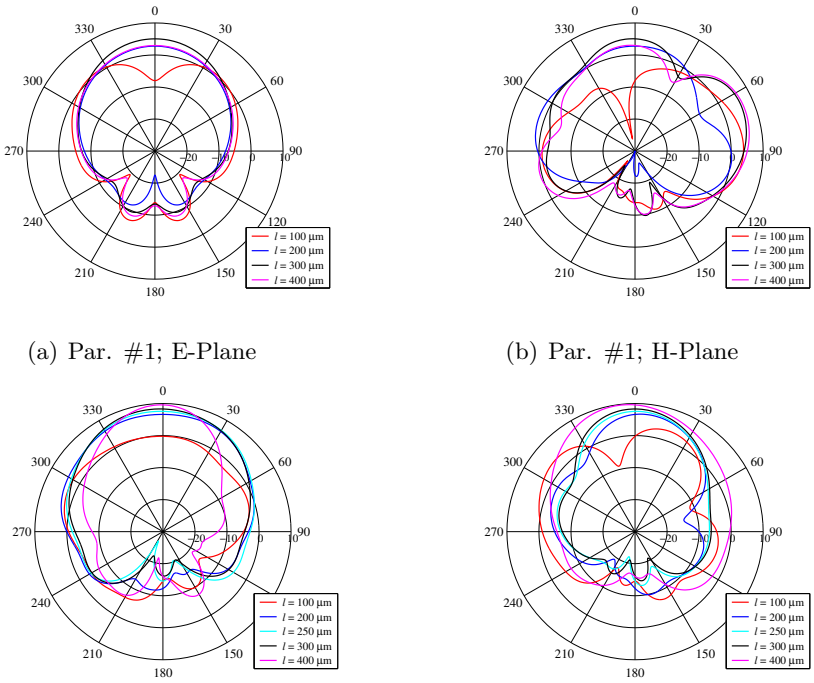

(a) Par. #1; E-Plane

(b) Par. #1; H-Plane

(c) Per. #1; E-Plane

(d) Per. #1; H-Plane

Figure 3.17: Radiation pattern a dipole fed by a CPS and placed on top of a ZTT Fan structure as a function of its length. $h = 40\,\mu m$; $f = 500$ GHz.

3.6.2 Radiation pattern

Regarding the radiation patterns obtained with these configurations, they are shown in Figure 3.17 for a quartz substrate thickness of 40 microns and different dipole lengths. Since in the "perpendicular #1" configuration it was not possible to use any symmetry plane, the largest configuration that could be analysed was $5 \times 5 \times 2$ periods. As in the previous cases, the radiation patterns obtained with very mismatched configurations, such as the "parallel #1" are quite different. Conversely, the patterns corresponding to the "perpendicular #1" configuration are more similar thanks to the better matching levels. In this case, the radiation pattern at resonance has also been included, showing similar features than those corresponding to other lengths.

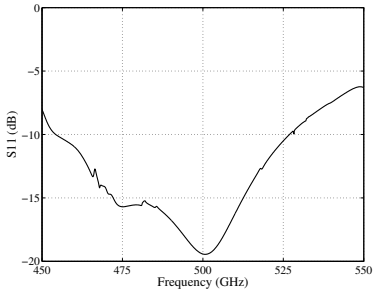

(a)

Figure 3.18: S_{11} parameter of the optimised dipole fed by CPS line on top of a ZTT Fan structure at the "perpendicular #1" symmetry position.

3.6.3 "Perpendicular #1" configuration

Since this configuration showed good matching features when the thickness of the quartz substrate was 40 microns, it has been studied in detail. The length of the dipole has been set to 250 microns since this corresponds to the best return loss.

The S_{11} of this configuration is presented in Figure 3.18. The -10 dB bandwidth corresponds to the range between 455 and 525 GHz.

The radiation patterns corresponding to different frequencies are shown in Figure 3.19. In this case the maximum directivity takes place for a frequency higher than 500 GHz. However, the H-Plane is slightly distorted by the feeding line. For frequencies lower than 500 GHz the directivity is lower but the pattern keeps on having a non-distorted shape.

3.7 Effect of the losses on the matching and radiation features

In the previous results the materials used in the EBG structures were considered lossless. In the case of silicon, this assuption is not far from reality, since it is a low loss material at the design frequency [HB03]. In particular, $tan\delta = 1.7 \times 10^{-4}$ is the meassured value at 500 GHz of the silicon waffers that were used to manufacture the woodpile structure. Conversely, ZTT presents much higher $tan\delta$, of the order of 10^{-2}.

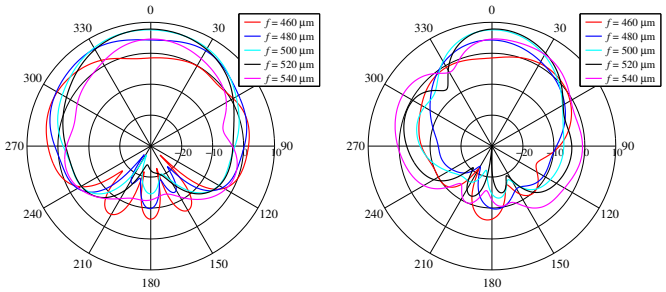

(a) E-Plane (b) H-Plane

Figure 3.19: Radiation pattern of the optimised dipole fed by CPS line on top of a ZTT Fan structure at the "perpendicular #1" symmetry position as a function of frequency.

In order to check the effect of these losses on the performance of the different EBG structures the configurations previously considered were analysed including them. The change in the S_{11} of the configurations is shown in Figure 3.20. For the silicon woodpile, the S_{11} is nearly identical in both cases. Only the resonance at 500 GHz is deeper when no losses are included. For the structures using the ZTT material, the differences are larger, due to the higher losses of this material. However, the changes are not important.

The directivity pattern corresponding to the lossless configuration and gain pattern of the configuration including losses are compared in Figure 3.21. For the three configurations there is hardly any difference between the two patterns. The power losses are summarised in Table 3.1. The reason for the low losses obtained, even with quite high $tan\delta$ materials is that these estructures work as reflectors. Since the electromagnetic fields do not propagate inside the structure they do not interact with the lossy material and therefore the losses are low.

EBG structure	$\boldsymbol{tan\delta}$	**Losses (dB)**
Silicon woodpile	1.7×10^{-4}	0.02
ZTT woodpile	1.0×10^{-2}	0.20
ZTT Fan	1.0×10^{-2}	0.22

Table 3.1: Losses due to the use of lossy dielectric materials.

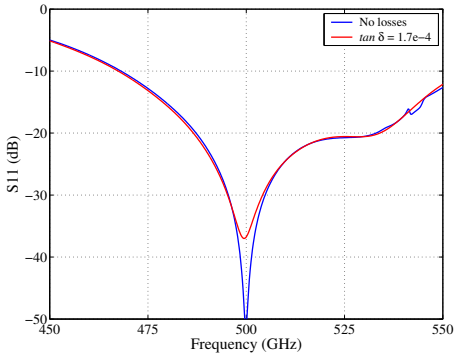

(a) Si woodpile

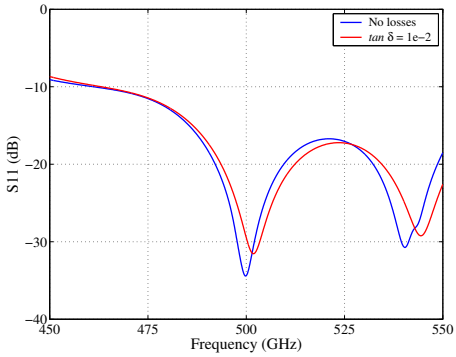

(b) ZTT woodpile

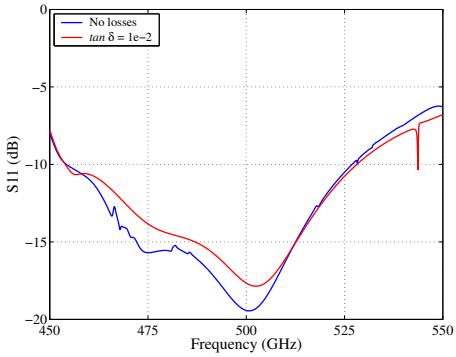

(c) ZTT Fan

Figure 3.20: Comparison of the S_{11} of the different configurations studied with and without losses.

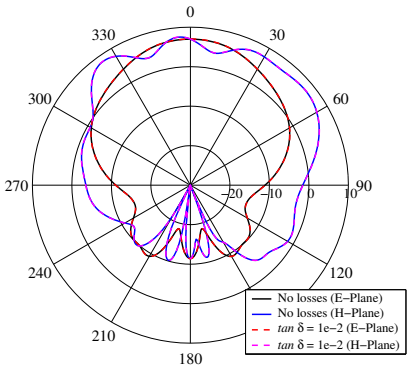

(a) Si woodpile

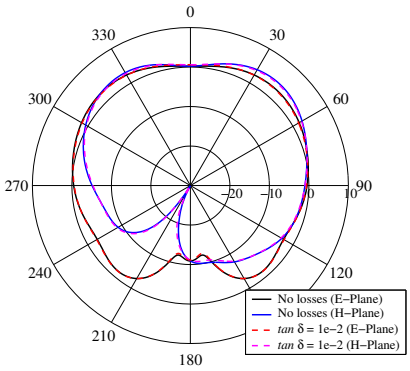

(b) ZTT woodpile

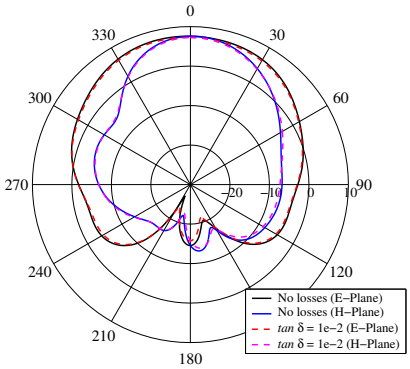

(c) ZTT Fan

Figure 3.21: Comparison of the directivity and gain patterns of the different configurations studied including losses.

Chapter 4

Modifications of the woodpile structure for the improvement of its performance as substrate for dipole antennas

4.1 Motivation

As it was concluded in the previous chapter, the different symmetry positions of the woodpile structure present distinct features when a dipole is placed at them. As a general rule, the "perpendicular" ones allow getting a good matching, whereas the radiation pattern obtained with them is not the best one. Conversely, the "parallel" configurations have a good radiation pattern while being difficult to match. However, even in this last case, the radiation pattern is not symmetric, the H-plane being broader than the E-Plane.

The objective of this chapter is to try to modify the woodpile structure, so that a good radiation pattern and a matched configuration are simultaneously obtained. The starting point of this study will be the "parallel void-void" configuration. In order to reduce the fabrication complexity, the type of modifications studied will only affect the upper most layer of the woodpile.

As it was mentioned in Chapter 2, when a dipole is placed on top of a woodpile in the "parallel void-void" symmetry position, the electric field concentrates in the bars parallel to the dipole, especially in those closer to it (see Figure 4.1). Therefore, the radiation pattern of this configuration

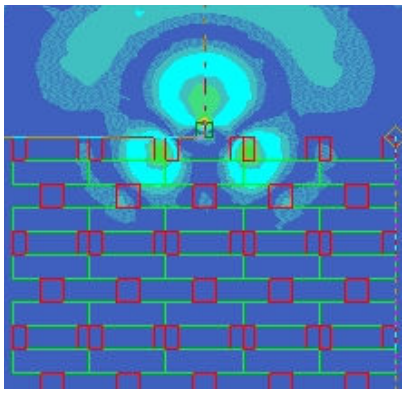

Figure 4.1: Electric field distribution in the plane perpendicular to the dipole (H-Plane). "Parallel void-void" symmetry position.

can be seen as the combination of the field radiated by the dipole and the field scattered at these bars. This creates an interference patter that for the dimensions of the optimum woodpile, give rise to a quite asymmetric radiation patter. Modifying the distance between these bars and the dipole might be a way to symmetrize the radiation pattern.

As in the previous chapters, first an ideal dipole will be used as radiating element, and changes in both its radiating features and input impedance will be analysed. Afterwards a more real configuration, in which the dipole is fed by a coplanar stripline will be studied.

4.2 Proposed configurations

As it was just mentioned, the proposed configuration is based on the displacement of the silicon bars closest to the dipole (see Figure 4.2). Since the radiation pattern depends on the position of these bars, given by the distance s, there should be an optimum value of this parameter that creates a symmetric beam.

If the distance that these bars are moved is large enough, they will be very close or even overlap their neighbouring bars. If the gap between the bars is very narrow the fabrication of these structures can be difficult. For instance, in the case of the optimised silicon woodpile, the gap is 1.9 microns, 11.9, 21.9 and 31.9 microns for values of s of 160, 150, 140 and 130 microns

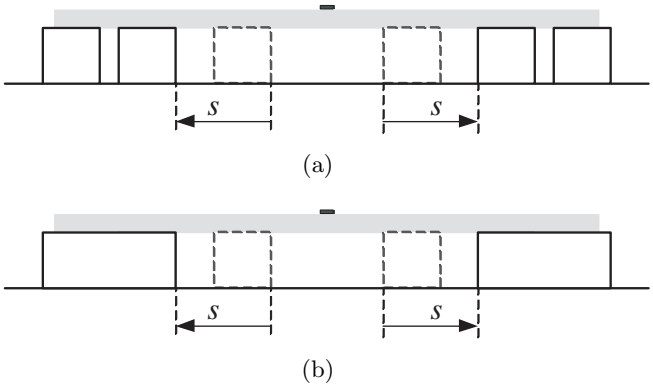

Figure 4.2: Schematic showing two proposed modifications. (a) Separated bars (b) Thicker bars. The grey area corresponds to the quartz substrate and the black one to the dipole and feeding lines. The dashed bars are those in the original woodpile whereas the solid ones are those in the modified woodpile.

respectively. It is technologically challenging, or maybe even impossible at least for the smallest values, to create these gaps. A feasible alternative to this configuration is based on connecting both bars, as it is shown in Figure 4.2(b). This is equivalent to removing the bars closest to the dipole and increasing the thickness of the second bars. The relation between both configurations, i.e. separated bars and thicker bars, will be studied.

The aforementioned configurations affect to a complete bar. An improvement of them is based on the modification of the bars just in the area closest to the dipole creating a 2D cavity. This localised defect has the advantage of leaving the rest of the woodpile unaffected. As a drawback of this configuration, its fabrication will require the use of etching [Azc03], since it is not possible to manufacture it using simpler methods, such as that proposed in [Gon02]. Examples of this kind of arrangements are given in Figure 4.3, where (a) represents the separated bar configuration and (b) the thicker bar configuration. In this case not only the displacement of the bars, s, but also the size of the cavity, d, can be used to improve the configurations. It is expected that for large enough values of d the performance of this arrangement will be similar to the previous one.

In order to check the effect of these modifications on the transmission performance of the woodpile structure, the transmission under normal insidence through two perturbed woodpiles, in which two bars have been displaced 80

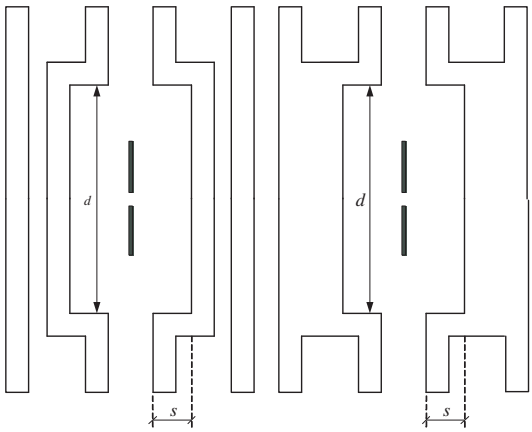

Figure 4.3: Dipole fed on modified woodpile 2D cavity configuration, top view. The black rectangles correspond to the dipole arms. The substrate has been removed for the sake of improved visibility.

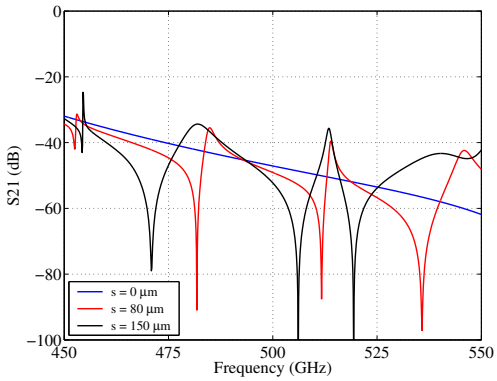

Figure 4.4: Transmission through 3 layers of a silicon woodpile structure. The s=0 curve corresponds to the unperturbed woodpile.

and 150 microns has been analysed. The results corresponding to a plane wave parallel to the bars of the first woodpile layer are presented in Figure 4.4. The main differences that can be observed are some resonances which make the transmission level be higher or lower than those corresponding to the unperturbed woodpile. In any case the transmission is lower than -30 dB.

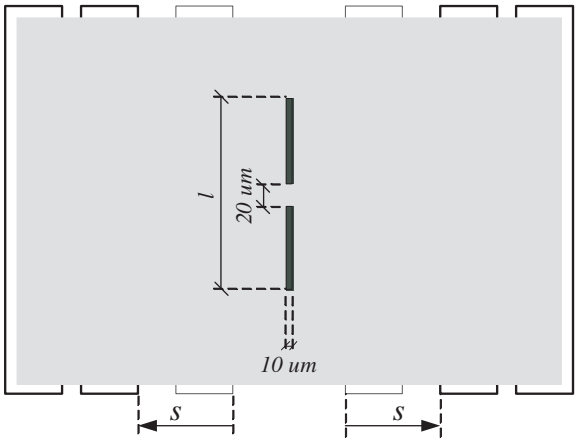

Figure 4.5: Schematic showing the dipole fed by lumped gap source configuration. The grey area corresponds to the quartz substrate and the black one to the dipole. The dashed bars are those in the original woodpile whereas the solid ones are those in the modified woodpile.

4.3 Ideal dipole on modified woodpile

A dipole fed by a lumped gap source, i.e. without feeding lines, has firstly been considered in order to study the improvements on the radiating features when the woodpile structure is modified. The dimensions that were considered for the dipole are shown in Figure 4.5. The thickness of the quartz substrate is 20 microns. The woodpile dimensions are those of the optimised silicon woodpile, i.e. $a = 232.9$ microns, $c = 1.22$, $d_1 = d_2 = 71$ microns.

In this case, configurations that affect complete bars are going to be studied. As a consequence of the modification in the configuration both the radiation pattern and the input impedance of the dipole will change. The results obtained are summarised and commented in the following sections.

4.3.1 Radiation pattern

The changes in the radiation pattern when the bars are moved are presented in Figure 4.6. As it was desired, the H-plane becomes narrower as the distance between the bars increases. At the same time the E-plane slightly broadens and the directivity increases.

In order to check the symmetry of the radiation patterns obtained, several

of them are shown in Figure 4.7. For small displacements, $s = 40$ microns in Figure 4.7(a), the H-Plane is still broader than the E-Plane. The optimum results are obtained for $s = 90$ and 100 microns. For these values the radiation pattern is very symmetric (Figure 4.7(b) and (c)). If the bars are further shifted, the H-Plane becomes narrower than the E-Plane. An example of this result is shown in Figure 4.7(d). Using larger distances slightly increases the directivity but at the expense of a more asymmetric beam.

Note that these configurations show ideal results with symmetric radiation patterns in both E and H planes. In a real configuration the dipole would be fed by a coplanar stripline, breaking the symmetry of the configuration. This case is studied in section 4.4.

4.3.2 Dipole input impedance

As it was already shown in Chapter 2, the input impedance of a dipole antenna placed on top of a woodpile structure depends very strongly on the position in which it is located. It is expected, therefore, that the modification of the woodpile will have an impact on the input impedance of the dipole.

For each of the configurations previously studied the input impedance of the dipole antenna was computed as a function of its length and the results are presented in Figure 4.8. For the sake of comparison the input impedance of the unperturbed woodpile is also plotted ($s = 0$ curve). As it was expected, the input impedance is largely affected by the modifications in the woodpile. In general, both curves lose the sharp resonance when s increases.

The resonance lengths and the input impedance at resonance of these new configurations are summarised in Table 4.9. The resonance shifts to larger lengths and the input resistance at resonance is higher than it was in the unperturbed case. For displacements larger than 80 microns the input resistance is higher than $100\,\Omega$ whereas for the unperturbed woodpile it was only $11\,\Omega$.

In Chapter 3 it was pointed out that the reason for the bad matching of a dipole placed at the "parallel void-void" configuration was the small value of its input impedance at resonance. By introducing a perturbation in the woodpile the input impedance of the dipole has been also modified, obtaining a configuration with input impedance closer to the characteristic impedance of a coplanar stripline. These results will allow obtaining a matched configuration when feeding the dipole with a coplanar strip line.

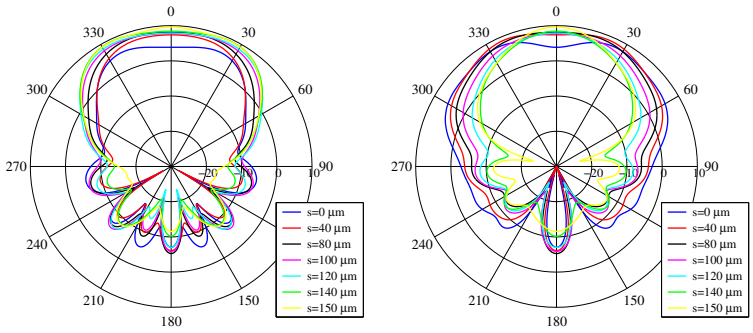

(a) E-Plane (b) H-Plane

Figure 4.6: Radiation pattern of a dipole antenna on top of a modified Si woodpile as a function of the displacement of the bars with respect to the original position. $f = 500\,GHz$.

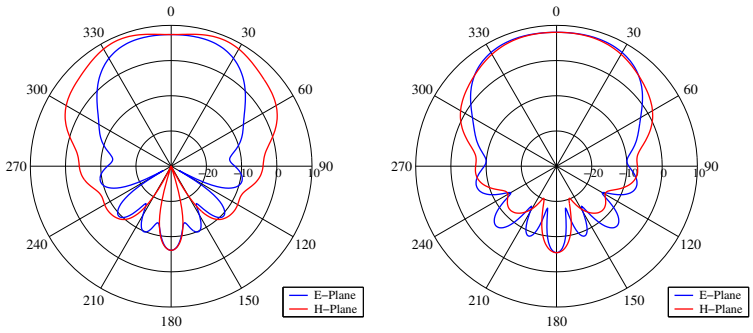

(a) $s = 40$ microns (b) $s = 90$ microns

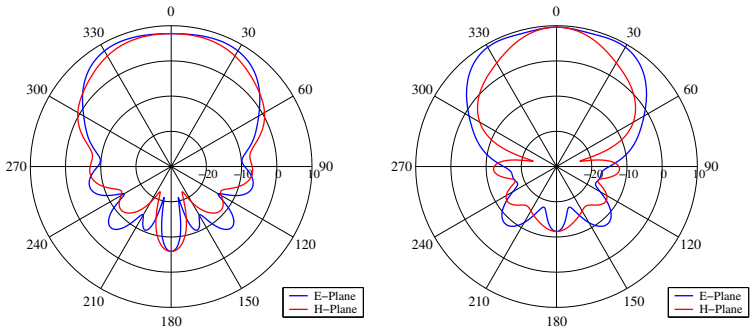

(c) $s = 100$ microns (d) $s = 150$ microns

Figure 4.7: Radiation pattern of a dipole antenna on top of a modified Si woodpile for different displacements of the bars with respect to the original position. $f = 500\,GHz$.

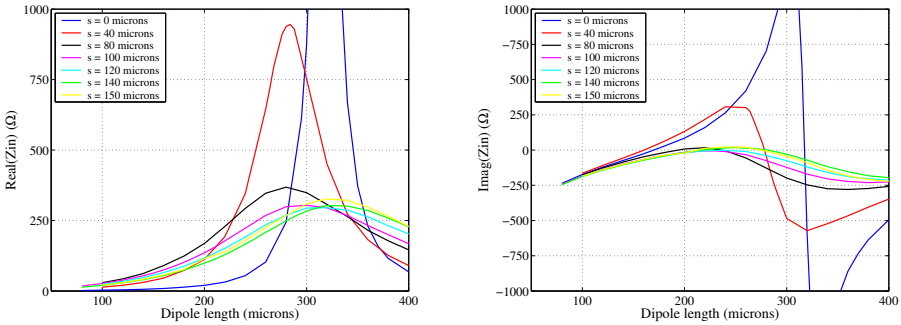

(a) R_i (b) X_i

Figure 4.8: Input impedance ($R_i + jX_i$) of a dipole antenna as a function of the distance with respect to the original position. (a) Real part; (b) Imaginary part. $f = 500\,GHz$.

s (μm)	l_r (μm)	R_i (Ω)
0	170	11
20	164	22
40	161	46
60	167	94
80	194	155
100	220	178
120	240	192
140	217	124
150	213	131

Figure 4.9: Resonant lengths (l_r) and input resistance at resonance (R_i) of a dipole antenna on top of a modified woodpile structure for different values of s. $f = 500\,GHz$.

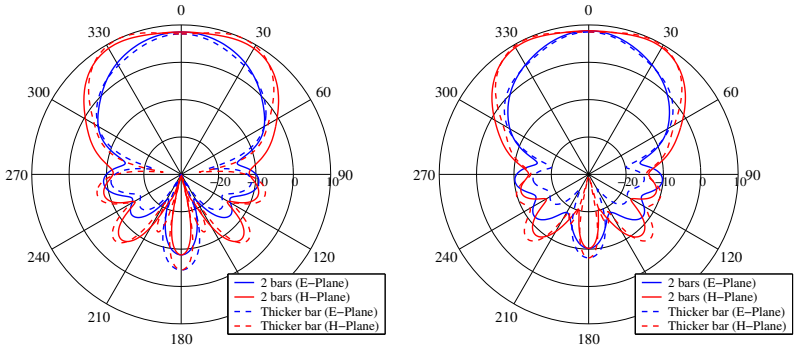

(a) $s = 130$ microns (b) $s = 140$ microns

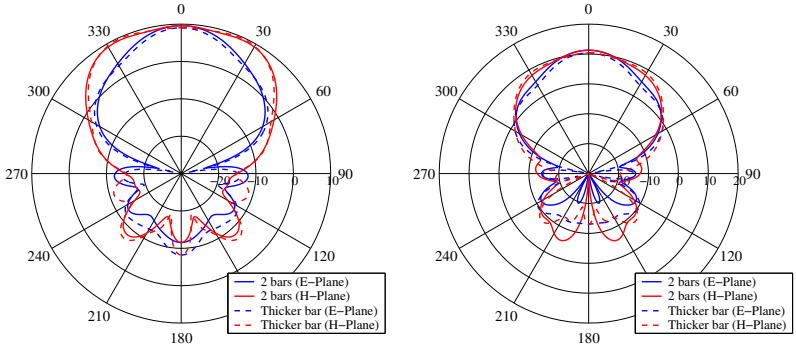

(c) $s = 150$ microns (d) $s = 160$ microns

Figure 4.10: Comparison between the radiation patterns obtained with configurations using thicker bars and 2 bars for different displacements of the bars with respect to the original position. $f = 500\,GHz$.

4.3.3 Comparison between separated bars and thicker bar configurations

As it was mentioned in Section 4.1, if the displacement of the bar is close to 160 microns, the gap between bars can be very narrow. An alternative to this configuration consists of connecting both bars creating a wider bar. The results obtained with this kind of arrangement are compared in Figure 4.10 and 4.11 with those obtained in the previous case.

The radiation patterns are shown in Figure 4.10. For the four selected configurations the results obtained are very similar. With respect to the input impedance of the dipoles, presented in Figure 4.11, the results are also similar

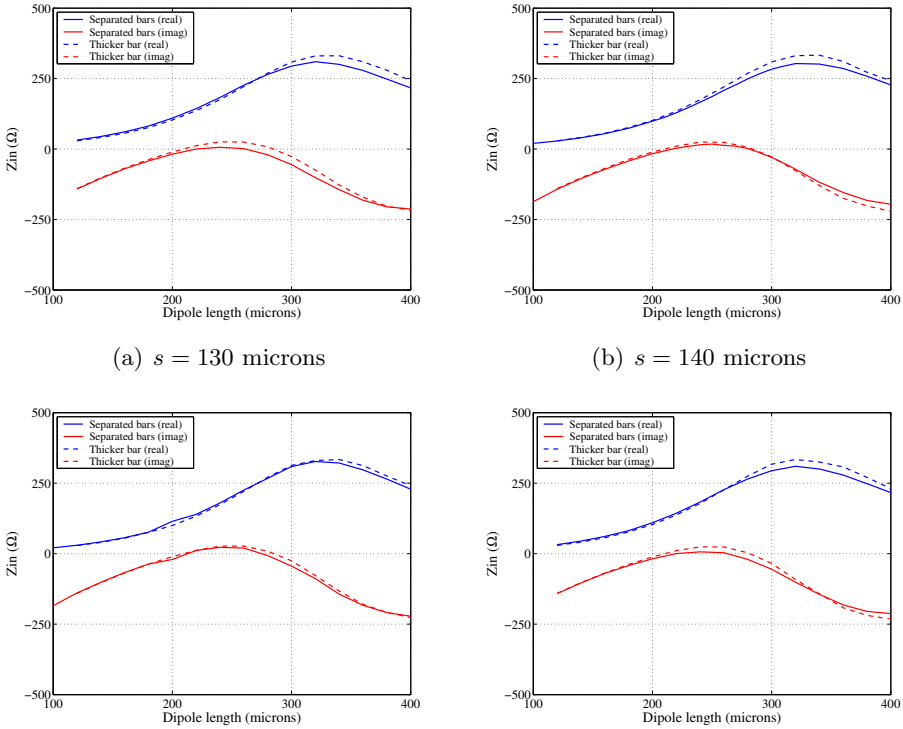

(a) $s = 130$ microns (b) $s = 140$ microns

(c) $s = 150$ microns (d) $s = 160$ microns

Figure 4.11: Comparison between the input impedance obtained with configurations using thicker bars and 2 bars for different displacements of the bars with respect to the original position. $f = 500\,GHz$.

in both cases, the curves being almost identical.

Since both sets of results are very close, the conclusion that can be drawn from the results above is that it is possible to use thicker bars when the gap between bars is too narrow without degrading the performance of the configuration.

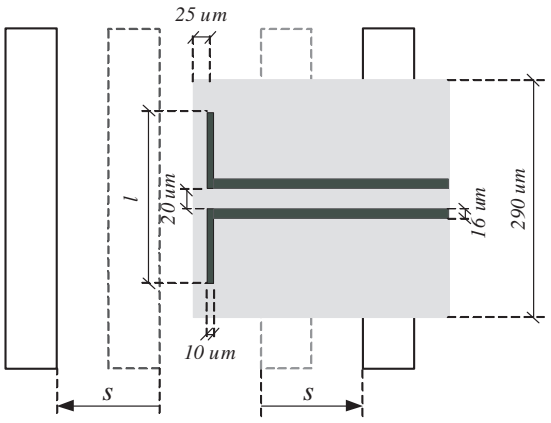

Figure 4.12: Schematic showing the dipole fed by CPS configuration. The grey area corresponds to the quartz substrate and the black one to the dipole and feeding line. The dashed bars are those in the original woodpile whereas the solid ones are those in the modified woodpile.

4.4 Dipole fed by coplanar stripline on modified woodpile

The results shown up to now corresponded to ideal configurations, with symmetric radiation patterns in both E and H planes. In a real configuration the dipole would be fed by a coplanar stripline, breaking the symmetry of the configuration.

The dimensions used in this study are shown in Figure 4.12. The dipole antenna is fed by a coplanar strip line printed on a quartz substrate. Since it was shown that the input impedance of dipole placed on top of this type of modified woodpile is quite large, the width of the coplanar stripline has been chosen as 16 microns, so that its input impedance is 177 Ω. The length of the dipole has been chosen as 270 microns, taking into account the fact that the resonance length of a dipole tends to be larger when fed by a CPS, as it was shown in Chapter 3. In this case, also both the radiation and the matching features of the dipoles have been studied.

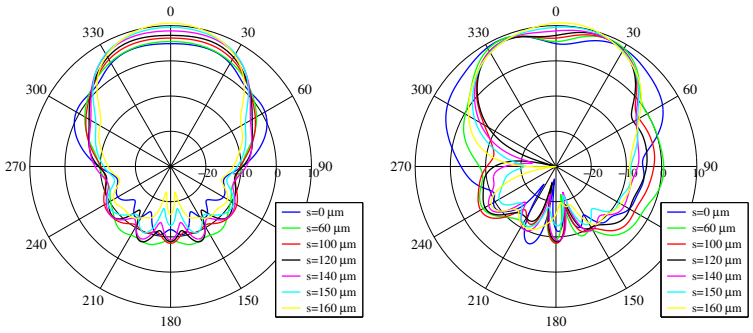

(a) E-Plane (b) H-Plane

Figure 4.13: Radiation pattern of the dipole fed by CPS on top of the modified as a function of the displacement of the bars with respect to their original position. $f = 500\,GHz$.

4.4.1 Radiation pattern

The same study as for the ideal dipole was performed for this new configuration. The s distance was swept and the effect on the radiation pattern can be seen in Figure 4.13. Also in this case the H-Plane gets narrower, and the pattern becomes more symmetric and directive when s increases.

If both planes are plotted together, as in Figure 4.14, it can be seen that the values of s needed for an optimum in terms of symmetry radiation pattern are larger than when an ideal dipole is used. In this case the most symmetric radiation pattern is obtained when the displacement is 150 microns, whereas in the case of the ideal dipole the optimum value was 90 microns. The reason for this fact is the difference between the initial configurations. As it can be seen in Figure 4.15, when the dipole is fed by a CPS, the radiation pattern is different from the radiation pattern of the ideal dipole. For instance, the difference between the boresigth directivity and the maximum directivity is larger than in the ideal case, due to the distortion created by the feeding lines. As a result a larger separation between bars is needed to correct for this.

4.4.2 Matching

The S_{11} values obtained with the previous configurations are shown in Figure 4.16. As it was expected, the configurations are quite well matched, due to the large input impedance. The return loss values obtained at 500 GHz were

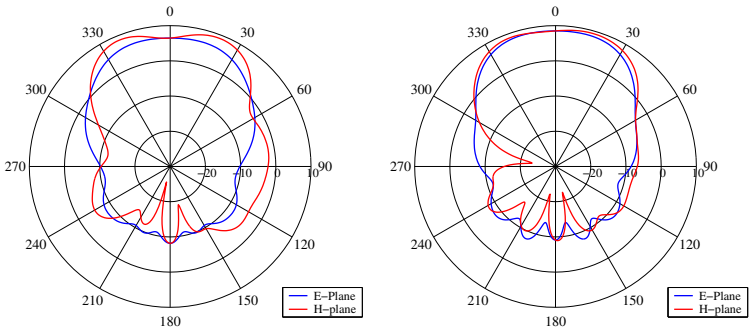

(a) $s = 100$ microns (b) $s = 140$ microns

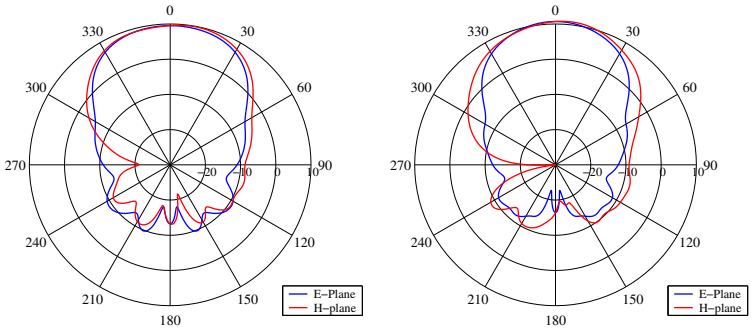

(c) $s = 150$ microns (d) $s = 160$ microns

Figure 4.14: Radiation pattern of the dipole fed by CPS on top of the modified for different displacements of the bars with respect to their original position. $f = 500\,GHz$.

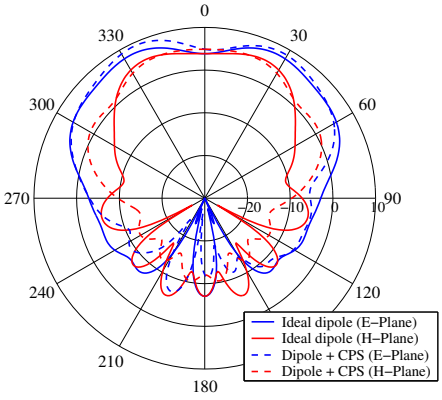

Figure 4.15: Radiation pattern of a dipole and a dipole fed by a CPS on top of the unperturbed woodpile at the "paralell void-void" symmetry position. $f = 500GHz$.

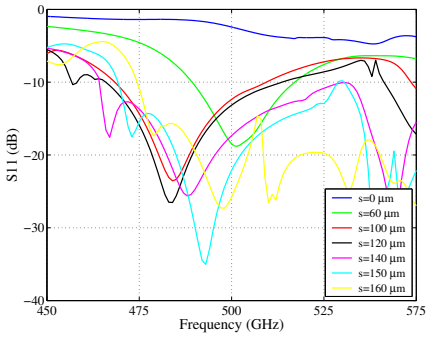

Figure 4.16: Return loss of a dipole fed by CPS on top of the modified woodpile for different displacements of the bars with respect to their original position.

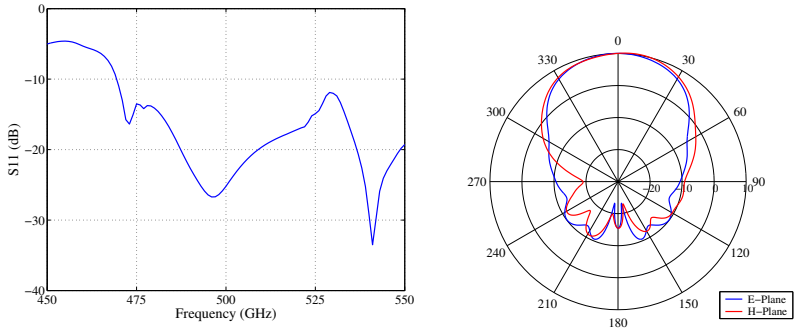

(a) (b)

Figure 4.17: (a) S_{11} and (b) radiation pattern at 500 GHz of the optimum dipole fed by CPS on top of modified woodpile configuration. $s = 150$ microns; $w_f = 12$ microns; $l = 270$ microns.

better than 10 dB in all cases. However, these results can be improved, since the resonance peak is not at the design frequency.

A displacement of the bars of 150 microns was the selected configuration in order to improve the matching, as its radiation pattern was quite symmetric. The return loss was optimised by changing the width of the feeding lines and adjusting the dipole length. The optimum dimensions of these parameters were found to be $w_f = 12$ microns and $l = 270$ microns. The radiation pattern and the S_{11} obtained are presented in Figure 4.17. The return loss achieved is higher than 20 dB at the design frequency and the radiation pattern is quite

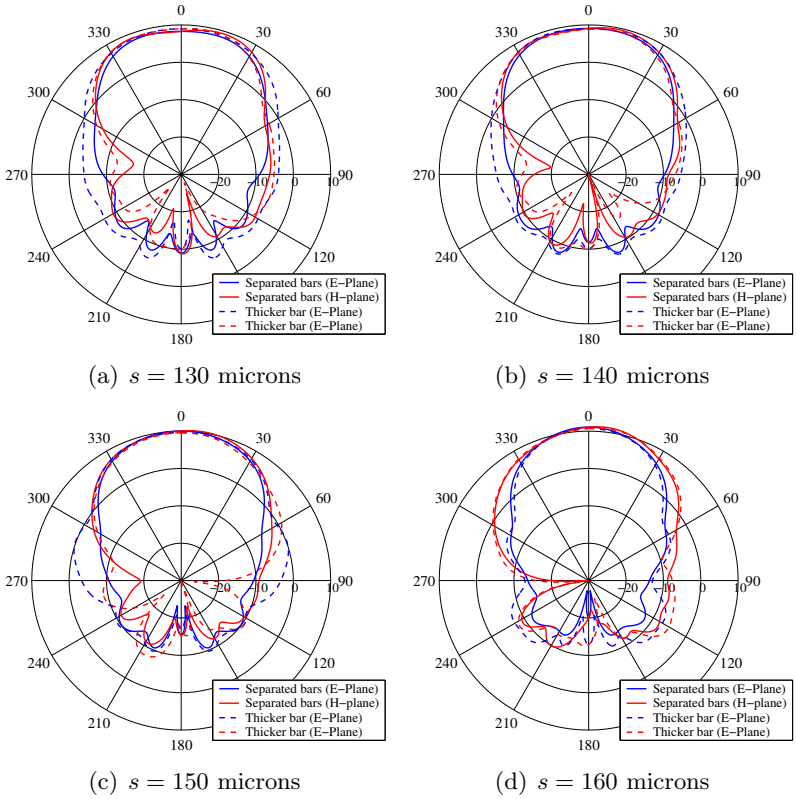

(a) $s = 130$ microns (b) $s = 140$ microns

(c) $s = 150$ microns (d) $s = 160$ microns

Figure 4.18: Comparison of the radiation patterns at 500 GHz obtained with the separated bars bar and the thicker bar configurations.

symmetric.

Comparing this plot with the initial one, shown in Figure 4.14.c) it can be seen that the changes in the feeding line and the length of the dipole have had little effect on the radiation pattern.

4.4.3 Comparison between separated bars and thicker bar configurations

In this case, the differences between the performance of the configuration using two separated bars and the configuration in which the bars are thicker is larger, as it is shown in Figure 4.19 and Figure 4.18.

Regarding the comparison of the radiation patterns, surprisingly, the larger

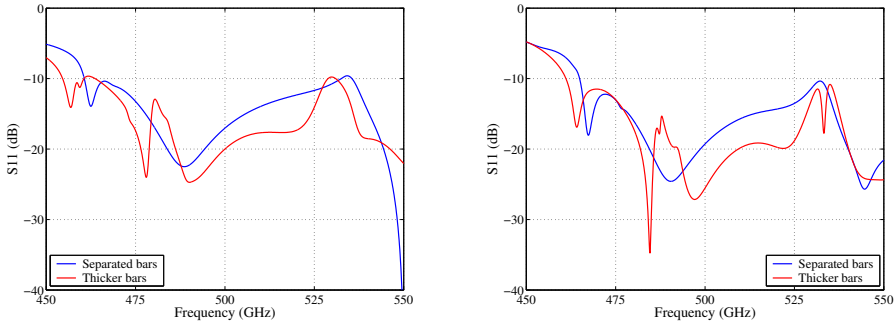

(a) $s = 130$ microns

(b) $s = 140$ microns

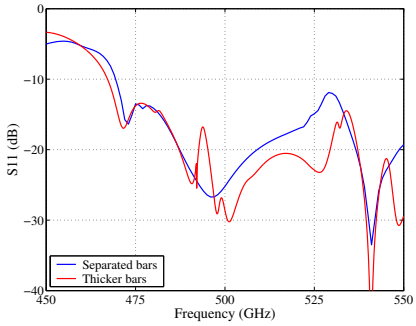

(c) $s = 150$ microns

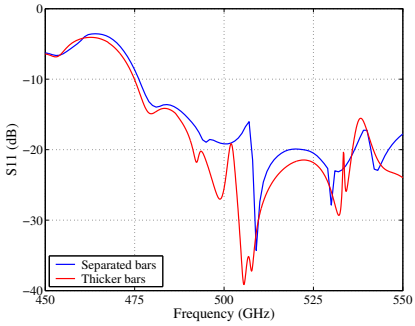

(d) $s = 160$ microns

Figure 4.19: Comparison of the S11 obtained with the separated bars and the thicker bar configurations.

difference corresponds to the E-Plane, whereas the H-Plane remains barely unaffected. The E-plane becomes broader when thicker bars are used. The reason for this broadening of the E-plane is the coupling of some power to the thicker bars.

With respect to the S_{11} of the configurations analysed, they are also very similar. However, when the thicker bars are used, a resonance appear. For certain dimensions this resonance is very close to 500 GHz and modifies the S_{11}. The resonance is caused by the thicker bar, as can be seen in Figure 4.20. In this figure, the electric field distribution is plotted at 490 GHz, which is the frequency of the resonance for this particular configuration, and 500 GHz. At 490 GHz the resonance mode of the dielectric bar is excited, creating the peak in the S_{11}.

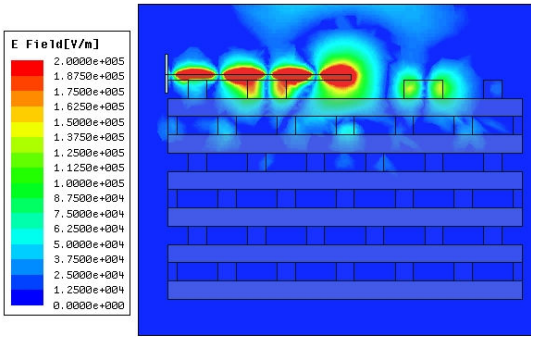

(a) $f = 490$ GHz

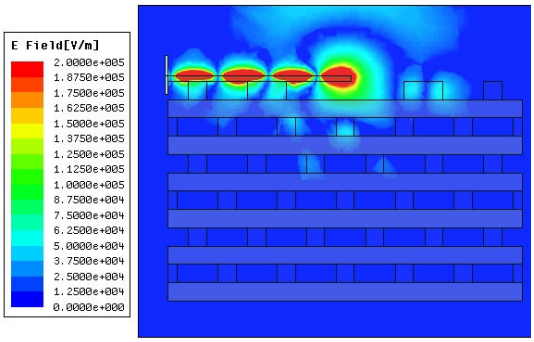

(b) $f = 500$ GHz

Figure 4.20: Electric field distributions for different frequencies. The parameters of the configuration are: $s = 150$ microns (thicker bars), $w_f = 12$ microns, $l = 270$ microns.

4.4.4 Frequency dependence of the radiation pattern

In order to study the frequency dependence of the radiation pattern the configuration with parameters $s = 150$ microns and $w_f = 12$ microns has been selected, since it showed the best compromise between radiation pattern symmetry and matching. The S_{11} of this configuration and its radiation pattern at 500 GHz have already been presented in Figure 4.17. At this frequency the radiation pattern is quite symmetric and the S_{11} is -29dB.

Since the optimisation of the configuration was based on the adjustment

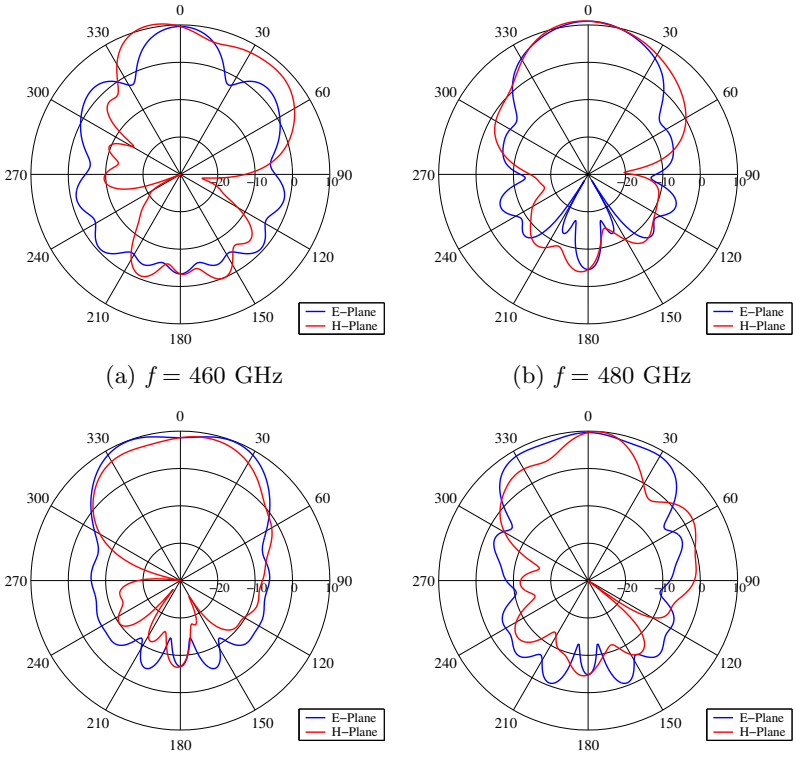

(a) $f = 460$ GHz (b) $f = 480$ GHz

(c) $f = 520$ GHz (d) $f = 540$ GHz

Figure 4.21: Radiation pattern of the selected configuration of dipole on top of modified woodpile at different frequencies. $s = 150$ microns and $w_f = 12$ microns.

of the interference pattern the bandwidth of the configuration will be reduced with respect to the case of an unperturbed woodpile. The radiation pattern obtained at different frequencies is shown in Figure 4.21. At 480 GHz and 520 GHz the radiation patterns are still quite symmetric. The boresight directivity is slightly larger at 480 GHz, similar result to what was obtained in the unperturbed woodpile. For frequencies further apart, such as 460 GHz and 540 GHz the radiation patterns are much degraded. In both cases the symmetry of the pattern has been lost and the back radiation has increased.

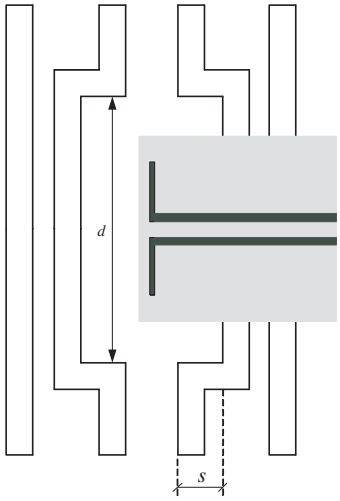

Figure 4.22: Dipole fed by CPS on 2D cavity modified woodpile configuration, top view. The grey area corresponds to the quartz substrate and the black one to the dipole.

4.5 2D cavity configuration

As it was previously mentioned, in the configurations considered above a complete bar of the woodpile was shifted. However, since the antenna is placed at very specific location it is enough if instead of modifying the whole bar, only the portion of bar closer to the dipole is reshaped, as it is shown in Figure 4.22. In this case, two parameters can be modified in order to optimize the configuration, d and s. It is expected that large values of d will lead to very similar results to those obtained in the previous configurations, where the whole bar was modified.

In this study only the CPS fed dipole has been considered. The optimum configuration in terms of matching (s = 150 microns; w_f =12 microns; l=270 microns) has been chosen as starting point. The d parameter will be swept and its effect on the return loss and on the radiation pattern of the configurations will be studied. Note that the purpose of this section is not to obtain a fully optimised design, but just to shown the changes in the performance of a certain configuration when the bars are modified locally.

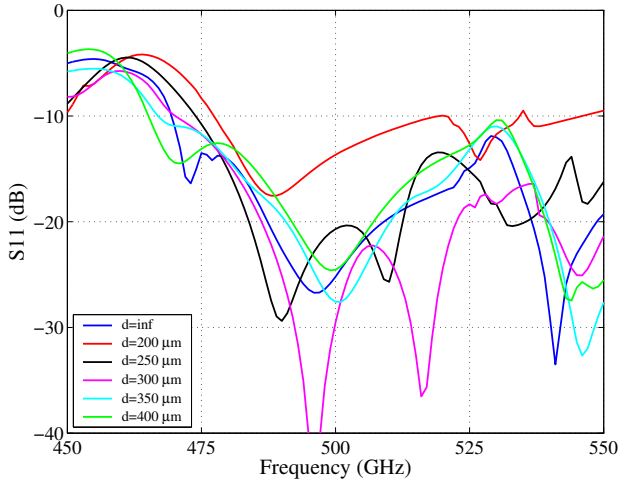

Figure 4.23: Return loss of a dipole antenna fed by a CPS on a 2D cavity modified woodpile configuration as a function of the d parameter. $s = 150$ microns; $w_f = 12$ microns; $l = 270$ microns.

4.5.1 Matching

The changes in the matching of the dipole as a function of the distance d are shown in Figure 4.23. As it was expected, small values of d lead to a degradation of the matching, due to the similitude between this configuration and the original unperturbed woodpile. On the other hand, if d is large enough the results are quite similar to those obtained when the whole bar is displaced. Values in between these two limit cases give the chance of getting even a better and broader band matching than in the original configuration, the reason for this being that the cavity that is created is better excited.

4.5.2 Radiation pattern

The dependence of the radiation pattern on the d parameter is presented in Figure 4.24. As it was expected, the E-Plane is more affected by the modifications carried out, especially for small values of d. However, a good symmetry can be still maintained (see Figure 4.24).

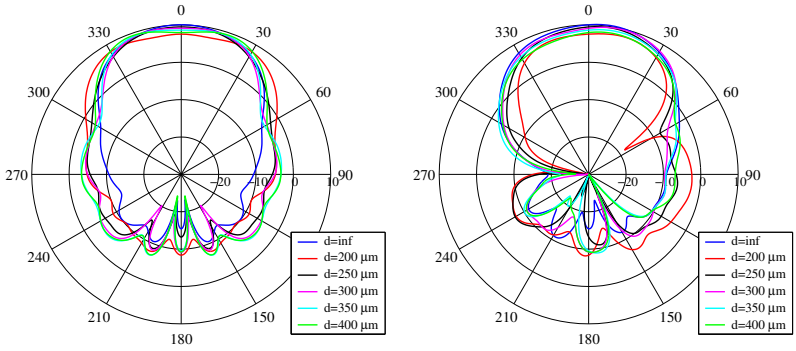

(a) E-Plane (b) H-Plane

Figure 4.24: Radiation pattern of a dipole antenna fed by a CPS on a 2D cavity modified woodpile configuration as a function of the d parameter. $s = 150$ microns; $w_f = 12$ microns; $l = 270$ microns.

4.5.3 Frequency dependence of the radiation pattern

From the previous results, the configuration in which the value of d was 350 microns has been selected in order to study the effect of the frequency on the radiation pattern. The reason to choose this configuration was the symmetric radiation pattern and the broad frequency band in which the matching was better than -20 dB. The radiation pattern corresponding to this configuration is presented in Figure 4.25.

With respect to the frequency dependence of the radiation pattern, the behaviour is the same as in the previous configuration, although the bandwidth in which the radiation pattern remains similar to that at 500 GHz is smaller than in the previous case, see Figure 4.26. For instance, the pattern at 520 GHz has lost most of its symmetry, whereas in the previous case it was still quite symmetric.

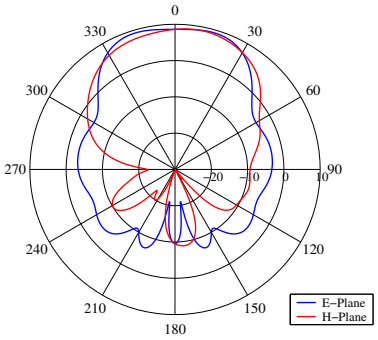

Figure 4.25: Radiation pattern at 500 GHz of the selected configuration of dipole antenna fed by a CPS on a 2D cavity modified woodpile. $s = 150$ microns; $d = 350$ microns.

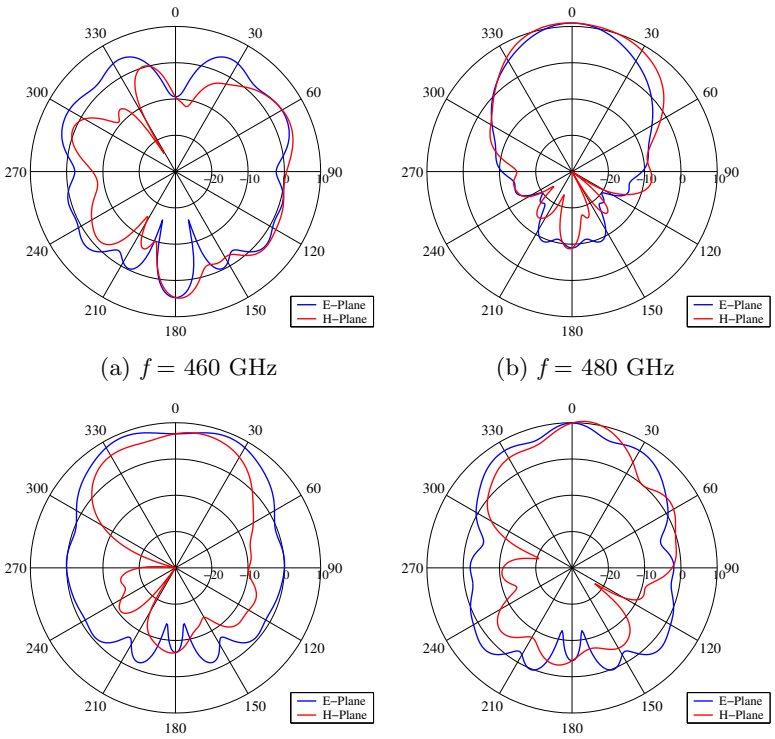

(a) $f = 460$ GHz (b) $f = 480$ GHz

(c) $f = 520$ GHz (d) $f = 540$ GHz

Figure 4.26: Radiation pattern vs. frequency for the selected configuration of dipole antenna fed by a CPS on a 2D cavity modified woodpile. $s = 150$ microns; $d = 350$ microns.

Chapter 5

Direct detector using EBG technology

5.1 Introduction

In the previous chapters the performance in terms on matching and radiation pattern of different configurations based on the combination of dipole antennas and EBG structures have been studied. In order to use them as radiating elements of a detector configuration the best combination of EBG and radiating configuration had to be selected.

With respect to the EBG structure, the silicon woodpile structure was chosen. Although the other EBG structures studied provided wider bandgaps, they are based on ceramic materials, which are not as easy to process. Conversely, the manufacture techniques used with silicon are well known and accurate enough to meet the specified requirements [Azc03; Azc04; Gon02]. Moreover, the increase in dielectric constant does not reduce the size of the dipoles as much as it would be a-priori expected. Therefore, the overall size of the configuration will be limited by the antenna size, which makes it difficult to achieve more compact systems.

Regarding the radiating configuration, the "perpendicular solid-solid" symmetry position was selected, since as it was discussed in Chapter 3, it provides the best compromise between matching and radiation features. Based on this radiating configuration a receptor working at 500 GHz, which aims at achieving the best sensitivity, is designed in this chapter using a Schottky diode as detecting element.

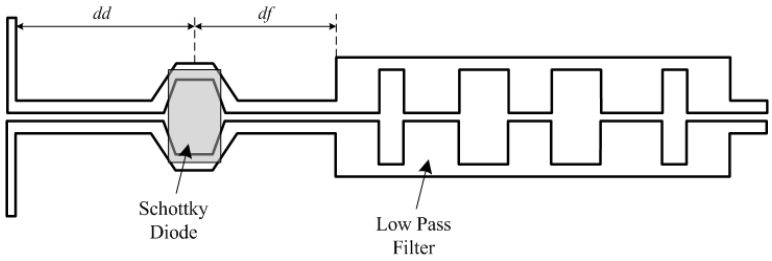

Figure 5.1: Detector configuration and design parameters.

5.2 Configuration

The proposed detector configuration is shown in Figure 5.1. It consists of a dipole antenna placed on top of a woodpile structure, a Schottky diode and a low-pass filter connected to the dipole antenna. The metallic lines are printed onto a quartz substrate. A signal proportional to the power levels detected by the antenna is obtained at the output of the RF filter. The design parameters, which will be used to optimize the detected power level are the shape of the lines around the diode and the distances from the diode to the dipole and to the filter, *dd* and *df* respectively.

The elements that constitute the detector are explained in detail in the following sections.

5.2.1 Antenna configuration

The antenna configuration is based on a dipole printed on a quartz substrate and fed by a coplanar stripline. The dipole is placed on top of the woodpile at the "perpendicular solid-solid" symmetry position. Since this configuration has been extensively studied in chapter 2 and 3, here only the predicted S_{11} and the radiation pattern of the configuration are presented, see Figure 5.2.

Note that in these results only the antenna and the feeding lines are included. However, as it will be explained later on, the diode and the filter have a large impact on the radiation performance of the configuration. Therefore, in order to accurately predict the radiating performance of the configuration, both the diode and the filter will be included in the analysis.

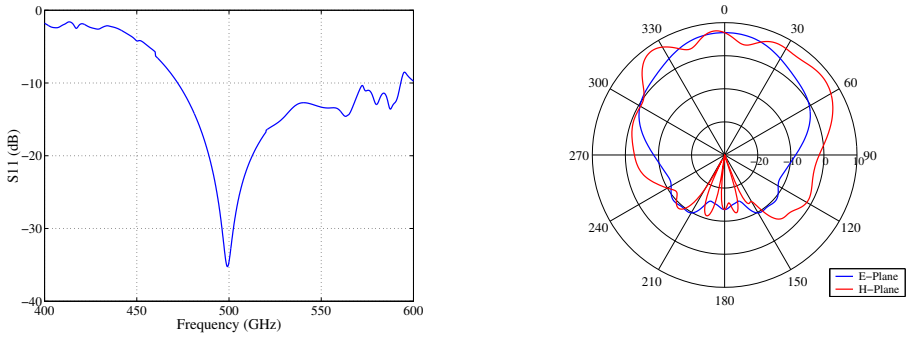

(a) (b)

Figure 5.2: (a) S_{11} parameter of the optimised dipole fed by CPS line configuration. (b) Radiation pattern at $f = 500$ GHz.

5.2.2 Schottky diode

The selected Schottky diode is the Flip-Chip United Monolithic Semiconductors (UMS) GaAs dual diode BDES105a, see Appendix D for the details (datasheet of the diode). The diodes come in pairs and dicing is performed to separate them and to decrease their size, in order to improve their high frequency operation. After dicing, the diodes are approximately 140 microns long x 60 microns wide x 30 microns thick. In Figure 5.3 the size of the diodes before and after dicing can be compared. Some more detailed pictures of the diode are shown in Figure 5.4.

To characterise the diode, measurements were performed on a sample, giving:

- Series resistance $R_s = 8.6\,\Omega$
- Ideality factor $n = 1.283$
- Saturation current $I_s = 1.031 \times 10^{-13}\,A$.

These values are slightly different from those provided in the datasheet which are $R_s = 4.4\,\Omega$, $n = 1.2$ and $I_s = 3.5 \times 10^{-14}\,A$. The 0 bias junction capacitance C_{j0} could not be measured. Hence, the value used for Harmonic Balance simulations is the one given in the data sheet, i.e. $C_{j0} = 9.5\,fF$.

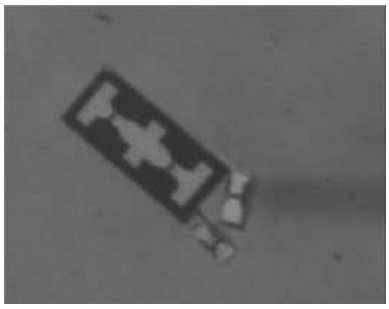

Figure 5.3: Photograph of a diode chip and the two resulting diodes after dicing.

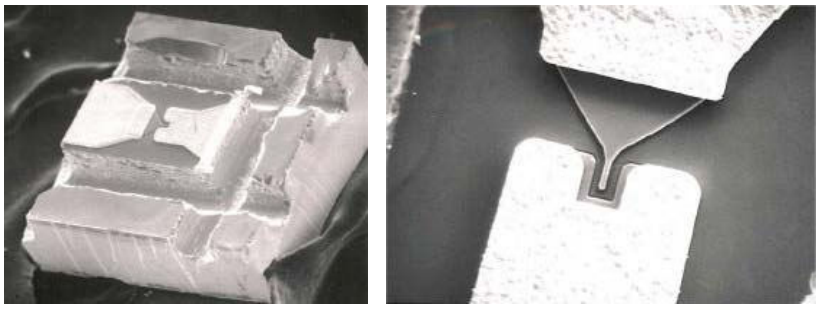

(a) (b)

Figure 5.4: Photographs of the UMS BDES105a Schottky diode. (a) Diode while being diced. (b) Close up of the diode.

5.2.3 Low-pass filter

The low pass filter does not allow the RF signal to pass, whilst it lets the DC output go through. Due to the blocking of the RF signal, it can be used as a tuneable short-circuit, which makes it possible to adjust the diode embedding impedance and the power coupling to the diode by modifying the distance from the diode to the filter, *df* in Figure 5.1.

The filter is composed of cascading alternated high and low impedance sections of coplanar stripline. An important parameter of the filter is its total width, since it can perturb the radiation pattern of the dipole. Therefore, care has to taken to design a filter as narrow as possible.

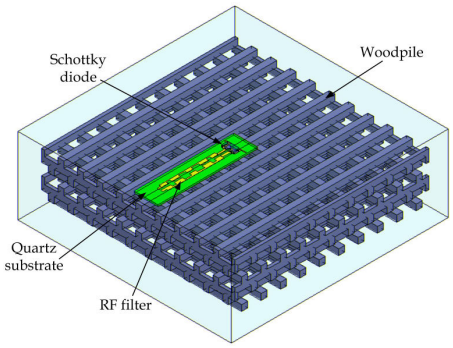

(a) Full HFSS model

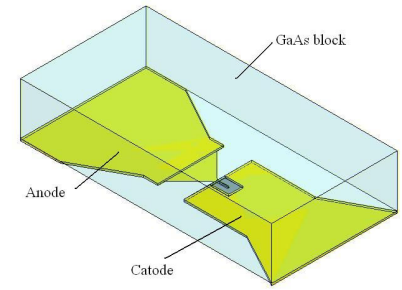

(b) Diode model

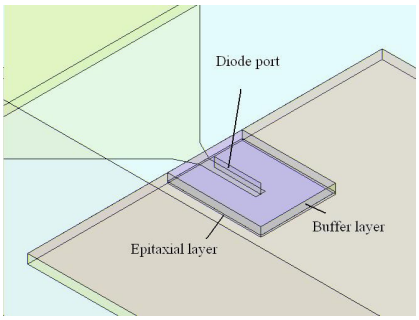

(c) Diode model

Figure 5.5: HFSS model used to compute the radiation pattern and the diode embedding impedance.

5.3 Modelling

5.3.1 HFSS model

This section describes the HFSS model used in the simulations of the performance of the detector configuration. The model proposed is shown in Figure 5.5. The excitation corresponds to a lumped gap source placed at the diode mesa. As it was already mentioned, in this case, since the diode is close to the dipole antenna the interaction between diode and dipole can not be neglected and the diode must therefore be included. Also the filter must be taken into account in order to compute its influence on both the radiation pattern and

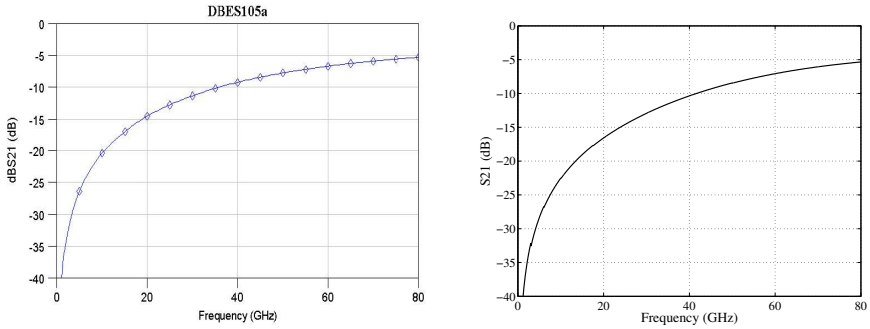

(a) (b)

Figure 5.6: Transmission through the diode. (a) Curve taken from the datasheet. (b)HFSS model of the diode.

the embedding impedance of the diode. Finally the woodpile must be large enough so as to accurate model the behaviour of a real structure. In our case the analysed model consisted of $11 \times 11 \times 2$ woodpile periods since this was the largest woodpile structure that could be analysed with the available version of Ansoft HFSS.

With respect to the diode model, it aims at describing precisely the contribution of the surrounding elements to the impedance seen by the diode, i.e. the metal-semiconductor junction. The dimensions and doping used for this model have been approximated using information in the data sheet and SEM pictures. The resulting model is presented in Figure 5.5 (b and c). It is composed of:

- highly doped ($\epsilon_r = 12.9$) GaAs block
- buffer layer ($\epsilon_r = 18$)
- lightly doped ($\epsilon_r = 14$) GaAs epitaxial layer.

As shown in Figure 5.5(c), a HFSS lumped gap source port is placed from the gold finger to the GaAs block, in order to compute the diode embedding impedance. The dimensions of the model are $140 \times 60 \times 30$ microns.

To check the accuracy of the model, a curve in the data sheet of the diode corresponding to measurements of transmission when placed in a microstrip line gap was reproduced. The results are presented in Figure 5.6. Good agreement is found between both curves.

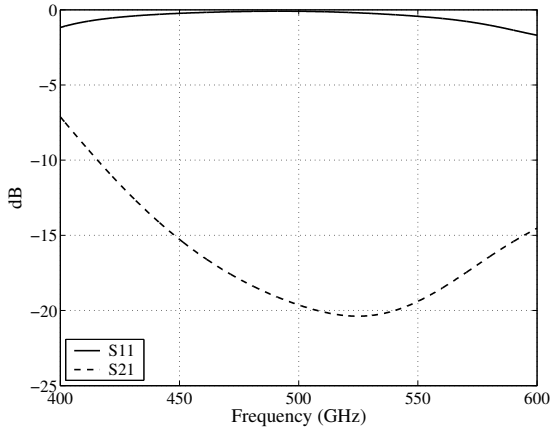

Figure 5.7: Predicted low pass filter response.

5.3.2 Low pass filter

As it was mentioned the design of this filter is based on alternated sections of low-high impedance coplanar striplines. The number of sections used is 5, since we were aiming at compactness. In order to reduce the interaction of the radiation with the low pass filter the filter should be as narrow as possible. However, this reduces the contrast between the impedances, making the filter slightly longer.

The predicted response of the filter is shown in Figure 5.7. The rejection obtained at 500 GHz is 19 dB.

5.3.3 Effect of the design parameters on the diode embedding impedance and the power coupling to the diode

In this section the effect on the diode embedding impedance and the coupling of power to the diode of the design parameters, i.e. diode-filter distance (df), the diode-dipole distance (dd) and the shape of the lines around the diode (see Figure 5.1), is studied.

Regarding the shape of the lines, a non symmetric configuration (see Figure 5.8) provides a larger range of tuning. However, this would introduce some asymmetry in the E-plane of the radiation pattern. Thus, only symmetric designs were considered.

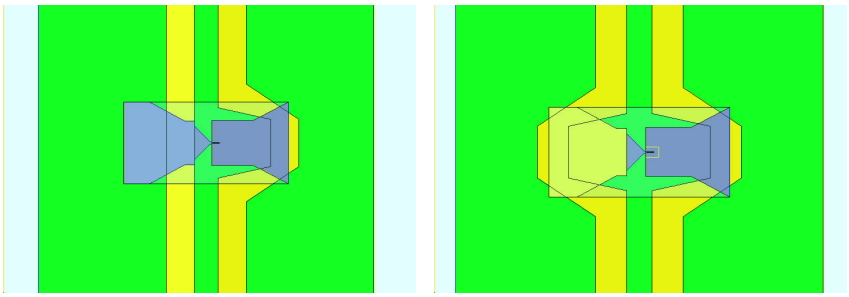

(a) Asymmetric configuration (b) Symmetric configuration

Figure 5.8: Schematic showing symmetric and asymmetric configurations of the lines surrounding the diode.

Diode embedding impedance and coupling to the diode

An Harmonic Balance analysis of the proposed detecting configuration was carried out [Lai03] in order to find the optimum embedding impedance for the selected UMS Schottky diode. This value was found to be $14 + j15\,\Omega$.

Initially, in order to predict the diode embedding impedance, the HFSS model shown in Figure 5.9 was used. In this model the dipole is assumed to be matched and is substituted by a port. Therefore the interaction between diode and dipole is not being considered. However, this simplified model will allow us to get an insight into the role of the filter in the process of coupling of power to the diode.

The distance between the diode and the filter, *df*, plays a very important role in the matching process, since it acts as a tuneable backshort, changing the diode embedding impedance the way it is shown in Figure 5.10. Moreover, if the coupling from the dipole port to the diode is examined, it is found that it also depends on the separation between diode and filter as it is presented in Figure 5.11. The coupling is a maximum for a distance of 160 microns. The minimum of the curve takes place at a distance of 190 microns, which corresponds to the diode being at the null of the standing wave pattern generated by the filter. The electric field distribution in both cases is shown in Figure 5.12.

Unfortunately, the optimum values in terms of embedding impedance and coupling do not correspond to the same distance to the dipole. The value of *df* that creates an embedding impedance closest to the optimum value according to the Harmonic Balance analysis, $df = 170$ microns (red circle

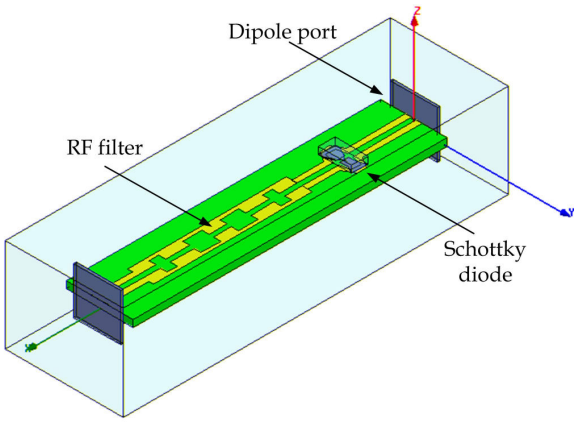

Figure 5.9: HFSS model used to compute the coupling to the diode and the diode embedding impedance.

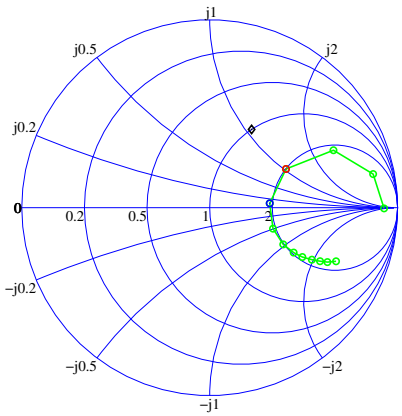

Figure 5.10: Predicted diode embedding impedance at 500 GHz as a function of the diode-filter distance (df). The initial point is df=90 microns and the step between points is 10 microns. Increasing df corresponds to clockwise displacement in the curve. The blue and red circles correspond to df=160 and df=170 microns respectively. The black diamond shows the optimum embedding impedance value according to Harmonic Balance analysis. Note that the reference impedance has been taken as 14 Ω for the sake of improved visibility.

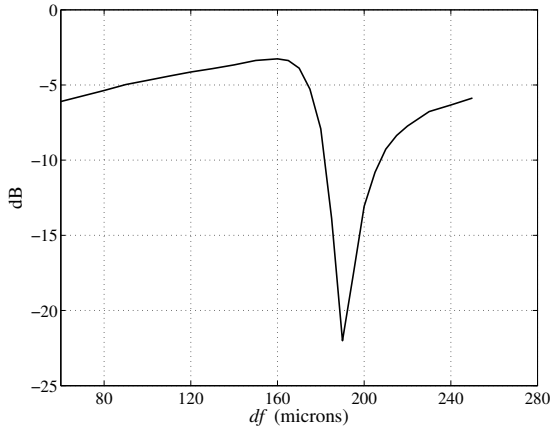

Figure 5.11: Predicted coupling to the diode port at 500 GHz as a function of the diode-filter distance, df.

in Figure 5.10), does not correspond to the maximum power coupling to the diode port, which takes place for $df = 160$ microns. The two values are quite close, but for values of df larger than 160 the coupling curve decreases very sharply and the embedding impedance tends to move away from the optimum value also very rapidly. Any deviation from the optimum values due to the manufacturing tolerances can lead to very different embedding impedances and worse performance of the detecting configuration.

Distance from the diode to the dipole

In the previous section, the dipole was assumed to be perfectly matched and was substituted by a port, so that the coupling from this port to the diode could be studied. However, as it will be shown, the distance between the diode and the dipole makes the embedding impedance of the diode change.

The curves in Figure 5.13 correspond to different distances between diode and dipole, dd. For each value of dd the separation between diode and filter, df, has been swept. The results obtained are different from those obtained substituting the dipole by a port, given by the green line, and depend very strongly on the diode to dipole distance. It is foreseen that if dd is very large the results should tend to this curve.

The curve that is closest to the optimum embedding impedance according

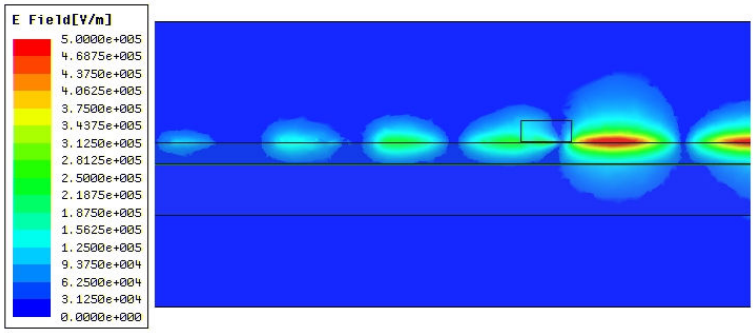

(a) df = 160 microns

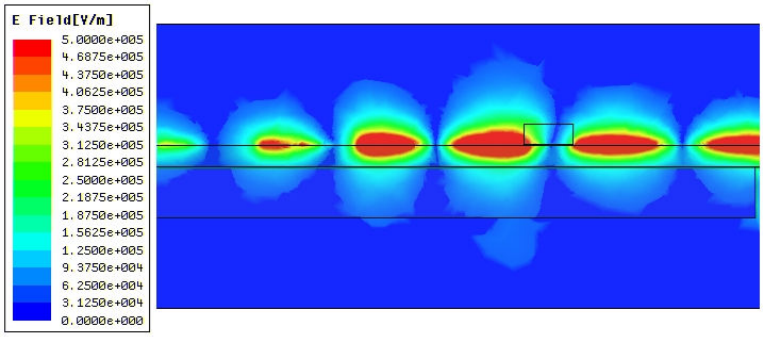

(b) df = 190 microns

Figure 5.12: Predicted electric field distribution for the maximum (a) and the minimum (b) of the coupling curve. 500 GHz.

to the Harmonic Balance analysis corresponds to a diode-dipole distance of 100 microns. The curve corresponding to 50 microns distance between diode and dipole is also close to the optimum embedding impedance. However, as it was already mentioned, in this case the embedding impedance changes very fast, which makes this configuration very sensitive to manufacturing errors.

5.3.4 Effect of the design parameters on the radiation pattern

Once the effect of the design parameters on the diode embedding impedance has been studied, in this section their effect on the radiation pattern of the configuration will be assessed. The dipole dimensions are those corresponding to the optimum configuration found in the previous chapters: the dipole is 235

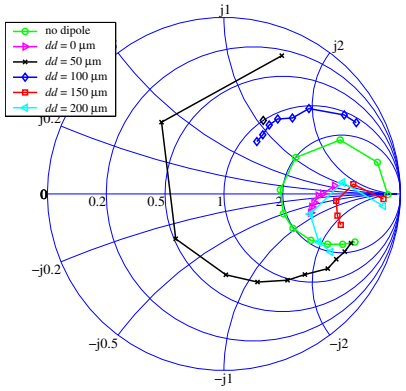

dd	*df*
0	80, 90, 100, 110, 120, 130, 140,150, 160, 170, 180, 190, 200
50	60, 80, 100, 120, 140, 150, 160, 165, 170, 175, 180
100	130, 135, 140, 145, 150, 160, 175, 180
150	120, 140, 160, 180, 200
200	120, 140, 160, 180, 200

Figure 5.13: Predicted diode embedding impedance at 500 GHz. In each curve the distance diode-dipole is fixed whereas the distance diode-filter is swept. The black diamond shows the optimum embedding impedance value according to Harmonic Balance analysis. The distances (in microns) used in each curve are shown in the table. Note that the reference impedance has been taken as 14 Ω for the sake of improved visibility.

microns long and 10 microns wide and the thickness of the quartz substrate is 20 microns. Finally, as it was already mentioned, in all the simulations the woodpile consists of $10 \times 10 \times 2$ periods.

Distance from the diode to the dipole

The first study consisted of varying the distance between the diode and the dipole, *dd*, while keeping constant the distance between the filter and the diode, *df*, to a value of 160 microns. This distance was chosen since the power coupled to the diode is a maximum in this case, as it was shown in section 5.3.3.

Figure 5.14 shows a very strong dependence of the radiation pattern on the separation between the diode and the dipole. For the different configurations the H-Plane pattern presents nulls at different angles, due to the interference between the radiation of the dipole and the power scattered at the diode. The E-Plane keeps the same shape, although the directivity values at boresight change due to the different interference patterns. It should be noted that the configuration in which $dd = 100$ microns exhibits an E-Plane quite different to the other ones due to the null at boresight.

These results agree with the fact that the diode embedding impedance also

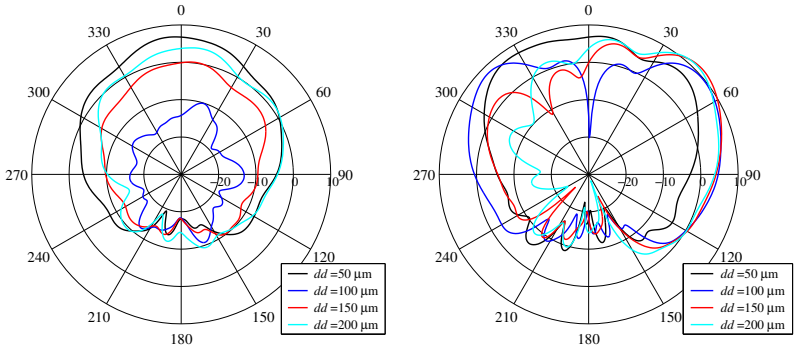

(a) E-Plane (b) H-Plane

Figure 5.14: Predicted radiation pattern at 500 GHz of a dipole antenna on top of a woodpile structure when the distance between the diode and the dipole are changed. $df = 160\,\mu m$.

changed with the diode to dipole distance, as it was shown in the previous section. Both results confirm that the interaction between both elements can not be neglected. Regarding the radiation patterns, it can be concluded that since the radiation pattern depends on the scattering on the diode, it is necessary that the distance between dipole and diode be as short as possible in order that they are in phase. However, since the diode requires some space to be soldered onto the circuit the minimum value of this parameter that will be considered is 50 microns.

Distance between diode and filter

In this case the distance from dipole to diode, dd, was kept fixed, whereas the separation between diode and filter, df, was modified. Results obtained for $dd = 50$ microns and $dd = 100$ microns are presented in Figure 5.15 and Figure 5.16 respectively. In both cases the radiation pattern keeps the same shape, with minor changes. In the configuration in which $dd = 100$ microns the null close to boresight is present irrespective of the configuration making the E-plane change. These results confirm that the radiation pattern is mainly determined by the separation between the diode and the dipole and the effect of the distance from the diode to the filter is much smaller.

In both cases, the pattern corresponding to 180 microns is quite different from the others. The reason for this fact is that for this distance the diode is

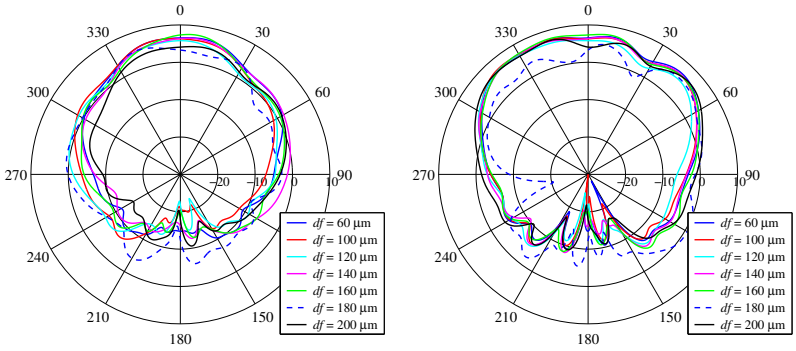

(a) E-Plane (b) H-Plane

Figure 5.15: Predicted radiation pattern at 500 GHz of a dipole antenna on top of a woodpile structure when the distance between the diode and the filter is changed. $dd = 50\,\mu m$.

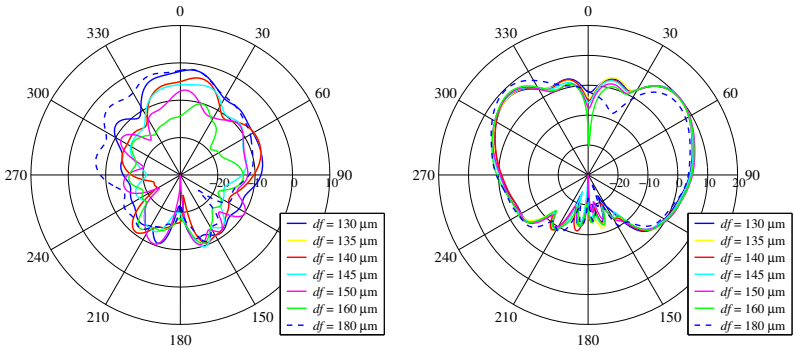

(a) E-Plane (b) H-Plane

Figure 5.16: Predicted radiation pattern at 500 GHz of a dipole antenna on top of a woodpile structure when the distance between the diode and the filter is changed. $dd = 100\,\mu m$.

very close to be placed at one null of the standing wave pattern generated by the filter and is effectively short-circuited. As it was shown in section 5.3.3 the coupling to the diode was a minimum for this distance.

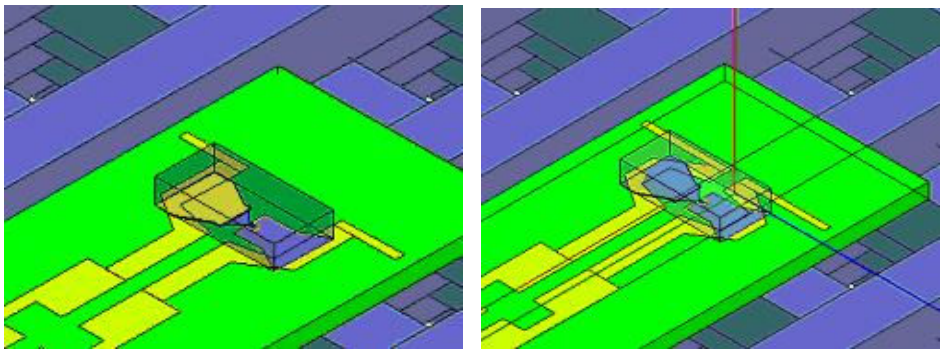

(a) (b)

Figure 5.17: Schematic showing (a) the new configuration proposed and (b) the old one.

5.3.5 Optimum configurations

Since with the proposed configuration of the lines it was not possible to achieve at the same time a good radiation pattern and embedding impedance close to the optimum according to the Harmonic Balance analysis, the lines around the diode have been modified (see Figure 5.17). Using this modified configuration, the range of embedding impedances shown in Figure 5.18 has been obtained. For 50 microns diode-dipole distance the diode embedding impedance is quite close to the optimum value when the diode-filter distance is 180 and 185 microns.

With respect to the radiation patterns obtained with these configurations at 500 GHz, shown in Figure 5.19, they are similar to those obtained with the previous one, due to the fact that same value of *df* is used in both cases. The radiation pattern for 185 microns distance is quite degraded due to the standing wave created by the filter. However, for 180 microns it is still acceptable.

Since with this configuration both a good radiation pattern and a good matched diode can be achieved, it was selected in order to build the detector configuration. Based on the previous results, four configurations have been selected. In all of them the distance from the diode to the dipole is 50 microns since as it was previously shown, for this distance the radiation pattern was not affected by the interaction with the diode, while having at the same time enough room to solder the diodes. Their embedding impedances and radiation patterns at 500 GHz are presented in Figure 5.21 and Figure 5.22 respectively.

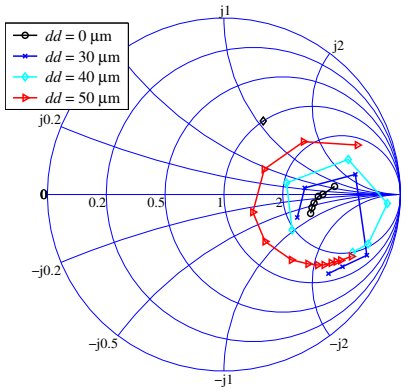

dd	*df*
0	120, 140, 150, 160, 170, 180
30	170, 180, 190, 210, 230, 250
40	170, 180, 190, 200, 220, 240
50	70, 100, ,120, 130, 140, 150, 160, 170, 175, 180, 185, 190

Figure 5.18: Predicted diode embedding impedance at 500 GHz for the modified configuration. In each curve the diode-dipole distance is fixed whereas the distance diode-filter is swept. The black diamond shows the optimum embedding impedance value. The distances (in microns) used in each curve are shown in the table. Note that the reference impedance has been taken as 14 Ω for the sake of improved visibility.

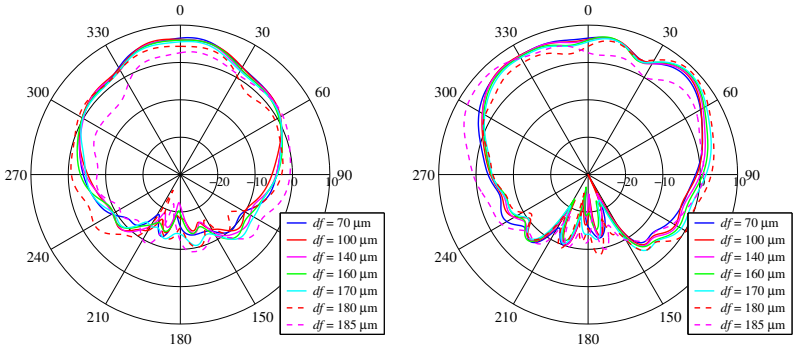

(a) E-Plane (b) H-Plane

Figure 5.19: Predicted radiation patterns at 500 GHz obtained with the new configuration. dd= 50 microns.

The dimensions of the 4 configurations are presented in Figure 5.20.

The first configuration, C1, is based on the original arrangement, in which the lines enclose the diode. The distance between the diode and the filter is 150 microns in this configuration. This distance is slightly shorter than the best value which corresponds to 160 microns, in order to guarantee a good performance in case the dimensions of the manufactured circuit are larger than

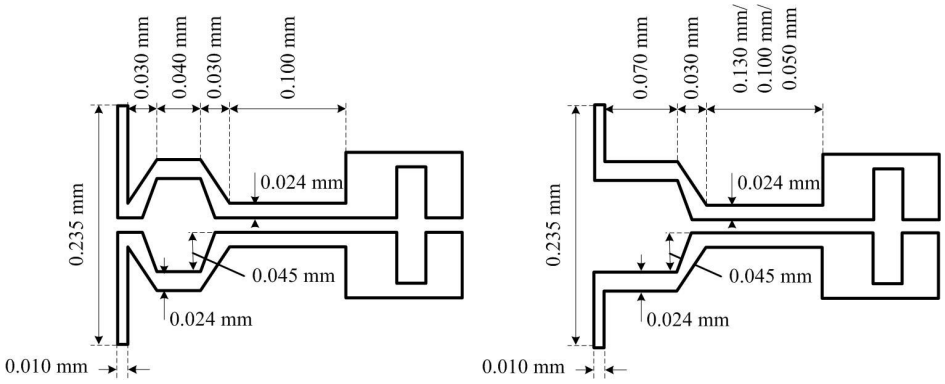

(a) C1 (b) C2, C3, C4

Figure 5.20: Dimensions of the selected configurations.

the design values. The radiation pattern corresponding to this configuration is quite symmetric, as can be seen in Figure 5.22(a).

C2, C3 and C4 are based on the new configuration, in which the lines have been opened in the side closer to the dipole. As it was pointed out, with this configuration it is possible to be closer to the optimum embedding impedance while having a good radiation pattern. The distance between the diode and the filter is 180, 150 and 100 for C2, C3 and C4 respectively.

The configuration labelled as C2 presents a diode embedding impedance which is close to the optimum one according to the Harmonic Balance analysis, while having at the same time a good radiation pattern, which is presented in Figure 5.22(b). C3 has a good coupling to the diode according to HFSS, similar to C1. Finally, C4 is close to C2 in terms of coupling to the diode but its embedding impedance is further from the optimum embedding impedance than the other configurations. Its predicted radiation pattern is similar to the radiation pattern of C3, as it is shown in Figure 5.22(c and d).

5.4 Fabrication

The fabrication of the detector configurations was carried out at the Rutherford Appleton Laboratory. The fabrication of the dipoles and associated filters was performed in two stages. The Rutherford Appleton MMT direct-write UV system is first used to pattern a Nichrome mask with the required dimensions. This mask was then used to pattern multiple copies of the required structure.

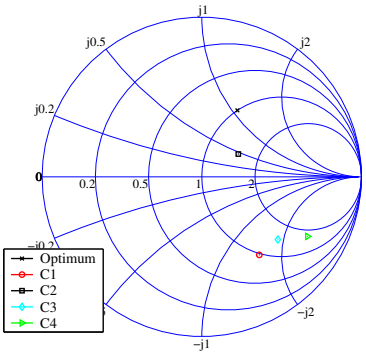

Figure 5.21: Predicted diode embedding impedance at 500 GHz for the selected configurations. Note that the reference impedance has been taken as 14 Ω for the sake of improved visibility.

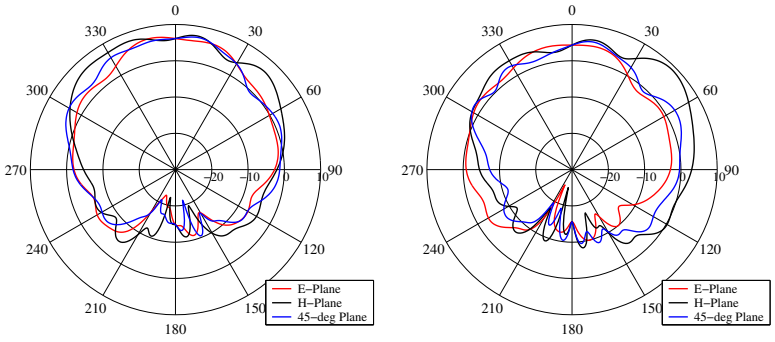

(a) C1 (b) C2

(c) C3 (d) C4

Figure 5.22: Predicted radiation pattern at 500 GHz of the selected configurations.

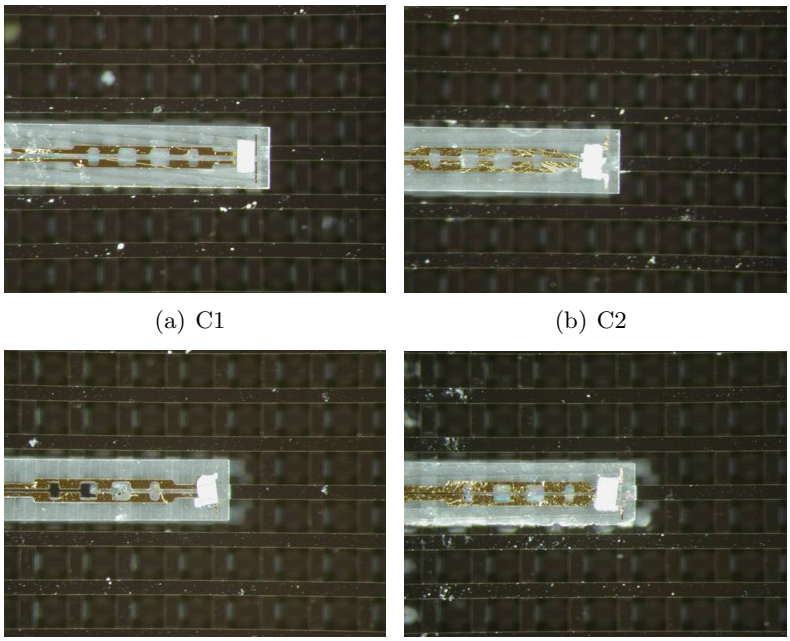

(a) C1 (b) C2

(c) C3 (d) C4

Figure 5.23: Photographs of the manufactured circuits.

The advantage of this two stage process arises from the time required for the exposure of the initial mask, which can be up to one day per filter. The direct-write process also favours the patterning of as small an area as possible, as maintaining the uniformity of focus of the UV spot is more difficult over larger distances. Hence it is better to make a master mask and to translate this to form the array.

The second stage of the fabrication is to transfer these structures to a pattern of photoresist on a gold-on-quartz substrate. A gold thickness of 1.5 μm will be required for the efficient and safe soldering of the diode. The quartz substrate material for this metal layer has been prepared by RF sputtering a Nichrome adhesion layer followed by a gold seed layer for electroplating. A jig was used for the electroplating process which was used to build the gold thickness to the required 1.5 microns. Once the dipoles are fabricated, the diodes are soldered on to them. The resulting configurations are shown in Figure 5.23.

In order that the woodpiles with several attached dipoles can be measured,

Figure 5.24: Jig used for the antenna pattern measurements.

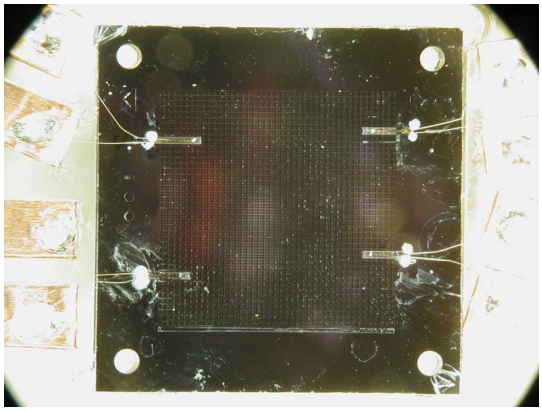

Figure 5.25: Photograph of the 4 detector configuration on top of the silicon woodpile structure.

a suitable fixture was designed to hold the woodpile and at the same time allow low frequency electrical contact to each of the dipoles. The fixture was built to attach directly onto the rotating stage of the measurement apparatus in the University of Bern. The jig consists of a low dielectric constant TPX plate, which has a square recess which serves to position the woodpile above an circular aperture, see Figure 5.24. SMA connectors are fixed at several positions around the edge of the TPX plate. The dipoles are connected with thin gold wire to the nearest of these connectors in each case. A photograph of the dipoles once placed on top of the woodpile structure is shown in Figure 5.25.

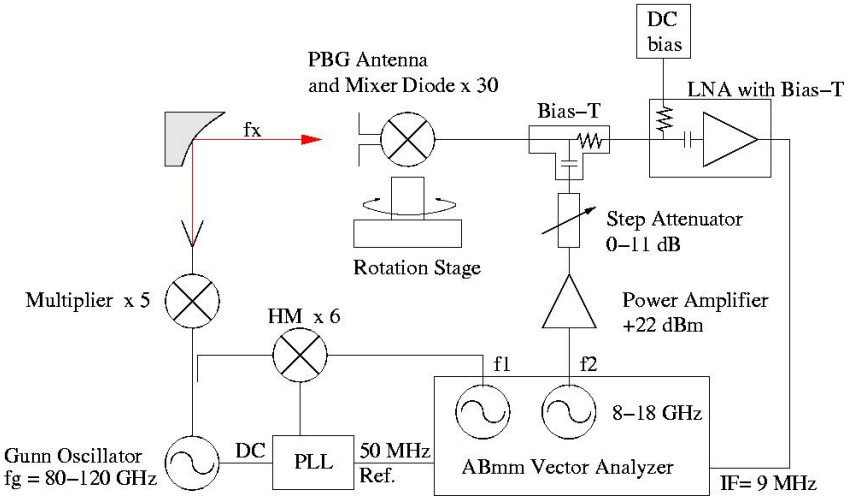

Figure 5.26: Block diagram of the antenna pattern measurement set-up.

5.5 Measurements

5.5.1 Measurement set-up

The radiation pattern measurements were carried out at the Institute of Applied Physics, Bern. The measurement set-up consisted of a feed horn and two mirrors, a paraboloidal and a planar one. The block diagram is presented in Figure 5.26. For the measurements at 500 GHz, a Gunn oscillator generated a 100 GHz signal that was the input signal of a multiplier by 5. The output of the multiplier was radiated by a horn antenna and focussed by the quasi-optical set-up previously described. The power detected by the samples was sub-harmonically down-converted in the detecting diode to an intermediate frequency (aprox. 9 KHz) using the 30th harmonic of an LO frequency of approximately 16.66 GHz (500/30). The power level of the LO signal was optimised using one amplifier and one attenuator in order to obtain the maximum detected signal. To generate the other frequencies the output frequency of the Gunn oscillator and the LO frequency were modified accordingly.

The sample was attached to a rotating stage to perform the scanning. Since the rotating stage rotated only in 1 plane, both feeding antenna and sample were rotated by 90 deg in order to change from H-Plane to E-Plane measurement. Pictures of the measurement set-up are presented in Figure 5.27 and Figure 5.28.

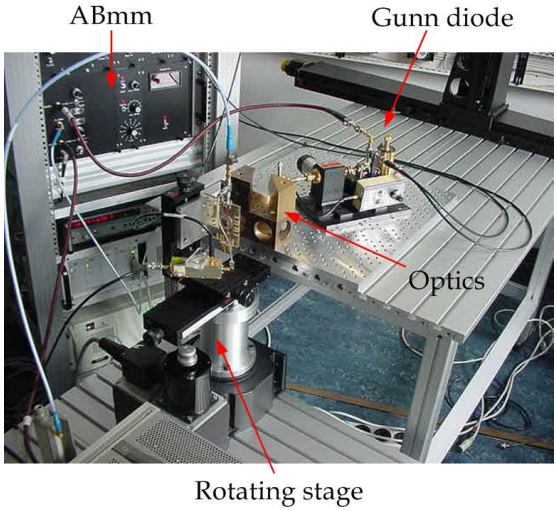

Figure 5.27: Antenna pattern measurement set-up. For the sake of visibility, the absorbing material was removed.

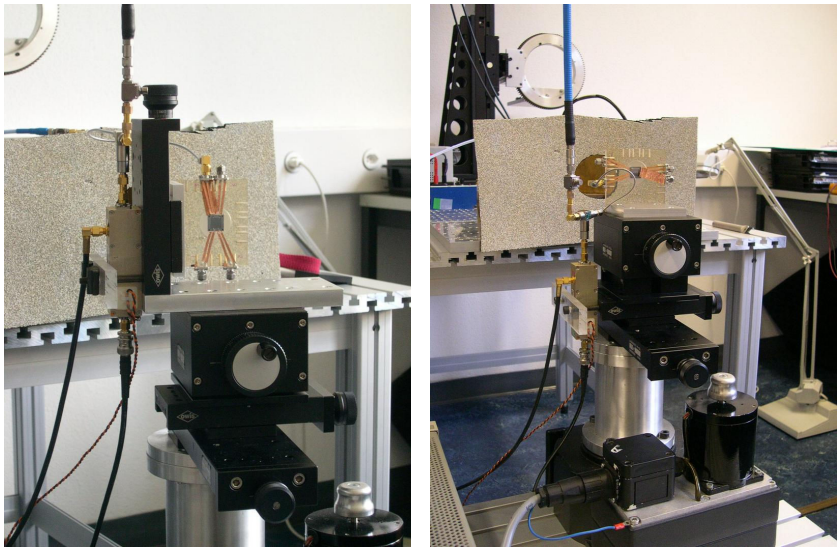

(a) (b)

Figure 5.28: Antenna pattern measurement setup. (a) E-Plane measurement (b) H-Plane measurement.

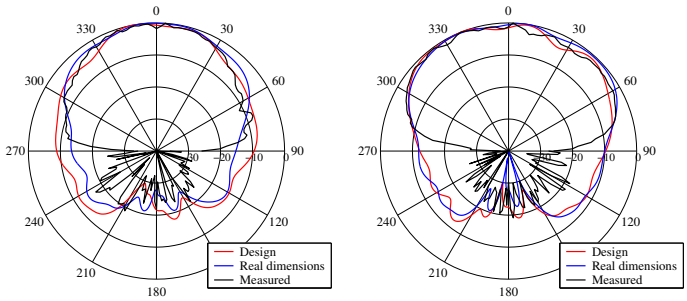

(a) E-Plane (b) H-Plane

Figure 5.29: Comparison between the predicted and measured radiation patterns at 500 GHz for configuration C1. Each curve has been normalized to its maximum.

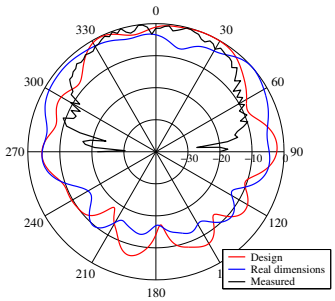

Figure 5.30: Comparison between the predicted and measured E-Plane radiation pattern at 500 GHz for configuration C2. Each curve has been normalized to its maximum.

5.5.2 Radiation pattern measurements

The measured radiation patterns at 500 GHz corresponding to the proposed configurations are presented from Figure 5.29 to Figure 5.32. For the configuration labelled as C2 only the E-Plane could be measured, since the diode stopped working during the alignment of the H-Plane measurement. For the same reason the back radiation could not be meassured either.

In all cases the measured results are compared with the predictions using the design dimensions and the real dimensions of the manufactured circuits. With respect to the manufactured circuits, the maximum offset between design and fabricated dimensions was measured to be always less than 10 m, the larger deviations corresponding to the width of the lines. The agreement between both sets of simulations is good.

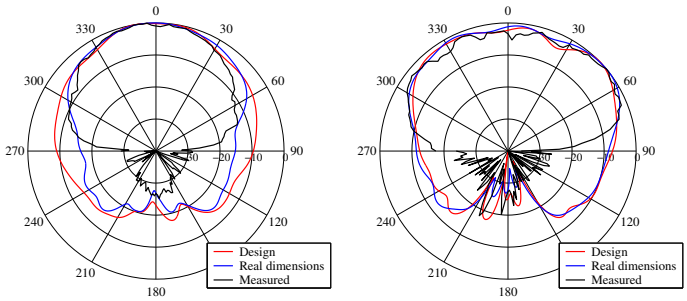

(a) E-Plane (b) H-Plane

Figure 5.31: Comparison between the predicted and measured radiation patterns at 500 GHz for configruration C3. Each curve has been normalized to its maximum.

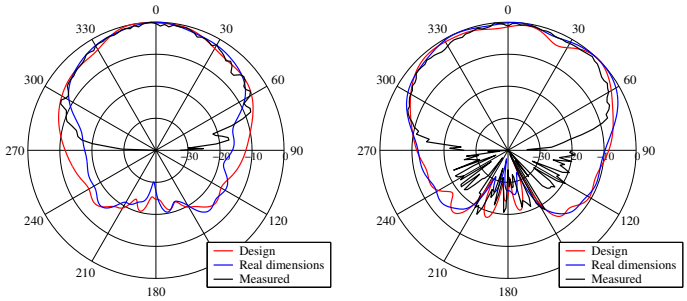

(a) E-Plane (b) H-Plane

Figure 5.32: Comparison between the predicted and measured radiation patterns at 500 GHz for configruration C4. Each curve has been normalized to its maximum.

The agreement between predictions and measurements is good for the main beam between -75^o and 75^o. For larger angles the prediction levels are always higher than the measurements. With respect to the back radiation, the predicted levels are also much higher than the measured ones. In both cases the reason for this discrepancy is the same. Since the size of the woodpile that is being considered in the simulations is only $11 \times 11 \times 2$ periods, there is some diffraction at the woodpile edges, which increases the predicted radiation levels.

This deviation should be even larger, as the back radiation could not be accurately measured. The reason was that the size of the beam was large enough so as to have some spillover on the woodpile edges which increased the back radiation levels.

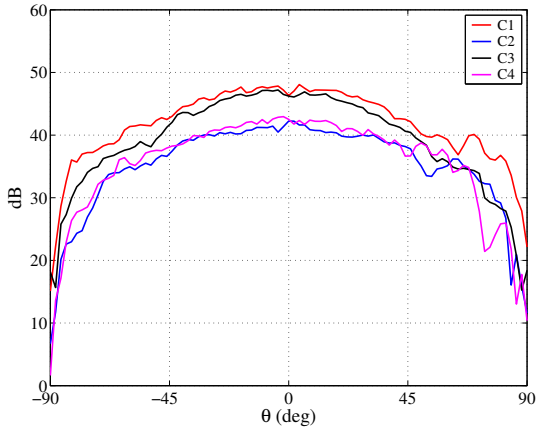

Figure 5.33: Comparison between the measured E-Plane at 500 GHz for the different configurations.

5.5.3 Sensitivity of the configurations

One of the goals of the previous studies is to achieve a sensitive detecting configuration. In order to compare the signal levels obtained with the different configurations, the results obtained for the E-plane at 500 GHz are shown in Figure 5.33. Two of the configurations, C1 and C3, present the highest detected levels, whereas it is lower for the other two ones. These results match the predictions in terms of power coupling to the diodes, since the best configurations according to it should be C1 and C3, as it was pointed out in section 5.3.5.

However, there are several uncertainties with respect to these results. First, the parameters of the diodes are different, as can be seen in Table 5.1. In particular, two of these diodes present values of the ideality factor parameter quite different from their nominal value according to the datasheet, which is around 1.2. In these cases the response of the diodes is less ideal, which could make their response different. In any case, the detected power does not seem to be directly linked to the diode characteristics, since the best results were obtained with one of the diodes which were more different from their nominal values. Also the series resistance of the diodes is different, being minimum for the two configurations which showed higher detected powers. This parameter could also justify the difference between the configurations, since the highest series resistance corresponds to the lowest detected power level.

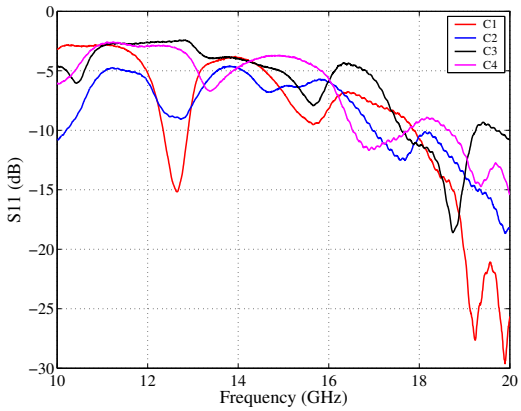

Figure 5.34: Measured S11 at the SMA connectors of the diode configurations.

Moreover, the measurement results correspond to subharmonic mixing in the Schottky diode and the level of the detected power depends very strongly on the pumping of the diodes by the LO signal, around 16.6 GHz in this case. Although the LO power was optimised for maximum detected level in some cases the maximum available power was used, meaning that that point had not been reached. In order to have an insight on the behaviour of the feeding lines at LO frequencies the S_{11} presented by the four configurations in the frequency range used in the measurements is shown in Figure 5.34. Although the best S_{11} corresponds to the worst configurations in terms of detected levels, this does not imply that the diodes were more pumped in configurations C1 and C3, since the LO level was optimised for each configuration.

In order to rule out these uncertainties, the diodes should be more similar and a direct detection system should be used.

Configuration	R_s **(Ω)**	η
C1	45	3.09
C2	57	1.74
C3	49	1.65
C4	76	3.42

Table 5.1: Measured parameters of the diodes used in the different configurations.

Chapter 6

Subharmonic mixer using EBG technology

6.1 Introduction

In the previous chapter the design of a detector using EBG technology has been presented. A more advanced receiver configuration will use coherent detection. This detection technique brings some advantages, such as improving the sensitivity of the receiver and allowing for the possibility of electronic scanning.

Coherent detectors require the LO oscillator signal to be guided to the mixers. This can be technologically difficult in the millimetre wave range, especially if the array is two-dimensional, due to the difficulties to build 3-dimensional circuitry, for instance power splitters. The use of EBG technology can alleviate this problem, due to the possibility of building 3-dimensional circuitry using this technology [Man03a; Ede03b].

In this chapter, the design of a subharmonic mixer using EBG technology is presented. Part of this design was developed during the Startiger project. In this project an imager working at 250 and 300 GHz was designed and manufactured. One of the side activities of this project was to explore the possibility of using EBG technology for imaging applications and in particular to design a coherent detector using this innovative technology. Due to the limitation in frequency and power of the available sources, subharmonic operation of the mixer was required. However, the selected EBG structure, a silicon woodpile, does not have a bandgap large enough so as to cover both the

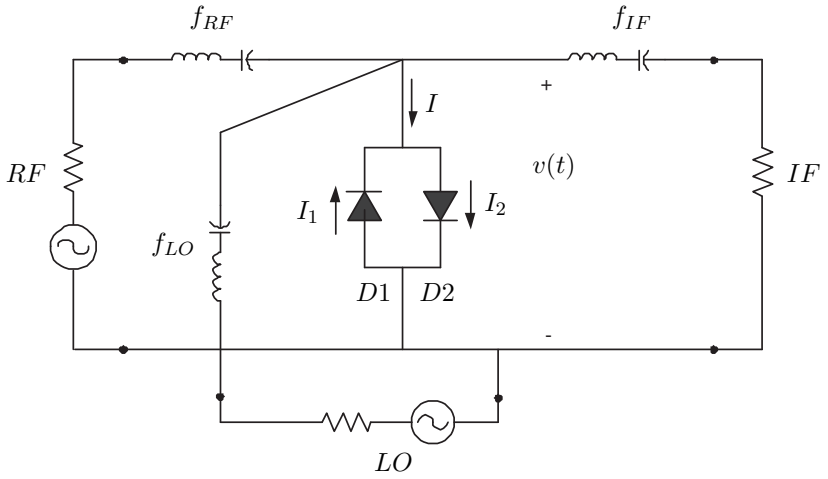

Figure 6.1: Schematic of a subharmonic mixer.

LO and RF frequencies, which are separated one octave. This fact discarded the possibility of a subharmonic mixer design using only EBG technology and the design combined both EBG and conventional technologies. Although in order to take full advantage of this technology and to avoid losses resulting from the transitions between different technologies, the whole system should be completely realised using EBG technology; this is a first step towards a fully-integrated EBG receiver which, as it was explained, should be based on harmonic mixing.

6.2 Subharmonic mixer operation

An schematic showing a subharmonic mixer configuration is shown in Figure 6.1. It consists of an antiparallel diode pair and filters to separate the different frequencies, much as if it were a single diode mixer [Maa93]. If the diodes are identical this circuit has no fundamental mixing response.

For the analysis of this configuration it can be considered that the current generated in the nonlinear conductance of a diode by a voltage V is described by [Man92]:

$$I = f(V) = aV + bV^2 + cV^3 + dV^4 + eV^5..., \tag{6.1}$$

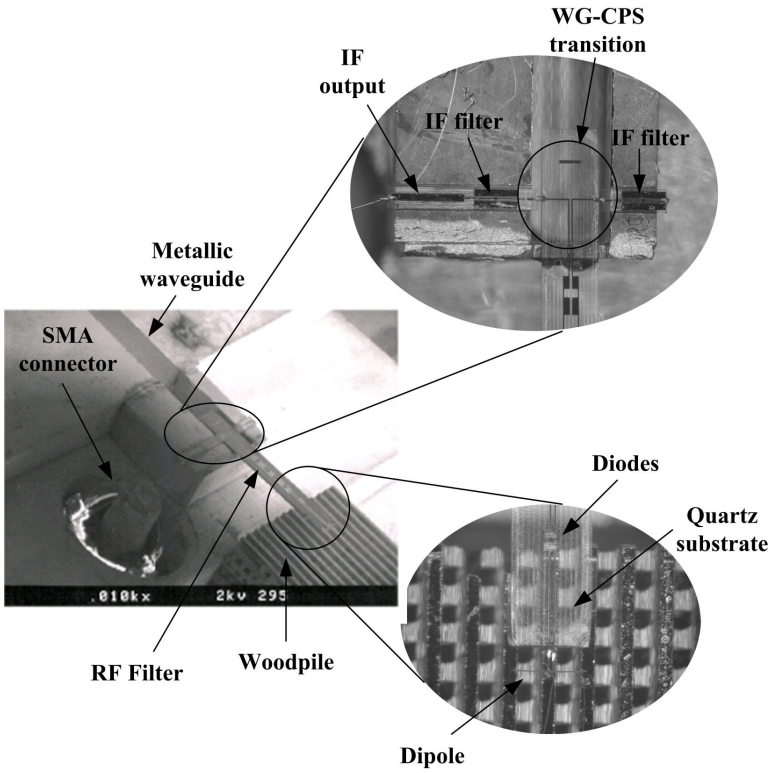

Figure 6.2: EBG mixer configuration.

where a,b,c,d,... are real constants

If the convention used in Figure 6.1 is maintained, we have for a diode operating in the reverse direction, such as $D1$, that the current is described by:

$$I_1 = f(-v) = -av + bv^2 - cv^3 + dv^4 - eV^5... \tag{6.2}$$

whereas for a diode operating in the forward direction, such as $D2$, the current is

$$I_2 = f(v) = av + bv^2 + cv^3 + dv^4 + eV^5... \tag{6.3}$$

Therefore the total current outside the diode loop is

$$I = -I_1 + I_2 = 2av + 2cv^3 + 2ev^5... \tag{6.4}$$

Assuming a sinusoidal dependence of both the LO and RF signal, the analysis of this equation shows that there is no presence at the output of the even LO harmonics and all frequencies $mf_{RF} + nf_{LO}$, where $|m| + |n|$ is even [Maa93]. Therefore, fundamental mixing, which corresponds to the term $m = 1$ and $n = 1$, is not allowed in this configuration and subharmonic mixing will be the main output.

6.3 Configuration

The designed sub-harmonic mixer operates around 250 GHz RF frequency, with LO frequency around 125 GHz. The IF frequency used was 4 GHz. An anti-parallel Schottky diode pair is used as the mixing element. Two notch filters centred at the RF and LO frequencies are used to separate the frequency bands, providing the required isolation between ports.

A picture showing the configuration studied is shown in Figure 6.2. The mixer is built on a Coplanar Stripline (CPS) circuit placed on top of the woodpile, using a dipole antenna to collect the RF radiation. Since the LO source output is in metallic rectangular waveguide (WR-8) and the mixer is built in CPS technology, a transition between both technologies is required. The IF circuitry is achieved via micro-strip circuitry enclosed in a rectangular metallic cavity. This configuration can be seen as the first step towards the design of a full EBG mixer, in which the LO waveguide would be implemented in EBG technology.

The different parts of the configuration are explained in detail in the following sub-sections.

6.3.1 LO waveguide to Coplanar Stripline (CPS) transition

The transition from metallic rectangular waveguide (WR-8) to CPS (shown in Figure 6.6) is based on a Quasi-Yagi antenna [Kan99]. This consists of a dipole and a director printed on a 0.05 mm thick quartz substrate and placed inside the rectangular waveguide along its E-Plane. The substrate was introduced into the waveguide through a 0.1 mm opening in the short-circuited waveguide end. The width of the output CPS lines was 0.025 mm and the separation between them was 0.02 mm.

Two stop band IF filters are connected to the two arms of the dipole. They were designed using microstrip waveguide channel technology, using the same 0.05 mm thick quartz substrate and positioned within a 0.2 mm x 0.1

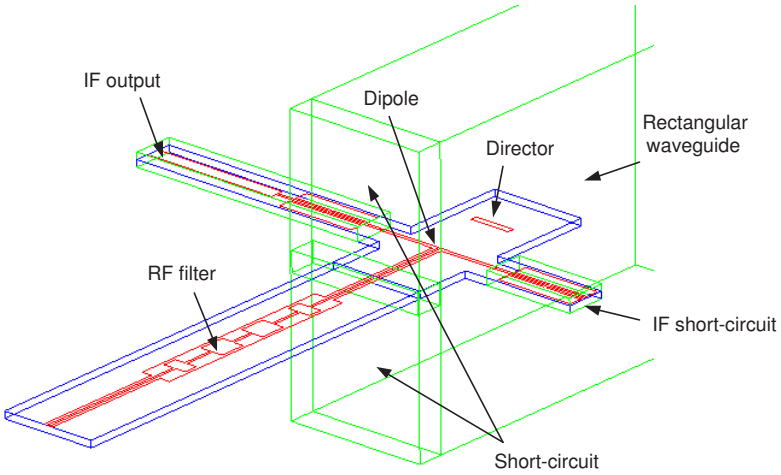

Figure 6.3: Schematic of the rectangular waveguide to CPS transition.

mm channel. The purpose of these filters is to provide the IF output and the short-circuited ground return required by the diodes. Since the filters present very high impedance at LO frequency the performance of the transition is not degraded by their inclusion.

6.3.2 RF filter

The low-pass filter is placed between the output of the waveguide-CPS transition and the dipole antenna. It blocks the RF radiation whilst letting the LO pass. Its design was based on connecting alternated sections of high and low impedance CPS. Since it presents very high impedance at RF frequencies it was also used as tuning element for the RF diode embedding impedance as will be commented in section 6.4.4.

6.3.3 EBG antenna

A dipole placed on top of a woodpile structure was used as the antenna. The silicon woodpile consisted of 5 periods in the stacking direction and 15 in the other two planes. Due to fabrication constraints in this case the woodpile was not the optimum in terms of fractional bandwidth. Its relevant dimensions

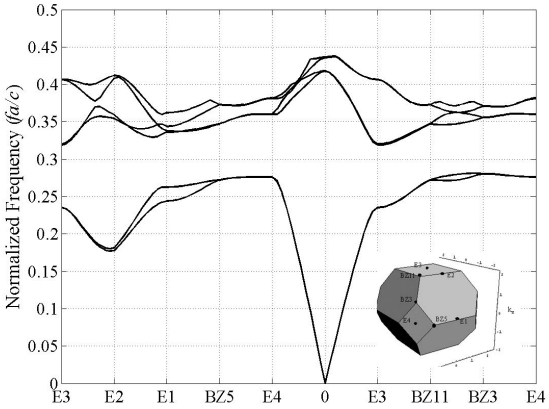

Figure 6.4: Band diagram of the used EBG structure.

are: $a = 0.36$ mm, $ca = 0.62$ mm and $d_1 = d_2 = 0.155$ mm (see Figure 2.9 for the description of the woodpile parameters). A bandgap of 10.9 % relative bandwidth around 250 GHz is achieved with this particular woodpile, see Figure 6.4.

As in the previous case, the dipole antenna was placed in the "perpendicular solid-solid" symmetry position, i.e. the dipole feed lines run along a bar in the top layer and its arms overlay a perpendicular bar in the layer immediately below. The dipole was based on CPS technology on a quartz substrate. However, in this case the quartz substrate was removed from underneath the dipole region, so that it effectively radiated in air.

This configuration is different from those presented in the previous chapters, in which the quartz was not removed under the dipole. The reason for this is that at the time this design was carried out, the studies about the input impedances of the dipoles antennas on top of the woodpile were not performed yet. Therefore, this design took as starting point [Gon01], in which a similar dipole configuration was used. However, in our case the dipole is placed at the "perpendicular solid-solid" symmetry position and not in the "parallel void-void", as it was in [Gon01]. This new position allows to achieve a better matched configuration, although at the expense of a less improved radiation pattern.

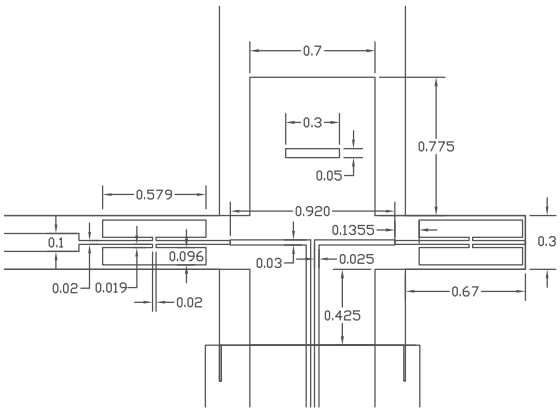

Figure 6.5: Dimensions of the rectangular waveguide to CPS transition.

6.4 Modelling

The following sections describe the modelling of the different parts that constitute the EBG mixer.

6.4.1 Waveguide to CPS transition

The performance of the transition was optimised by adjusting the distance from the short-circuited end of the waveguide to the dipole, and the director length and its distance to the dipole. The optimum distance between the dipole and the end of the waveguide was found to be 0.56 mm and the director length and distance to the dipole were 0.3 mm and 0.46 mm respectively. The rest of dimensions of the transition are given in Figure 6.5. The transition performance including the RF filter is shown in Figure 6.6. The coupling from the waveguide port to the CPS port is a maximum at the design frequency (125 GHz) giving a return loss of 15 dB. Good isolation (-28 dB) with respect to the IF port was also achieved.

The isolation to the IF port is mainly caused by the two notch filters that are attached to the arms of the dipole. Its frequency response is presented in Figure 6.7. The rejection at LO frequencies is about 29 dB whereas at frequencies lower than 10 GHz the transmission is total.

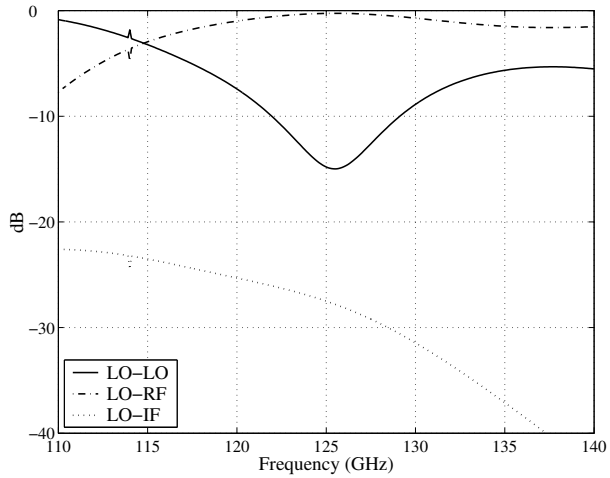

Figure 6.6: Performance of the rectangular waveguide to CPS transition.

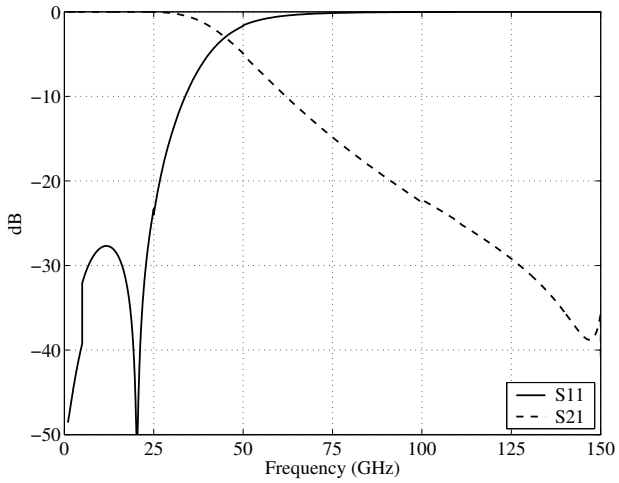

Figure 6.7: Performance of the IF filter.

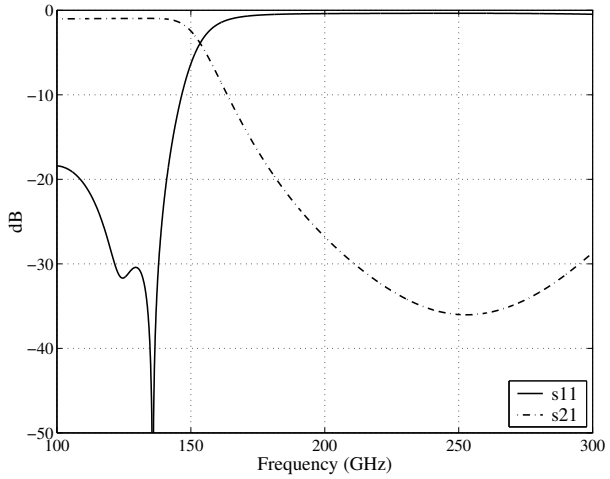

Figure 6.8: Performance of the RF filter.

6.4.2 RF filter

This low-pass filter blocks the RF signal whilst letting the LO pass. It was designed by connecting alternated sections of high and low impedance CPS. The filter predicted performance can be seen in Figure 6.8. At RF frequencies, i.e. around 250 GHz, the transmission is lower than -30 dB whereas at LO frequencies, i.e. around 125 GHz, the insertion losses are about 1dB, mainly due to the radiation inherent to any open configuration. The dimensions of this filter are shown in Figure 6.9.

6.4.3 EBG antenna

As it was mentioned previously, the dipole antenna radiated in air, although the CPS feeding lines were printed onto a 40 microns thick quartz substrate. The dipole antenna was printed onto a quartz substrate metallised with 2 microns of gold. The matching of the dipole was optimised by modifying the dipole length and width, and the quartz substrate thickness, which effectively modified the distance between the dipole and the woodpile. The optimum values for these parameters were found to be 0.34 mm, 0.025 mm and 0.05 mm, respectively.

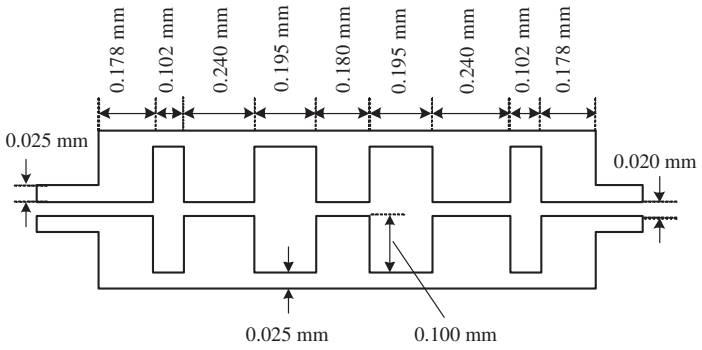

Figure 6.9: Dimensions of the RF filter.

The predicted return loss of the design is shown in in Figure 6.10(a). Return loss values better than 20 dB were obtained in a 9% bandwidth around the design frequency. Figure 6.10(b) shows the predicted radiation pattern at 250 GHz obtained with this configuration. The improvement achieved with respect to a dipole radiating in air is not as large as previously reported [Gon01]. The reason for this is that the selected configuration ("perpendicular solid-solid" symmetry position, i.e. dipole perpendicular to the top layer bars and overlaying a bar in the layer immediately below) is different from that used in [Gon01] ("parallel void-void" symmetry position, i.e. dipole parallel to the top layer bars and placed in between two of these bars), allowing to achieve a better matching but at the expense of smaller improvement in radiation pattern.

The width of the main quartz substrate was imposed by the rectangular waveguide to CPS transition. In order to keep the fabrication as simple as possible, a constant width was required by the dicing process used to separate the substrates. This limitation, together with the substrate thickness needed for a good matching, caused some interaction of the dipole radiation with the substrate. Although the dipole was separated from the substrate as much as possible, i.e. 0.25 mm, there was some degradation of the radiation pattern caused by the substrate. It is clear that the effect of dielectric close to the dipole can greatly affect the resulting radiation pattern and interaction with the EBG backing plane. The use of a substrate that narrower in the vicinity of the dipole (as shown in Figure 6.11(b)) would have avoided this problem, but at the expense of a more complicated fabrication procedure.

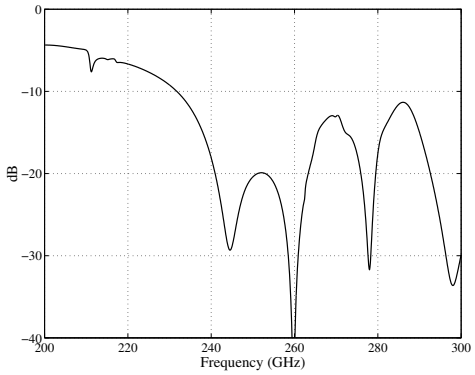

(a)

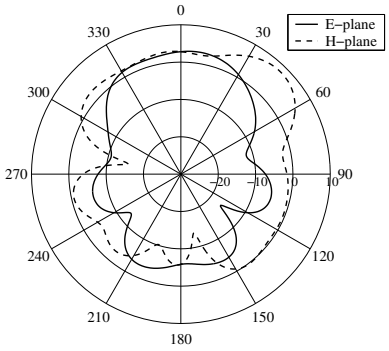

(b)

Figure 6.10: (a) Return loss and (b) radiation pattern of the EBG antenna.

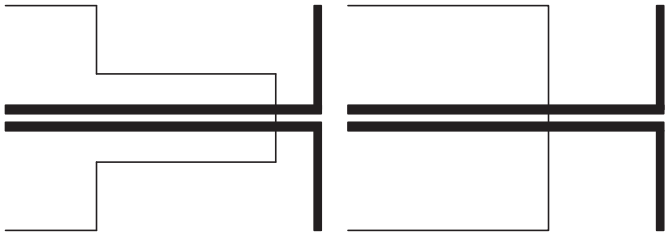

(a) (b)

Figure 6.11: Antenna configurations.

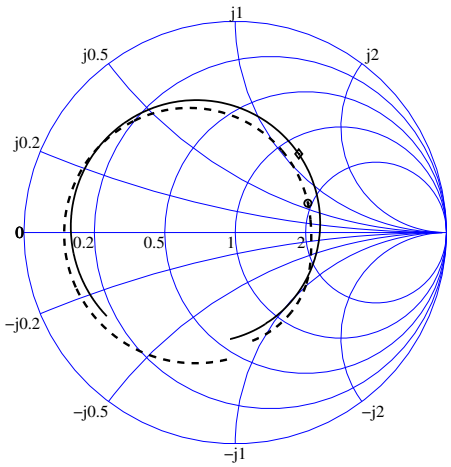

Figure 6.12: Diode embedding at RF (solid line) and LO (dashed line) frequencies.

6.4.4 Diode embedding impedance

The mixer design is based on the adjustment of the embedding impedance of the diodes at both RF and LO frequencies. The diode embedding impedance was obtained using HFSS software. To include the diodes in the HFSS simulations, The same model described in the previous chapter was used (see section 5.3.1). In this model a lumped gap source was placed at the diode mesa to measure the embedding impedance that is effectively presented to the diode.

The Harmonic Balance analysis carried out showed that the optimum diode embedding impedance for minimal noise temperature at both RF and LO were found to be in the region of $50 + j50\ \Omega$ and $50 + j100\ \Omega$ respectively.

At the RF frequency, the diode embedding impedance was optimised by varying the distance from the RF filter to the diodes and separation between the lines at the point where the diodes were placed. The separation between lines at the position of the diodes was asymmetric since it was used to provide part of the required reactance. The predicted RF diode embedding impedance as function of frequency is shown in Figure 6.12. At 250 GHz, the achieved diode embedding impedance was $55 + j59\ \Omega$.

At the LO frequency the only parameter that was used to optimise the diode embedding impedance was the distance from the diodes to the dipole

antenna. Since the antenna is not resonant at these frequencies it acts as an open circuit. Therefore, it can be used as matching element to obtain the required diode embedding impedance. The results are presented in Figure 6.12. At 125 GHz, the diode embedding impedance was $91 + j36\ \Omega$. It is clear that the LO power requirement could be reduced with an improved LO circuit. However, the emphasis for the design was placed on achieving the best RF performance. This will become and important design parameter for arrays of mixers where LO power will be a more valuable commodity.

The dimensions of the final configuration are shown in Figure 6.14.

6.4.5 Simulated mixer performance

Once the S parameters at the different mixer harmonics $mf_{IF} + nf_{LO}$ were obtained using HFSS, the prediction technique proposed by Kerr [Ker79] for subharmonically pumped mixers was applied to compute the Double Side Band (DSB) noise temperature. For the simulation, the same values as in the previous chapter were taken for the UMS diode parameters: series resistance $R_s = 8.6\,\Omega$, ideality factor $h = 1.283$, saturation current $I_s = 1.031 \times 10^{-13}\,A$, and zero bias junction capacitance $C_{j0} = 9.5\,fF$. The series inductance, L_s, was neglected, since it was supposed to be computed in the HFSS model of the diode. Finally, it was assumed that both diodes see the same embedding impedances.

Predicted DSB noise temperature as function of frequency, for an IF frequency of 4 GHz and varying LO powers at the diodes is presented in Figure 6.13(a). For LO power values between 1 mW and 2 mW, the mixer bandwidth increases very rapidly and the DSB noise temperature decreases. For higher LO powers the increase in bandwidth varies more slowly and the DSB noise temperature is quite flat over the whole bandwidth. The noise temperature is a minimum for 2 mW LO power and increases slightly for higher LO powers, especially for frequencies higher than 121 GHz. The widest bandwidth corresponds to the highest considered LO power, i.e. 5 mW. In this case the minimum DSB noise temperature is 912 K, with an average value of 1500 K for frequencies between 115 GHz and 137 GHz.

With respect to the DSB mixer conversion loss, predicted results as function of frequency, for an IF frequency of 4 GHz and different LO powers are presented in Figure 6.13(b). As for the mixer noise temperature, the best conversion losses are achieved for LO powers between 2 mW and 3 mW. For higher LO powers the conversion loss is quite flat in the band between 116

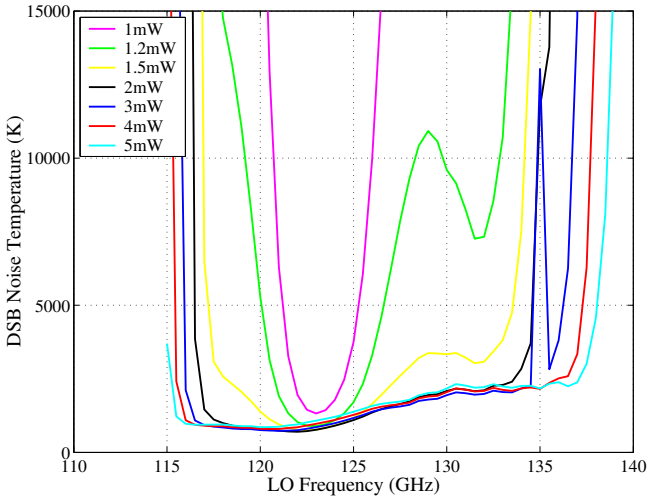

(a)

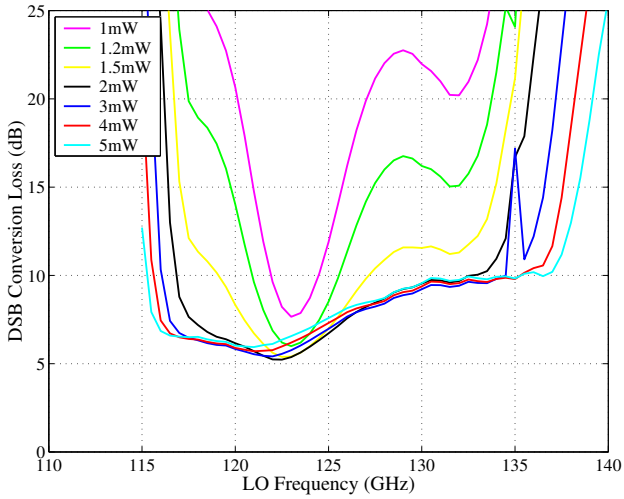

(b)

Figure 6.13: Predicted mixer performance: (a) DSB noise temperature and (b) DSB conversion loss.

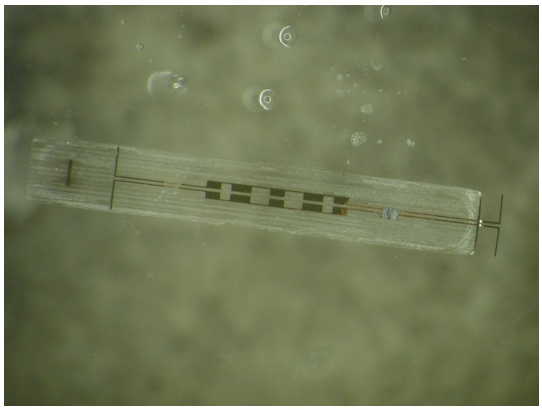

(a) CPS substrate

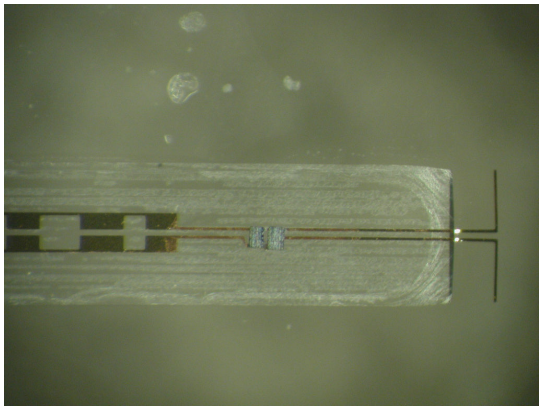

(b) Close up of the diodes and dipole antenna

Figure 6.14: Photographs of the fabricated CPS substrate.

GHz and 135 GHz, with values ranging from 5.2 dB to 10 dB. Also in this case the widest bandwidth corresponds to the highest considered LO power, i.e. 5 mW.

6.5 Fabrication

The EBG mixer was fabricated at the Rutherford Appleton Laboratory (RAL). The woodpile was built using high resistivity silicon following the dicing manufacturing process described elsewhere [Gon02].

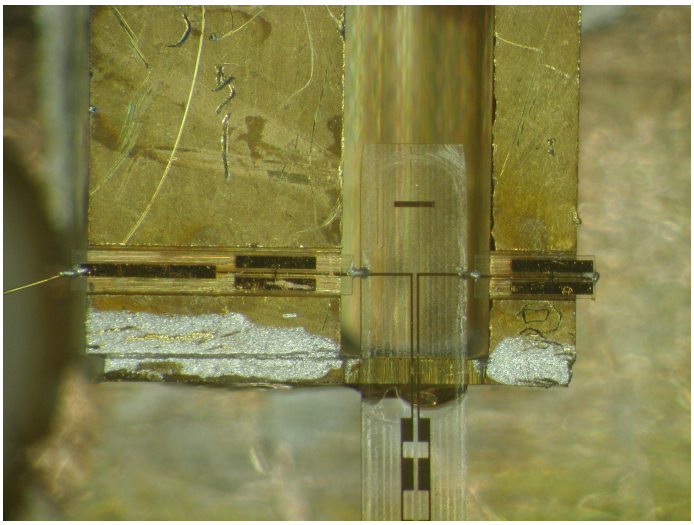

Figure 6.15: Photograph of the waveguide to CPS transition.

The CPS and micro-strip circuits were fabricated on 0.05 mm quartz substrates using lithographic techniques. The waveguide to CPS transition required a cross-shape substrate. In order to keep its fabrication as simple as possible the substrate was split in to three sections. Two of them, which corresponded to the arms of the cross, contained the two IF filters. The central part, CPS substrate from here on, contained the RF dipole, the RF filter and the dipole and director of the waveguide to CPS transition. The portion of substrate under the antenna was etched away to remove the quartz and leave the dipole radiating in air.

The diodes were diced in order to decrease their overall size, reducing their capacitance and improving their high frequency performance. After being diced they were soldered onto the circuit with a low melting temperature solder. Photograph of the CPS substrate are shown in Figure 6.14.

For expediency, critical parts of the waveguide circuit, LO waveguide and IF channels were fabricated in silicon using a dicing process and afterwards metallised with nichrome and gold to a thickness of 2 microns. They were manufactured as two halves and then glued together using silver epoxy. Finally, the CPS circuitry was placed in its location and the whole assembly was then glued into a conventionally machined metal housing. The LO waveg-

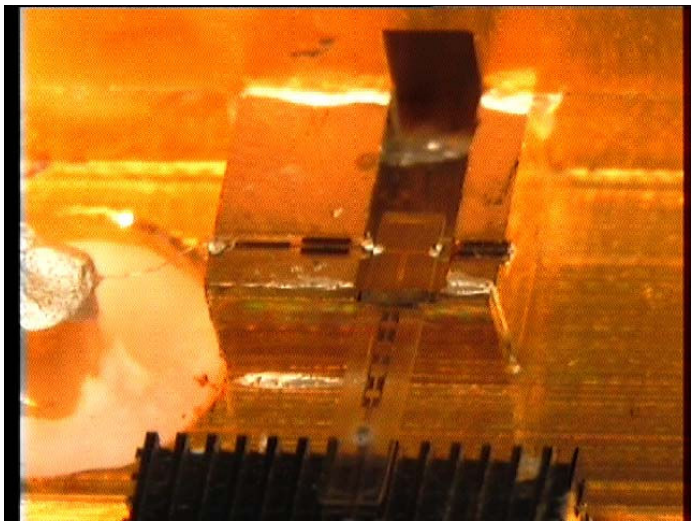

Figure 6.16: Front view of the complete mixer assembly. Note that the upper half of the waveguide has been removed for the sake of visibility.

uide was short-circuited using two metallised silicon blocks, which created the aperture required to introduce the central substrate inside the circuit. The CPS substrate was supported by one of these blocks and the woodpile. Once aligned with the IF substrates the metallic lines were soldered (see Figure 6.15 for a photograph of the assembled transition). One of the IF filters was connected to the waveguide body to provide the required ground return whereas the other one was connected with a bounding wire to a SMA connector, which constituted the IF output.

A front view photograph of the complete mixer assembly is shown in Figure 6.16.

6.6 Measurements

The EBG mixer noise performance was characterised using standard techniques. A schematic of the measurement set-up is shown in Figure 6.17. A backward-wave oscillator (BWO), tuneable from 110 GHz to 140 GHz, was used as the LO source. The LO power that fed the mixer was varied using an attenuator. A 10 dB directional coupler together with a power meter was

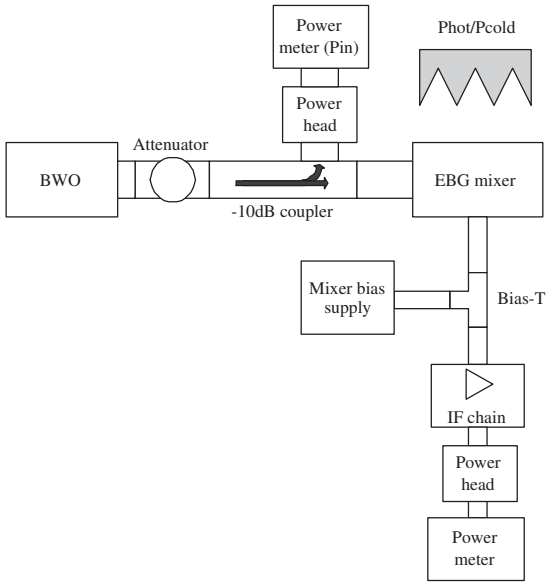

Figure 6.17: Mixer measurement setup.

used to monitor the LO power. The output of the directional coupler, P_{in} in Figure 6.17, is used as a parameter in most of the following plots. The mixer IF output was connected to a low noise amplifying chain (42 dB gain) operating in the 2 - 6 GHz range. The IF noise temperature was characterised using the Y-factor method [Maa93] and was measured to be 350 K.

The diodes were found to be slightly unbalanced, resulting in a non-optimum operation of the mixer. The reason of this behaviour could be that both diodes were not identical or that there was a small asymmetry in its position. A DC voltage was used to balance them so that their average DC current was zero. The compensation voltage for different LO powers is shown in Figure 6.18.

The performance of the receiver in terms of noise temperature was measured with the Y-factor technique, using a blackbody (Eccosorb AN72 absorber) at room temperature (294 K) as hot source and a liquid nitrogen cooled blackbody (77 K) as cold source. The DSB receiver noise temperature results for 2 - 5 mW LO source powers are presented in Figure 6.19. For values of the detected input power lower than 0.1 mW measured at the output of the 10dB coupler (1 mW coupled to the mixer approx.) no mixing effect is ob-

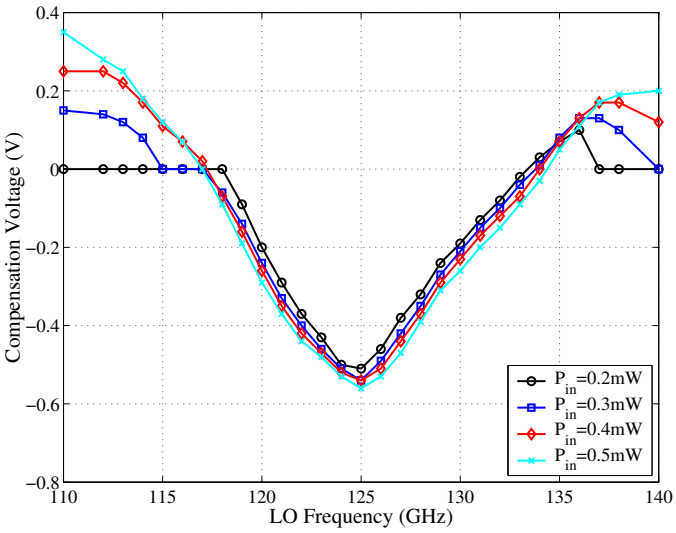

Figure 6.18: Compensation voltage vs. LO frequency for different LO powers.

served. For higher power values (2 - 5 mW) the receiver shows two frequency ranges, from 117 GHz to 126 GHz and from 131 GHz to 136 GHz, were the DSB receiver noise temperature reaches minimum values. The two bands are separated by a resonance that was already predicted in our simulations for low LO powers. Both bands broaden when the input power is increased in agreement with the predictions.

The mixer DSB noise temperature can be extracted from the receiver DSB noise temperature and the IF chain noise temperature [Maa93] using:

$$T_{MIX} = T_{REC} - \frac{T_{IF}}{G_{MIX}}, \tag{6.5}$$

where G_{MIX} is the gain of the mixer,

$$G_{MIX} = \frac{P_{REC,H} - P_{REC,C}}{P_{IF,H} - P_{IF,C}}, \tag{6.6}$$

and T_{IF} and T_{IF} are the DSB noise temperature of the IF chain and the receiver respectively, both calculated previously.

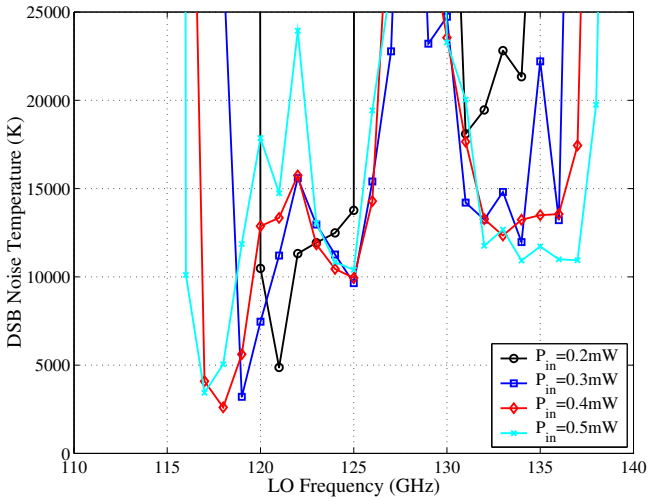

Figure 6.19: Measured DSB receiver noise temperature vs. LO frequency for different LO powers.

The results for the DSB mixer noise temperature are presented in Figure 6.20(a). As in the receiver noise temperature case, there are two frequency bands, were the DSB noise temperature of the mixer reaches a minimum. The two bands are separated by the same resonance previously observed. The performance of the mixer in terms of noise is slightly better in the lower frequency band where the average noise temperature is 3500 K whereas in the higher frequency band is 6500 K. Input powers between 3 mW and 4 mW, which correspond to monitored powers (P_{in}) of 0.3 mW and 0.4 mW, gave the best results in terms of noise temperature. If the power is increased to 5 mW the bandwidth increases but eventually at the expense of an increase of the DSB noise temperature. The minimum measured DSB noise temperature was 938 K for a 4 mW LO power at 118 GHz.

The mixer conversion loss is shown in Figure 6.20(b). The frequency bands where the noise temperature is minimum corresponds to those where the conversion loss is lower. The best values, between 6.3 and 13 dB were also achieved with 3 mW and 4 mW LO power.

These results are in good agreement with the predictions shown in Figure 6.13. The frequency limits of the mixer bandwidth were correctly predicted.

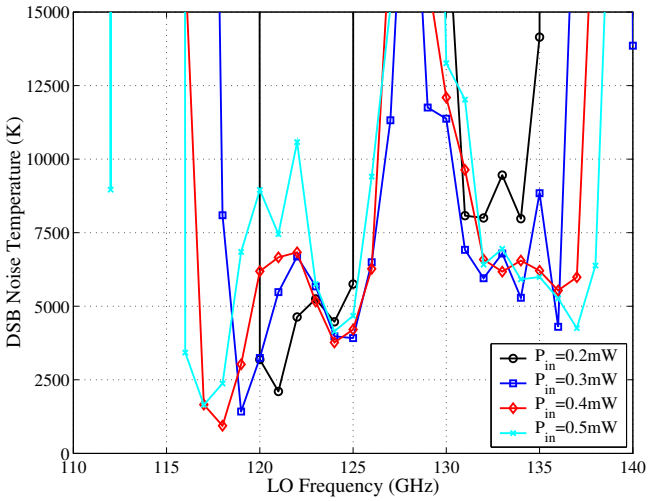

(a)

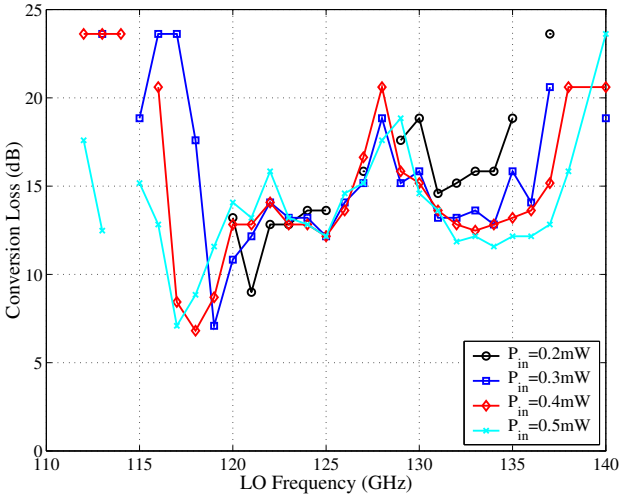

(b)

Figure 6.20: Measured mixer performance: (a) DSB noise temperature and (b) DSB conversion loss.

With respect to the peak at 128 GHz, it is also predicted in the simulations but for lower LO powers. However, the power levels that have been measured were taken at the entrance of the circuit and therefore did not take into account the losses: ohmic losses, reflection in the waveguide to CPS transition and diode coupling losses. Due to these losses the power at the diodes will be lower than at the output of the coupler. In order to obtain an even improved match between predicted and measurements higher LO powers would be required.

For a sub-harmonic mixer realised in waveguide the isolation between the IF, LO and RF signals is high due to the natural waveguide cut-off. However, for the EBG environment this characteristic is solely dependent on the successful implementation of the EBG material and the design of the filters and circuitry. Therefore care has to be taken to ensure the correct interpretation of the measurement results. For example in an open structure circuit there is the well know problem of the RF circuit acting as an antenna at the IF frequency and thereby allowing the low noise amplifier chain to see the hot and cold load used when measuring the mixer's RF response. In this instance the resulting variation of IF power with load temperature could be misinterpreted as mixing occurring at the RF. For this design, presence of this effect was ruled out by carrying out the Y-factor measurement in the absence of LO power and whilst varying diode bias to vary the terminating impedance of the IF chain, no drop in IF power was observed.

Another potential area of uncertainty is that mixing can occur at the LO frequency if the natural balance of the anti-series diode pair is not sufficiently close for fundamental mixing to be cancelled. For this design this is an area of greater uncertainty, as whilst the balance of the diodes at DC was excellent this may not necessarily be the case at the RF or LO. In fact to achieve optimum mixing response at certain frequencies it was necessary to apply a DC bias as shown in Figure 6.18 and explained previously.

In order to check if there was some harmonic mixing response the Y-Factor measurement was carried out placing a dicroic plate which filters out frequencies lower than 200 GHz. If the response of the mixer were purely subharmonic, the noise temperature measured should in theory not change. In practice, there will be some losses associated to the filter that will decrease the Y-factor.

The used filter is based on a hexagonal array of circular holes drilled in a 2.275 mm thick gold plate. The radius of the holes is 0.46 mm and its separation 1 mm. The predicted response of this filter under normal incidence is presented in Figure 6.21, showing insertion losses lower than 0.8 dB at RF

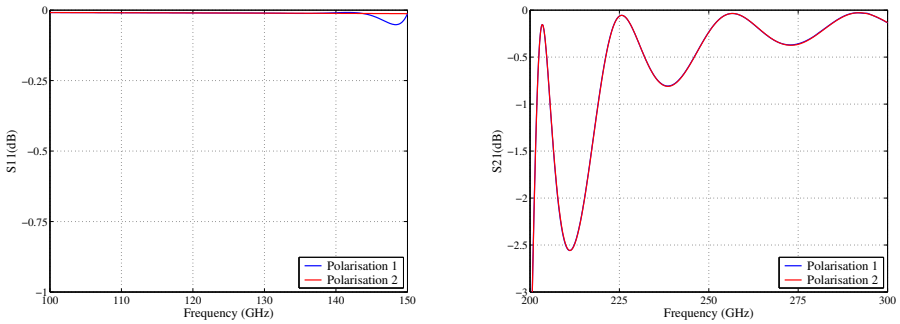

(a) (b)

Figure 6.21: Predicted performance of the dicroic high-pass filter at (a) LO and (b) RF frequencies.

frequencies. At LO frequencies the return loss is very close to 0 dB.

Unfortunately, this test could not be performed on the same mixer configuration, since the diodes were damaged and the mixer had to be rebuilt. The performance of this new mixer was much worse than the previous one. Its DSB noise temperature is shown in Figure 6.22(a) for different LO powers. Although the shape of the curve is similar to that previously obtained, the noise temperature is much higher. Several reasons could explain this worsening. Since the mixer was rebuilt, the circuits are damaged after its rebuilding or some of the contacts are lossier. Also the unbalance between the new diodes could be larger than between the first ones, either because their characteristics are different or their placement was more asymmetric.

When the filter is placed in between the antenna and the hot/cold load the noise temperature increased, as it is shown in Figure 6.22(b). The change in conversion loss is presented Figure 6.23. The conversion loss increases between 0 and 3 dB between 120 GHz and 135 GHz. For frequencies between 125 GHz and 130 GHz the degradation of the performance is lowest, which corresponds to the frequency range in which the change of noise temperature is smaller.

The change in both noise temperature and conversion loss shows that the mixer presents some harmonic mixing response. However, it is difficult to quantify how important it is when compared with the subharmonic mixing. Also, since the harmonic mixing is due to the unbalance of the configuration, it is not possible to asses if in the first measurements the low noise temperature was due to a more pure subharmonic mixing response.

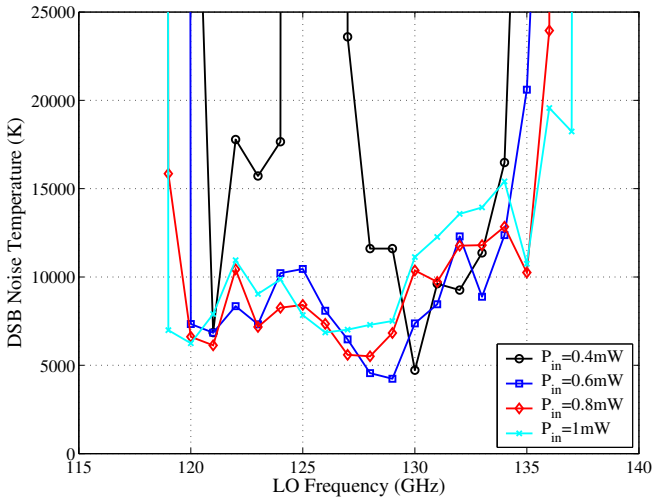

(a)

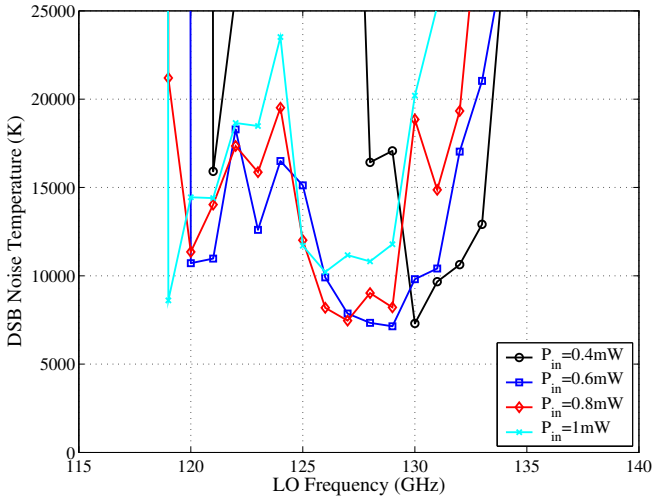

(b)

Figure 6.22: Measured DSB mixer noise temperature vs. LO frequency for the second fabricated configuration. (a) No high pass filter (b) Using a high-pass filter.

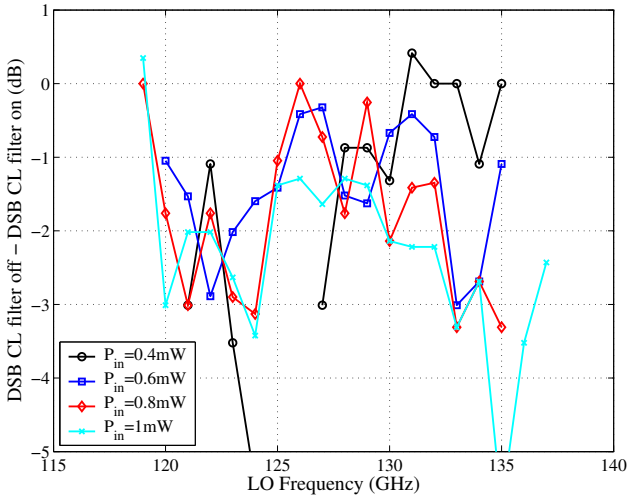

Figure 6.23: Measured DSB conversion loss degradation when the high pass filter is placed in front of the configuration.

The conclusion that can be drawn from these results is that the assembly of this mixer configuration is critical in order to assure the perfect balance of the diodes. Otherwise, since it is an open configuration the possibility exists to be combining both the harmonic and subharmonic mixer responses. This problem could be solved by using an antiparallel diode chip, so that the balance of the diode pair did not depend on the skill of the assembler.

Another improvement of the configuration would be to include a low-pass filter between the diodes and the antenna which blocked the LO frequency received by the antenna. However, the performance of the dipole antenna at LO frequencies is rather bad, since the woodpile is not acting as a reflector. This would imply that the LO frequency is being captured by the whole circuitry.

6.7 Comparison with conventional designs

In order to compare the performance of this mixer with conventional ones, measured subharmonic mixer results reported in the literature are summarised in Table 6.1. This table includes results close in frequency to the design frequency of the presented mixer. The results in [Möt00] and [Sie93] where

$RF(GHz)$	$T_{DSB}(K)$	$L_{DSB}(dB)$	**LO(mW)**	**Reference**
160	-	12	-	[Gau00]
182	1820	8.5	9	[Kor93]
183	450	4.2	2-3	[Moy98]
205	800	5.7	5.7	[Sie93]
215	1750	6.2	3.5	[Möt00]
240	490	-	3	[Meh98]
345	1650	-	7	[Orl03]

Table 6.1: Published performance of subharmonically pumped Schottky diode mixers.

given in terms of Single Side Band (SSB) performance. They were transformed into DSB values assuming: $T_{DSB} = T_{SSB}/2$ and $L_{DSB} = L_{SSB} - 3\,dB$.

Values of DSB noise temperature lower than $500\,K$ can be considered as state-of-the-art performance [Moy98]. The performance of the first measured prototype is, therefore, close to this value.

Chapter 7

Conclusions and guidelines for future research

In this chapter the main results obtained in this thesis will be summarised. Next some guidelines for future research will be provided.

7.1 Conclusions

In this thesis the use of EBG structures for millimetre-wave applications has been studied. In this frequency range, planar technologies suffer from losses due to surface wave excitation which worsens the antenna performance. One of the proposed solutions to this problem is the use of EBG substrates, in which no electromagnetic wave could propagate.

Although some preliminary demonstrations of the use of EBG technology for this application had already taken place, they were mainly proof-of-concept experiments. In this thesis a step forward is given, overcoming this initial status. In particular, several aspects related with the RF design of millimetre-wave receivers implementing EBG technology have being studied.

First, the main features of EBG structures when used as substrates for dipole antennas have been studied in Chapter 2. In particular both the radiation features and the input impedance of a dipole antenna placed on top of three different EBG structures have been studied. The selected EBG structures were the silicon and ZTT woodpile and the ZTT Fan structure. In all cases, the dipole antennas were printed on to a quartz substrate, as it would be in any real configuration.

With respect to the woodpile structure, the input impedance of a dipole antenna placed on top of it has been found to depend mainly on its orientation with respect to the first layer of bars. Dipoles placed parallel to these bars have very low input impedance, whereas the input impedance of those placed perpendicular to them is higher. In the case of the Fan structure a similar behaviour has been found, the input impedance being also in the in this case determined by the orientation with respect to the dielectric areas of the structure. These results seem to be linked to the phase of the reflected wave under plane wave incidence, which is close to 180 deg for the polarisation which show low input impedance and close to 0 deg for the other one.

The use of high dielectric constant materials presents two main advantages: increasing of the bandwidth of the gap and reducing the size of the structure. They would allow to have more compact and broader systems. However, in our studies when a high dielectric constant material, such as the ZTT, was used the size of the dipole antennas when placed on top of the studied EBG structures is not reduced accordingly, being the resonant lengths of the dipoles only slightly shorter.

Regarding the radiation patterns, they have also been found to depend very strongly on the orientation of the dipole with respect the woodpile bars. Configurations in which the dipole was parallel to the woodpile bars show more directive radiation patters than those configurations where the dipole is perpendicular to them. Also the radiation pattern is less dependent on the size of the woodpile structure for the parallel configurations. This behaviour is similar with both the ceramic and the silicon woodpile. In the case of Fan structure, the radiation patterns obtained are quite asymmetric and very dependent on the position of the dipole and its orientation.

More real configurations have been studied in Chapter 3, where the matching of dipole antennas fed by Coplanar Striplines placed on top of EBG structures is studied. Since the Coplanar Striplines present high characteristic impedance only those dipole configurations which have a large enough input resistance can be easily matched. In particular, and among the configurations that satisfy this condition, the "perpendicular solid-solid" has been studied in the case of the silicon and ceramic woodpile and the configuration labelled as "perpendicular #1" in the case of Fan structure. In all cases the effect of the feeding lines on the radiation pattern of the configurations and their frequency dependence has been studied. Also the effect of the losses of the materials has been taken into account, being negligible due to the response in reflection of the EBG.

The main conclusion that can be extracted from Chapters 2 and 3 is that the radiation and matching features depend very strongly on the position and orientation of the dipole on top of the EBG structure. Based on this fact, a modification of the woodpile has been proposed in Chapter 4 which allows obtaining simultaneously good matching and an improved radiation pattern. The modification proposed, based on the displacement of the bars closer to the dipole is easy to implement since it only affects to the first layer of bars.

Based on the results obtained in the previous chapters a receiver configuration using a Schottky diode as detecting element has been designed in Chapter 5. The radiating element was a dipole antenna placed on top of a silicon woodpile at the "perpendicular solid-solid" symmetry position. This position was chosen since it showed the best compromise between radiation and matching features. The design process of the detector was based on the adjustment of the distance between the diode and the dipole and filter. The diode must be as close as possible to the dipole to not distort the radiation pattern. The distance from the filter to the diode is finally chosen to obtain the required embedding impedance. The radiation pattern of the configuration was measured, showing good agreement with predictions. Regarding the sensitivity of the configurations, the results obtained agree with our predictions. However, there are several uncertainties in these results, since the measurement technique, subharmonic mixing detection, was very dependent on the LO power levels and the diodes were not identical, which makes them difficult to compare.

In addition to this detector, a subharmonic mixer using EBG technology at 250 RF frequency has been presented in Chapter 6. The design was a combination of EBG and conventional technology, since the bandgap of the selected EBG structure, silicon woodpile, is not large enough so as to cover both frequency bands and allow for the use of an EBG waveguide. Therefore, conventional waveguide technology was used to guide the LO and a configuration using a dipole antenna on top of the woodpile was used as radiation element. The mixer was characterised showing good performance, with best DSB noise temperature of 938 K. However, since this design is an open configuration, harmonic mixing can be present at the output of the mixer. This problem, which is created by the unbalance of the diodes has been detected in our configuration.

7.2 Guidelines for future research

In this thesis dipole antennas on top of EBG structures have been studied. A logical continuation of this work would be to study other radiating elements with improved radiating features, such as double dipoles. Also the control of the radiation pattern by locally modifying the surface of the woodpile could be further study, extending it to other symmetry positions.

Since the features of a dipole on top of an EBG are determined by the EBG configuration, it would be advisable to continue studying other EBG structures which could lead to improved radiation or matching features.

One of the applications of this technology is the realisation of imaging arrays. Since the design of a detecting element based on EBG technology as been carried out in this thesis, the next logical step would be to design a whole imaging array using these elements as detectors.

With respect to the design of mixers using EBG technology, harmonic mixers seem to be more appropriate, in order to use the same EBG as substrate for the radiating elements and to create the LO waveguides. In this case the whole configuration could be built based on EBG technology. This type of configuration would need to accurately study the transition between the EBG waveguides and conventional waveguides and the way to allocate the diodes and extract the IF signal.

Appendix A

Input impedance and radiation pattern of a dipole antenna on top of a silicon woodpile

In this appendix the complete set of plots corresponding to the input impedance and the radiation pattern of a dipole antenna placed on top of a silicon woodpile are presented.

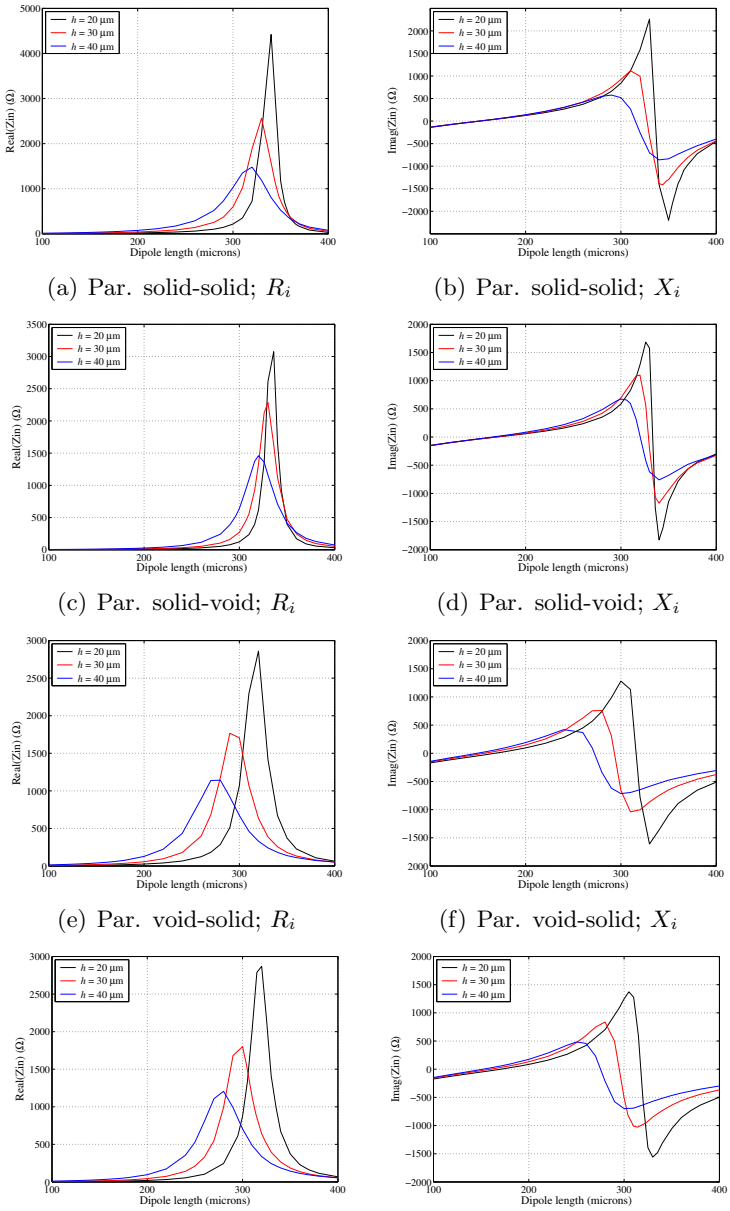

(a) Par. solid-solid; R_i

(b) Par. solid-solid; X_i

(c) Par. solid-void; R_i

(d) Par. solid-void; X_i

(e) Par. void-solid; R_i

(f) Par. void-solid; X_i

(g) Par. void-void; R_i

(h) Par. void-void; X_i

Figure A.1: Input impedance ($R_i + jX_i$) of a printed dipole placed on top of a silicon woodpile in the "parallel" symmetry positions as a function of its length and of the substrate thickness. $f = 500$ GHz.

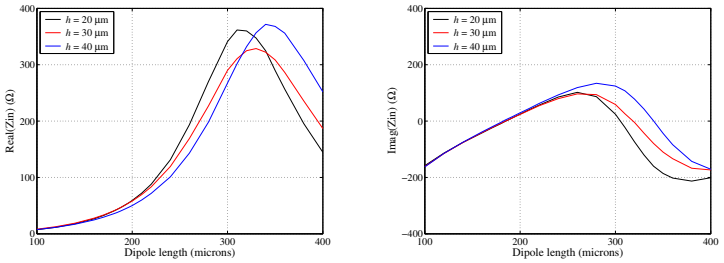

(a) Perp. solid-solid; R_i

(b) Perp. solid-solid; X_i

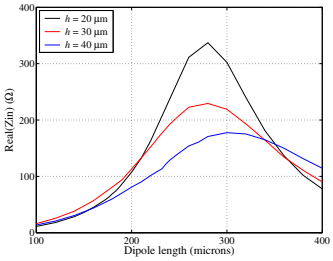

(c) Perp. solid-void; R_i

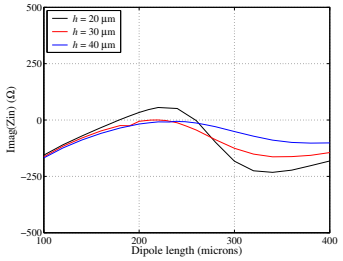

(d) Perp. solid-void; X_i

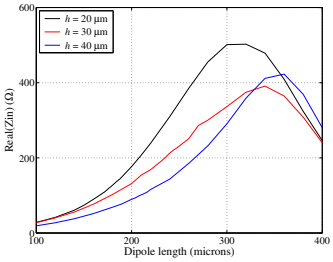

(e) Perp. void-solid; R_i

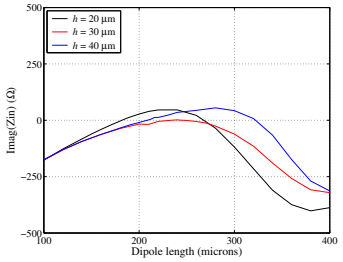

(f) Perp. void-solid; X_i

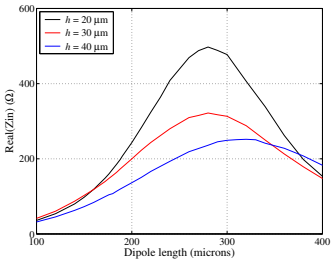

(g) Perp. void-void; R_i

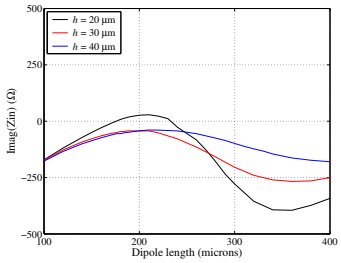

(h) Perp. void-void; X_i

Figure A.2: Input impedance ($R_i + jX_i$) of a printed dipole placed on top of a silicon woodpile in the "perpendicular" symmetry positions as a function of its length and of the substrate thickness. $f = 500$ GHz.

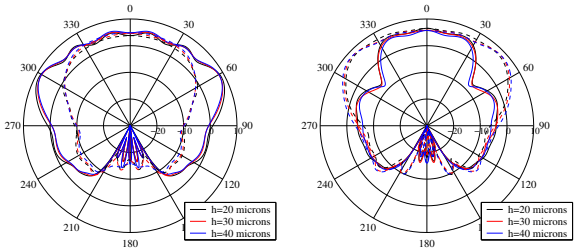

(a) Parallel solid-solid (b) Perp. solid-solid

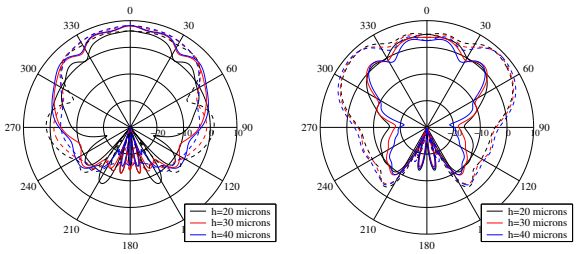

(c) Parallel solid-void (d) Perp. solid-void

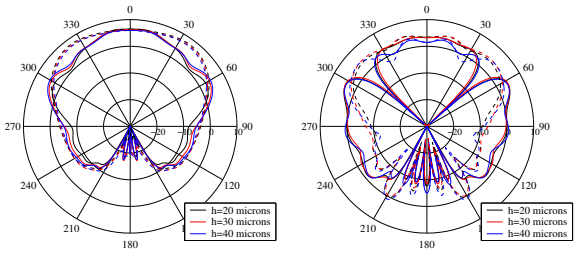

(e) Parallel void-solid (f) Perp. void-solid

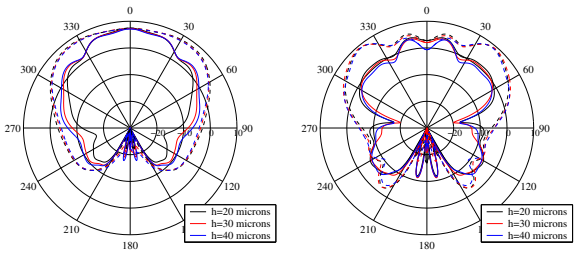

(g) Parallel void-void (h) Perp. void-void

Figure A.3: Radiation patterns of a printed dipole placed on top of the optimised silicon woodpile EBG structure as a function of the substrate thickness. $l_d = 250microns$*;* $f = 500$ *GHz. Solid line: E-Plane; Dashed line: H-Plane.*

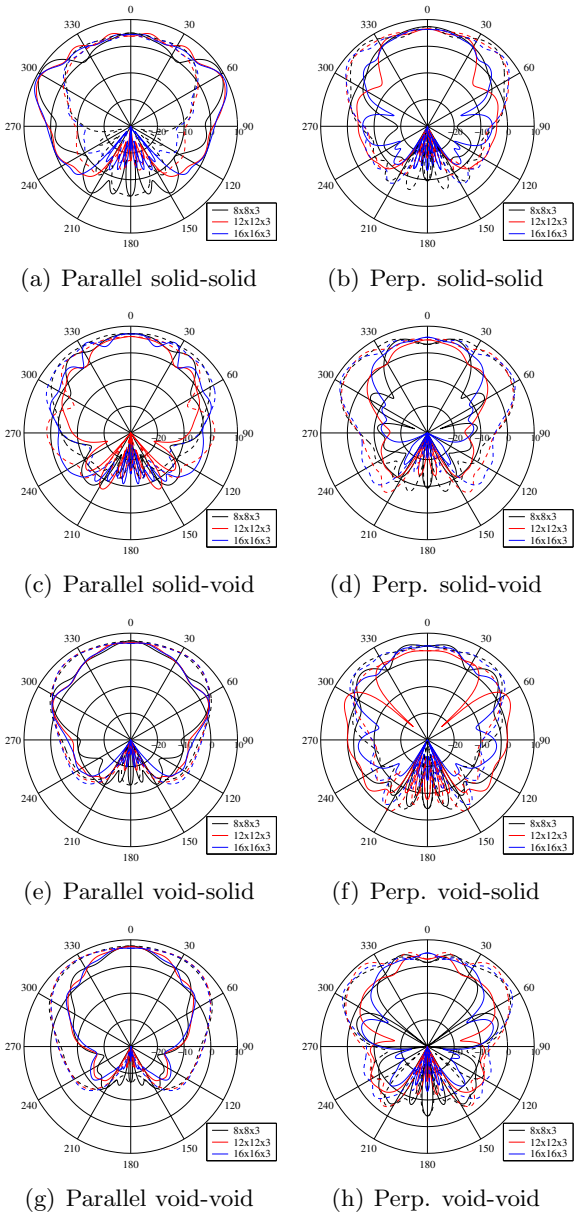

(a) Parallel solid-solid (b) Perp. solid-solid

(c) Parallel solid-void (d) Perp. solid-void

(e) Parallel void-solid (f) Perp. void-solid

(g) Parallel void-void (h) Perp. void-void

Figure A.4: Radiation patterns of a printed dipole placed on top of the optimised silicon woodpile EBG structure as a function of the number of periods of the woodpile structure. $l_{dip} = 250\,\mu m$*;* $h = 20\,\mu m$*;* $f = 500$ *GHz. Solid line: E-Plane; Dashed line: H-Plane.*

Appendix B

Input impedance and radiation pattern of a dipole antenna on top of a ZTT woodpile

In this appendix the complete set of plots corresponding to the input impedance and the radiation pattern of a dipole antenna placed on top of a ZTT woodpile are presented.

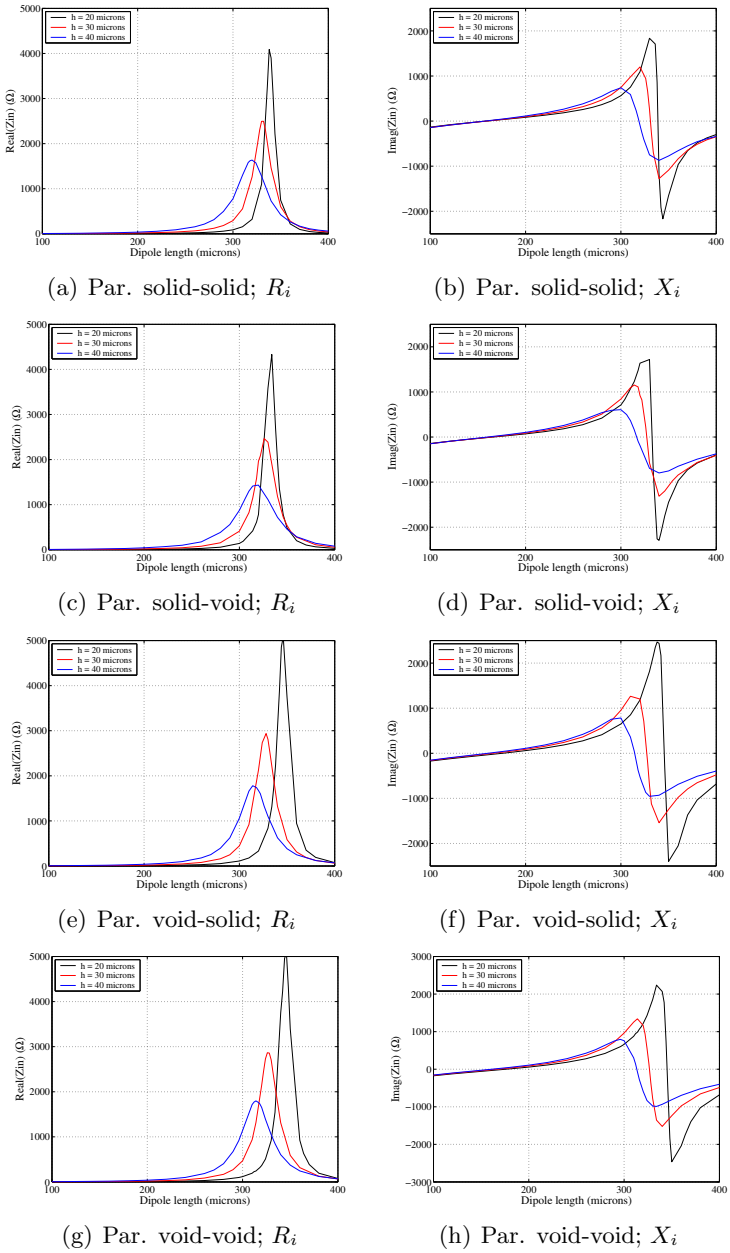

(a) Par. solid-solid; R_i (b) Par. solid-solid; X_i

(c) Par. solid-void; R_i (d) Par. solid-void; X_i

(e) Par. void-solid; R_i (f) Par. void-solid; X_i

(g) Par. void-void; R_i (h) Par. void-void; X_i

Figure B.1: Input impedance ($R_i + jXi$) of a printed dipole placed on top of a ZTT woodpile, $\epsilon_r = 37$, in the "parallel" symmetry positions as a function of its length and of the substrate thickness. $f = 500$ GHz.

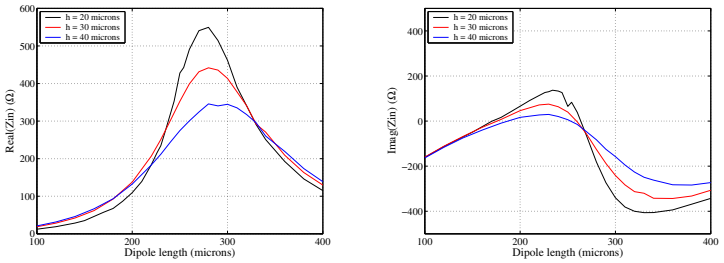

(a) Perp. solid-solid; R_i

(b) Perp. solid-solid; X_i

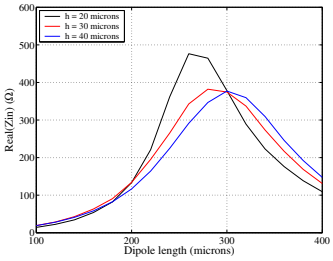

(c) Perp. solid-void; R_i

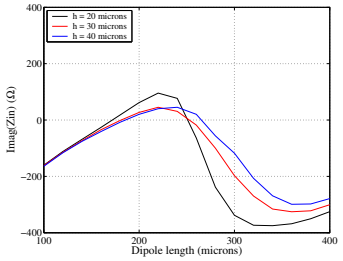

(d) Perp. solid-void; X_i

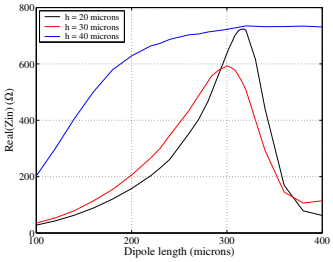

(e) Perp. void-solid; R_i

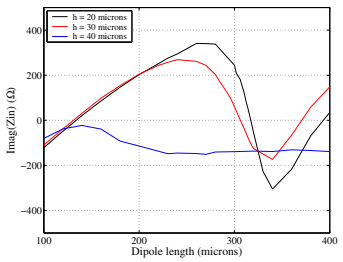

(f) Perp. void-solid; X_i

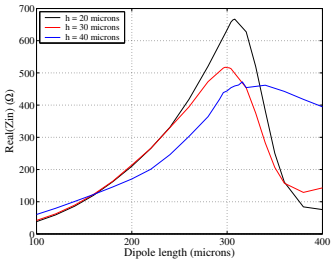

(g) Perp. void-void; R_i

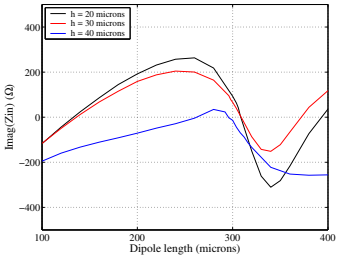

(h) Perp. void-void; X_i

Figure B.2: Input impedance ($R_i + jX_i$) of a printed dipole placed on top of a ZTT woodpile, $\epsilon_r = 37$, in the "perpendicular" symmetry positions as a function of its length and of the substrate thickness. $f = 500$ GHz.

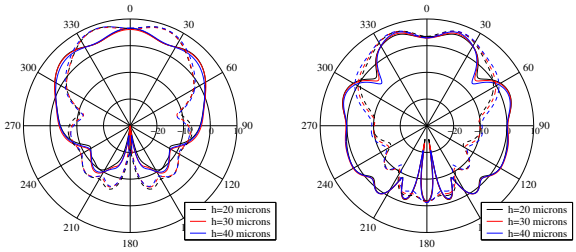

(a) Parallel solid-solid (b) Perp. solid-solid

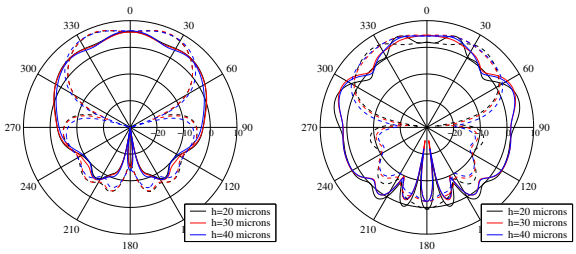

(c) Parallel solid-void (d) Perp. solid-void

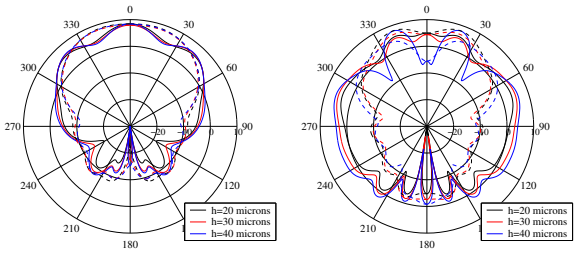

(e) Parallel void-solid (f) Perp. void-solid

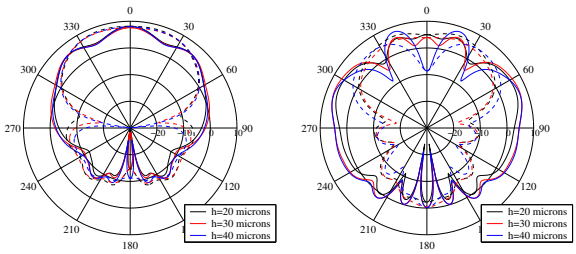

(g) Parallel void-void (h) Perp. void-void

Figure B.3: Radiation patterns of a printed dipole placed on top of the optimised ZTT woodpile as a function of the substrate thickness. $6 \times 6 \times 2$ *periods;* $l_d = 250\,\mu m$*;* $f = 500$ *GHz. Solid line: E-Plane; Dashed line: H-Plane.*

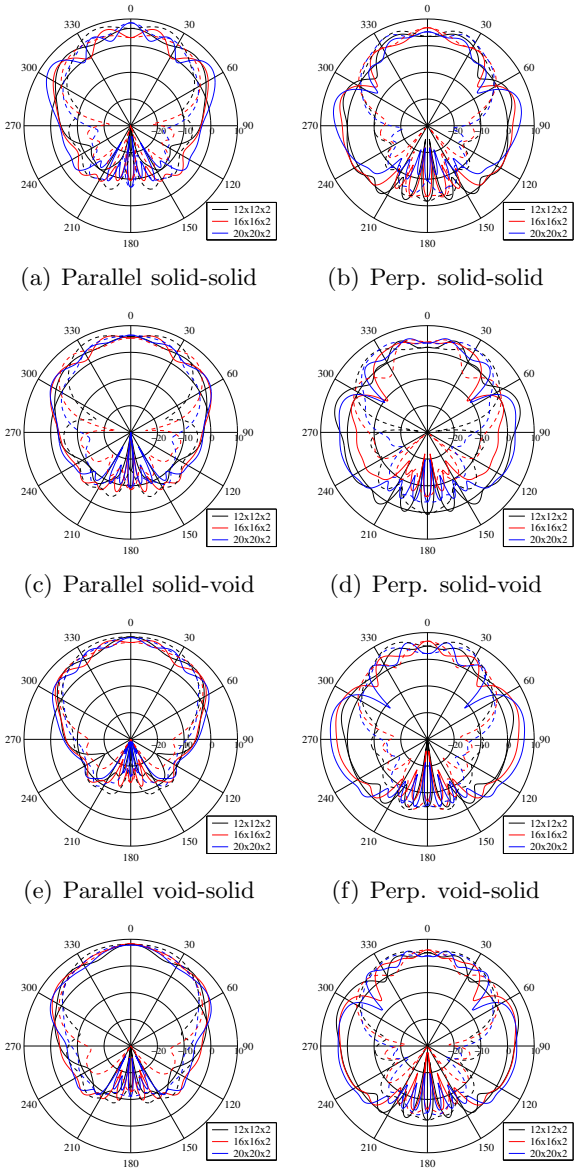

(a) Parallel solid-solid (b) Perp. solid-solid

(c) Parallel solid-void (d) Perp. solid-void

(e) Parallel void-solid (f) Perp. void-solid

(g) Parallel void-void (h) Perp. void-void

Figure B.4: Radiation patterns of a printed dipole placed on top of the optimised ZTT woodpile as a function of the number of periods of the EBG structure. $l_d = 250\,\mu m$*;* $h = 20\,\mu m$*;* $f = 500$ *GHz. Solid line: E-Plane; Dashed line: H-Plane.*

Appendix C

Input impedance and radiation pattern of a dipole antenna on top of a ZTT Fan structure

In this appendix the complete set of plots corresponding to the input impedance and the radiation pattern of a dipole antenna placed on top of a ZTT Fan EBG structure are presented.

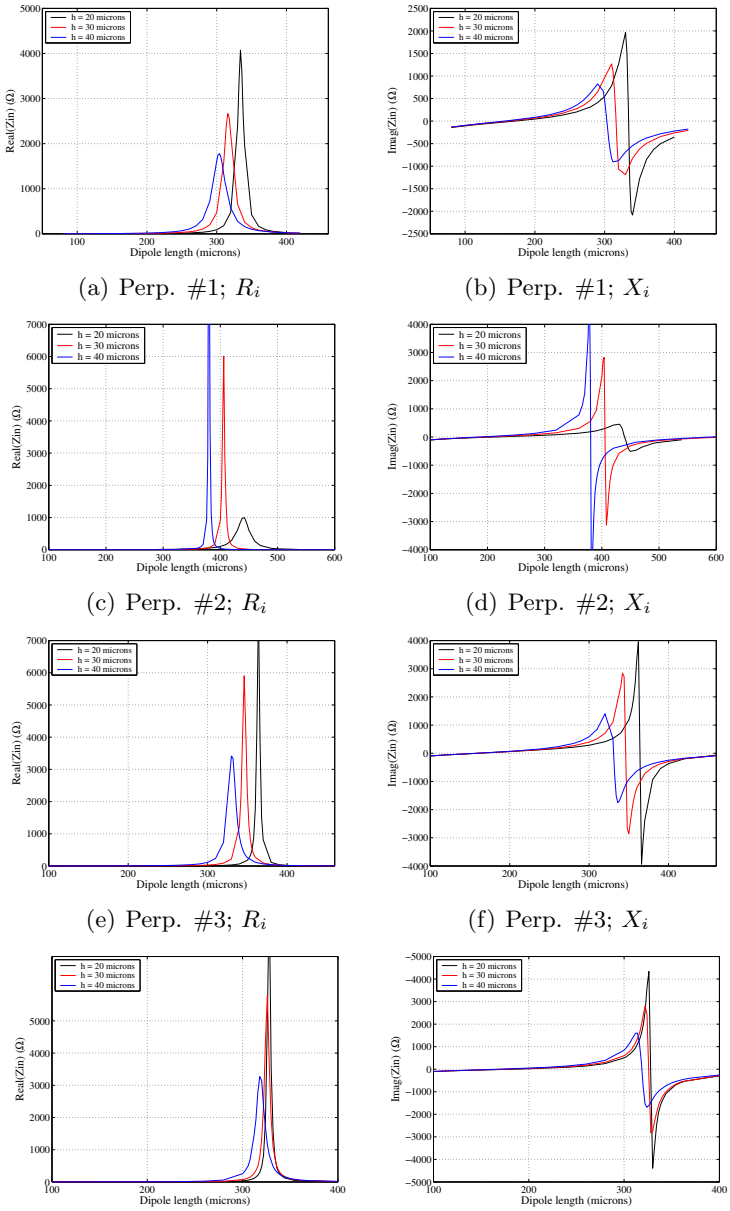

(a) Perp. #1; R_i (b) Perp. #1; X_i

(c) Perp. #2; R_i (d) Perp. #2; X_i

(e) Perp. #3; R_i (f) Perp. #3; X_i

(g) Perp. #4; R_i (h) Perp. #4; X_i

Figure C.1: Input impedance ($R_i + jXi$) of a printed dipole placed on top of Fan EBG structure, $\epsilon_r = 37$, in the "perpendicular" symmetry positions as a function of its length and of the substrate thickness. $f = 500$ GHz.

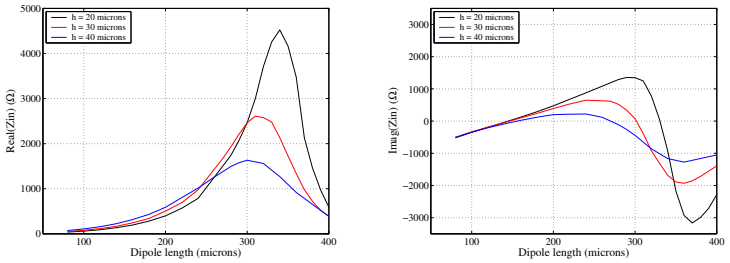

(a) Par. #1; R_i (b) Par. #1; X_i

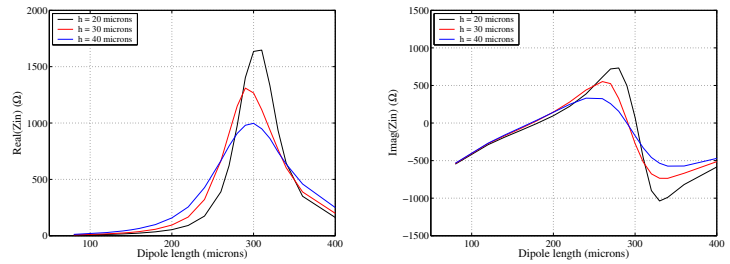

(c) Par. #2; R_i (d) Par. #2; X_i

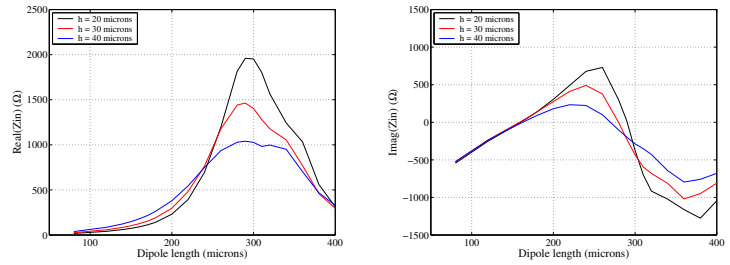

(e) Par. #3; R_i (f) Par. #3; X_i

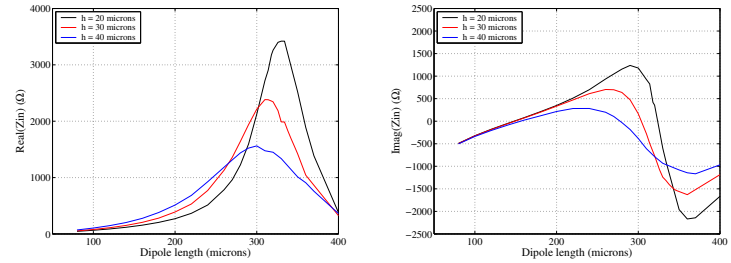

(g) Par. #4; R_i (h) Par. #4; X_i

Figure C.2: Input impedance ($R_i + jXi$) of a printed dipole placed on top of Fan EBG structure, $\epsilon_r = 37$, in the "parallel" symmetry positions as a function of its length and of the substrate thickness. $f = 500$ GHz.

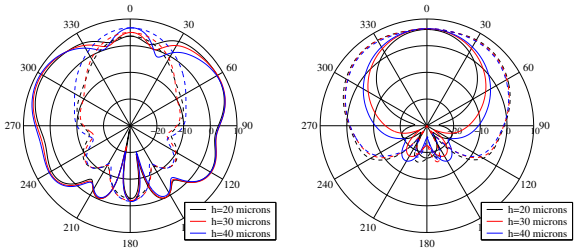

(a) Par. #1 (b) Perp. #1

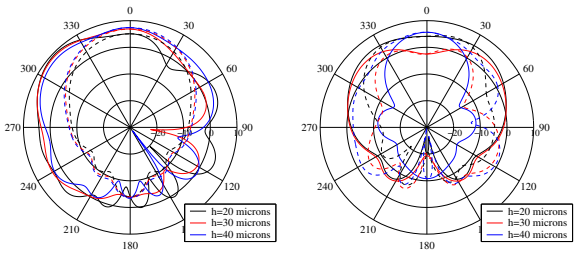

(c) Par. #2 (d) Perp. #2

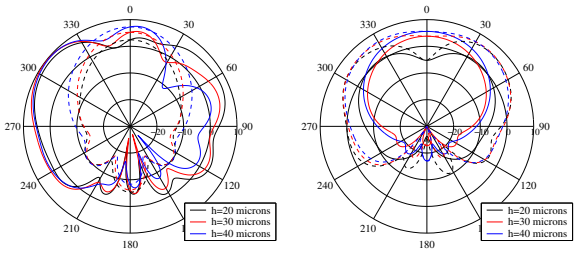

(e) Par. #3 (f) Perp. #3

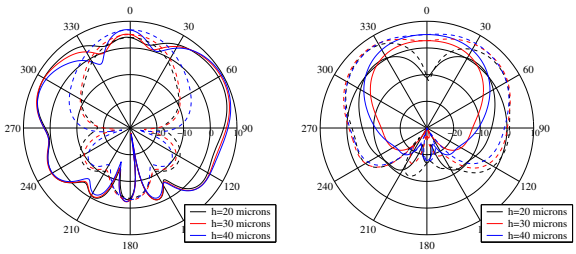

(g) Par. #4 (h) Perp. #4

Figure C.3: Radiation pattern of a dipole placed on top of Fan EBG structure. $l = 250\,\mu m$*;* $f = 500$ *GHz as a funtion of the quartz substrate thickness. Solid line: E-Plane; Dashed line: H-Plane.*

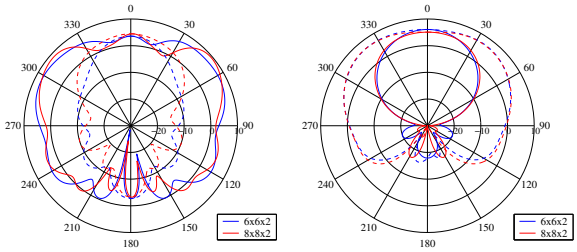

(a) Par. #1

(b) Perp. #1

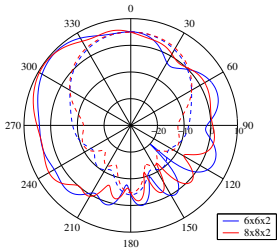

(c) Par. #2

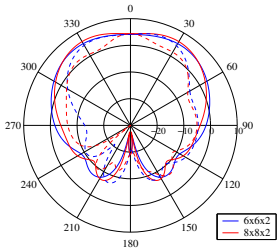

(d) Perp. #2

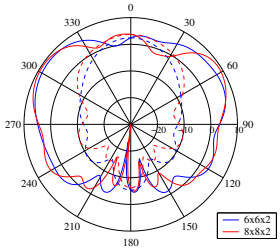

(e) Par. #3

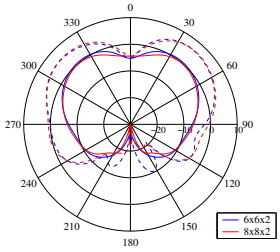

(f) Perp. #3

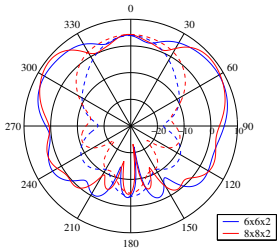

(g) Par. #4

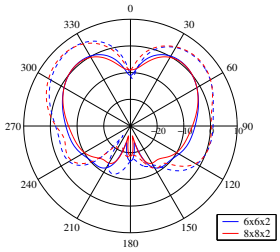

(h) Perp. #4

Figure C.4: Radiation pattern of a dipole placed on top of Fan's EBG structure as function of the number of periods of the EBG structure. $h = 20\,\mu m$*;* $f = 500$ *GHz. Solid line: E-Plane; Dashed line: H-Plane.*

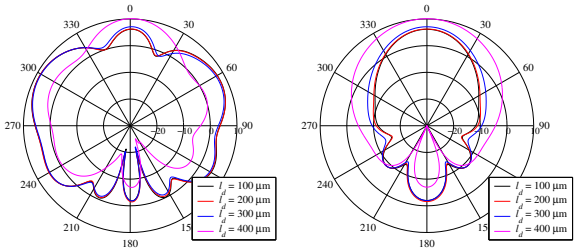

(a) Par. #1; E-Plane (b) Par. #1; H-Plane

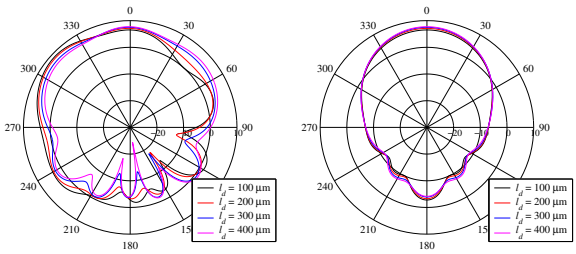

(c) Par. #2; E-Plane (d) Par. #2; H-Plane

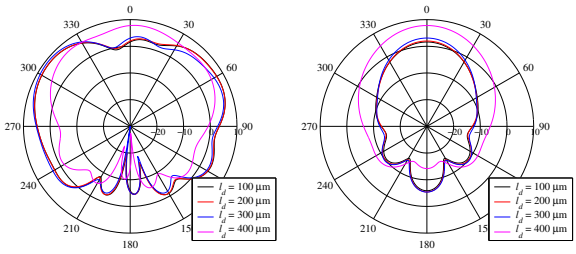

(e) Par. #3; E-Plane (f) Par. #3; H-Plane

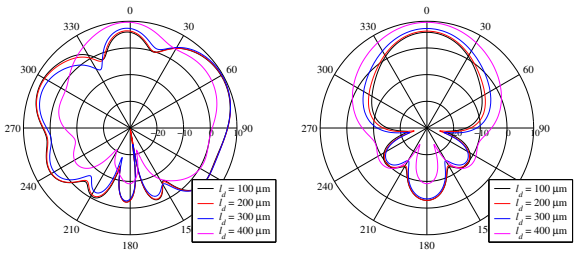

(g) Par. #4; E-Plane (h) Par. #4; H-Plane

Figure C.5: Radiation pattern of a dipole placed on top of Fan's EBG structure at the "parallel" symmetry positions as function of the length of the dipole. $h = 20\,\mu m$*;* $f = 500$ *GHz.*

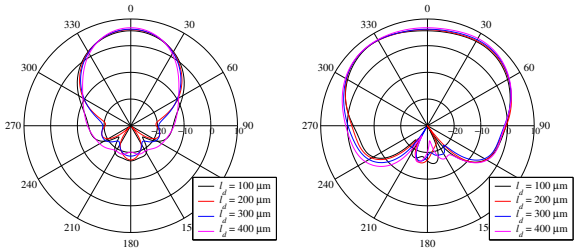

(a) Perp. #1; E-Plane (b) Perp. #1; H-Plane

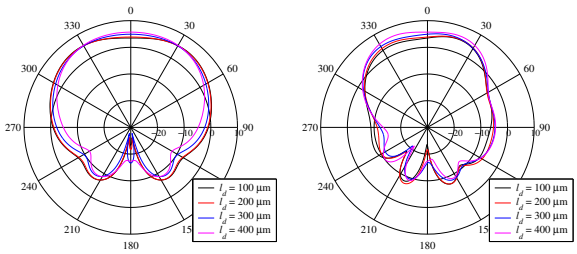

(c) Perp. #2; E-Plane (d) Perp. #2; H-Plane

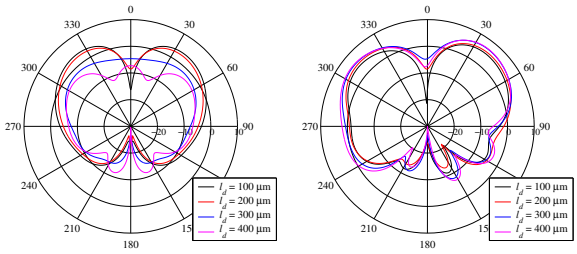

(e) Perp. #3; E-Plane (f) Perp. #3; H-Plane

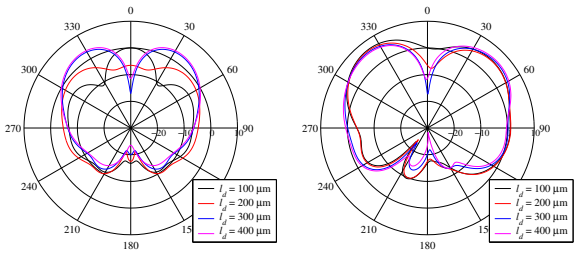

(g) Perp. #4; E-Plane (h) Perp. #4; H-Plane

Figure C.6: Radiation pattern of a dipole placed on top of Fan's EBG structure at the "perpendicular" symmetry positions as function of the length of the dipole. $h = 20\,\mu m$*;* $f = 500$ *GHz.*

Appendix D

Data sheet of the UMS DBES105a Schottky diode

united monolithic semiconductors

DBES105a

Flip-Chip Dual Diode

GaAs Diode

Description

The DBES105a is a dual Schottky diode based on a low cost 1µm stepper process including a bump technology. The parasitic inductances are reduced and result in a very high operating frequency.

This flip-chip dual diode has been designed for high performance mixer applications.

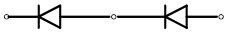

Main Features

- High cut-off frequencies : 3THz
- High breakdown voltage : < -5V @ 20µA
- Good ideality factor : 1.2
- Low parasitic inductances
- Low cost technology
- Dimensions : 0.53 x 0.23 x 0.1mm

Main Characteristics

Tamb. = 25°C

Symbol	Parameter	Typ	Unit
Wu	Gate Width	5	µm
Fco	Cut-off frequency	3	THz
n	Ideality factor	1.2	
BVak	Anode-cathode break-down voltage	< -5	V

ESD Protection : Electrostatic discharge sensitive device. Observe handling precautions !

United Monolithic Semiconductors S.A.S.
Route Départementale 128 - B.P.46 - 91401 Orsay Cedex France
Tel. : +33 (0)1 69 33 03 08 - Fax : +33 (0)1 69 33 03 09

DBES105a

Flip-Chip Dual Diode

Equivalent Circuit

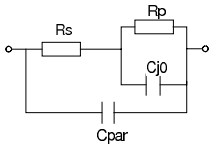

Rs(Ω)	Cjo(fF) (0V)	Cpar(fF)	Fco(THz)
4.4	9.5	5.8	2.4

Fco = 1/(2π Rs [Cpar + Cjo])
Rp can be neglected

Absolute Maximum Ratings (1)

Tamb. = 25°C

Symbol	Parameter	Typ. values	Unit
Vak	Reverse anode-cathode voltage	-5	V
Iak	Forward anode-cathode current	10	mA

(1) Operation of this device above anyone of these parameters may cause permanent damage.

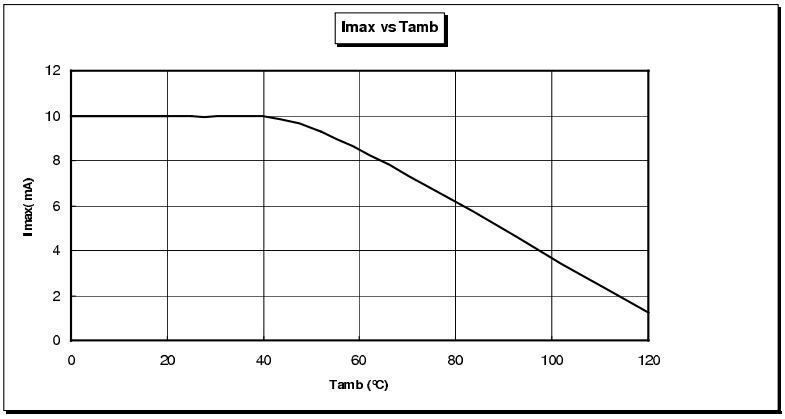

Route Départementale 128 , B.P.46 - 91401 ORSAY Cedex - FRANCE
Tel.: +33 (0)1 69 33 03 08 - Fax : +33 (0)1 69 33 03 09

Flip-Chip Dual Diode **DBES105a**

Typical DC Measurements

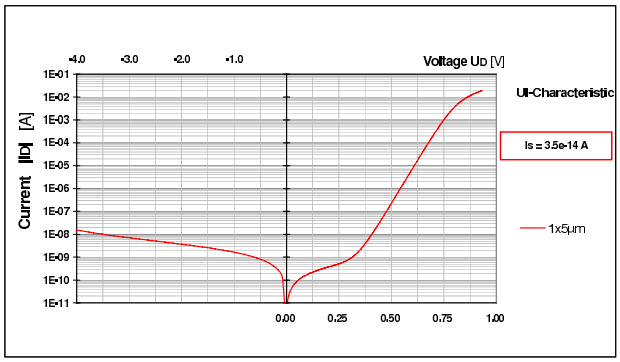

Typical On-Wafer Measurements

Bias Conditions Vak = 0V

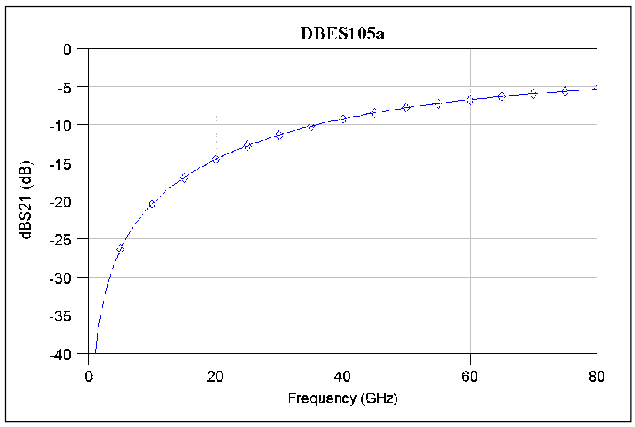

Route Départementale 128 , B.P.46 - 91401 ORSAY Cedex - FRANCE
Tel.: +33 (0)1 69 33 03 08 - Fax : +33 (0)1 69 33 03 09

DBES105a

Flip-Chip Dual Diode

Mechanical data

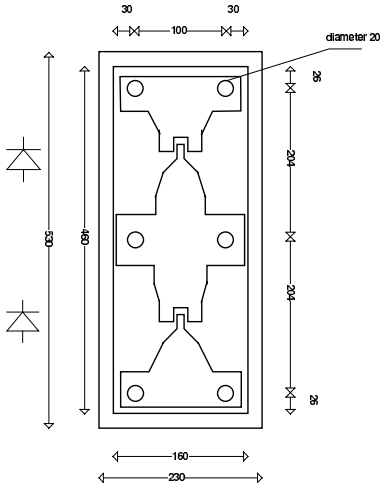

Dimensions in µm

Dimensions: 230 ± 35 x 530 ± 35 µm
Thickness= 100µm ± 10 µm

Ordering Information

Chip form : DBES105a-99F/00

Route Départementale 128 , B.P.46 - 91401 ORSAY Cedex - FRANCE
Tel.: +33 (0)1 69 33 03 08 - Fax : +33 (0)1 69 33 03 09

Bibliography

[Ale83] N.G. Alexopoulos, P.B. Katehi and D.B. Rutledge, "Substrate optimisation for integrated circuit antennas.", *IEEE Trans. Microwave Theory Tech.*, vol. 31, no. 7, pp. 550–557, Jul. 1983.

[Azc03] L. Azcona, B.J.E. Alderman, P.G. Huggard, R. Gonzalo, B. Martínez, I. Ederra, C. Del Río, B. de Hon, M. van Beurden, L. Marchand and P. de Maagt. "Micromachined electromagnetic bandgap crystals as antenna substrates for a 500 GHz imaging array." *Proc. 4th round table on Micro/Nano Technologies for Space*. ESTEC, Noordwijk, The Netherlands, May 2003.

[Azc04] L. Azcona, B.E.J. Alderman, P.G. Huggard, R. Gonzalo, B. Martínez, I. Ederra, C. del Río, B. P. de Hon, M. C. van Beurden, L. Marchand and P. de Maagt. "Manufacture of wide bandwidth 3-D EBG crystals for sub-millimetre antenna substrates." *Proc. 27th ESA Antenna Technology Workshop on Innovative Periodic Antennas: Electromagnetic Bandgap, Left-handed Materials, Fractal and Frequency Selective Surfaces*. Santiago de Compostela, Spain, Mar. 9-11 2004.

[Bal97] C.A. Balanis. *Antenna theory: analysis and design*. John Willey & Sons, 1997.

[Bis01] R. Biswas, E. Ozbay, B. Temelkuran, M. Bayindir and M. M. Sigalas, "Exceptionally directional sources with photonic-bandgap crystals.", *J. Opt. Soc. Am. B*, vol. 18, no. 11, pp. 1684–1689, Nov. 2001.

[Bri46] L. Brillouin. *Wave propagation in periodic structures*. New York:Dover, 1946.

[Bro93] E.R. Brown, C.D. Parker and E. Yablonovitch, "Radiation properties of a planar antenna on a photonic-crystal substrate.", *J. Opt. Soc. Am. B*, vol. 10, no. 2, pp. 404–407, Feb. 1993.

[Bro94] E.R. Brown, C.D. Parker and O.B. McMahon, "Effect of surface composition on the radiation pattern from a photonic-crystal planar-dipole antenna.", *Appl. Phys. Lett.*, vol. 64, no. 24, pp. 3345–3347, Jun. 13 1994.

[Bro96] E.R. Brown and O.B. McMahon, "High zenithal directivity from a dipole antenna on a photonic crystal.", *Appl. Phys. Lett.*, vol. 68, pp. 1300–1302, 1996.

[Bur04] G. Burns, I. Thayne and J.M. Arnold. "Inprovement of planar antenna efficiency when integrated with a millimetre-wave planar antennas with photonic crystal." *Proc. 27th ESA Antenna Technology Workshop on Innovative Periodic Antennas: Electromagnetic Bandgap, Left-handed Materials, Fractal and Frequency Selective Surfaces*. Santiago de Compostela, Spain, Mar. 9-11 2004.

[Büt93] T. Büttgenbach, "An improved solution for integrated array optics in quasioptical mm and submm receivers: the hybrid antenna.", *IEEE Trans. Microwave Theory Tech.*, vol. 41, no. 10, pp. 1750–1761, Nov. 1993.

[Cha04] R. Chantalat, T. Monédière, M. Thevènot, B. Jecko and P. Dumond. "Multi-beam reflector antenna with interlaced focal feeds by using a 1-D dielectric EBG resonator." *Proc. 27th ESA Antenna Technology Workshop on Innovative Periodic Antennas: Electromagnetic Bandgap, Left-handed Materials, Fractal and Frequency Selective Surfaces*. Santiago de Compostela, Spain, Mar. 9-11 2004.

[Che02] C. Cheype, C. Serier, M. Thevènot, T. Monédière, A. Reineix and B. Jecko, "An electromagnetic bandgap resonator antenna.", *IEEE Trans. Antennas Propagat.*, vol. 50, no. 9, pp. 1285–1290, Sep. 2002.

[Cra03] D.A. Crawley, C. Longbottom, V.P. Wallace, B.E. Cole, D.D. Arnone and M. Pepper, "Three dimensional terahertz pulse imaging of dental tissue.", *J. Biomedical Opt.*, vol. 8, p. 303, 2003.

[dM03] P.J.I. de Maagt, R. Gonzalo, Y.C. Vardaxoglou and J.-M. Baracco, "Electromagnetic bandgap antennas and components for microwave and (sub)millimeter wave applications.", *IEEE Trans. Antennas Propagat.*, vol. 51, no. 10, pp. 2667–2677, Oct. 2003.

[Ede03a] I. Ederra, R. Gonzalo, C.M. Mann and P. de Maagt. "(Sub)mm-wave components and subsystems based on EBG technology." *Proc. 2003 IEEE AP-S Int. Symp.*. Columbus, Ohio, USA, Jul. 2003.

[Ede03b] I. Ederra, F. van de Water, A. Laisne, C.M. Mann, P. de Maagt, G. McBride, D. Castiglione, A. McCalden, L. Deias, J.P. O'Neill, J. Teniente Vallinas, D. Haskett, D. Jenkins, A. Zinn, M. Ferlet and R. Edeson. "EBG millimetre-wave components design." *Proc. of the 3rd ESA Workshop on Millimetre Wave Technology and Applications: circuits, systems, and measurement techniques*, pp. 129–134. Espoo, Finland, May 21-23 2003.

[Ede04] I. Ederra, R. Gonzalo, B. Martínez, C. del Río, L. Azcona, B.E.J. Alderman, P.G. Huggard, B. P. de Hon, M. C. van Beurden, L. Marchand and P. de Maagt. "Sub-millimetre wave imaging array configurations using EBG technology." *Proc. 27th ESA Antenna Technology Workshop on Innovative Periodic Antennas: Electromagnetic Bandgap, Left-handed Materials, Fractal and Frequency Selective Surfaces*. Santiago de Compostela, Spain, Mar. 9-11 2004.

[Fan94] S. Fan, P.R. Villeneuve, R.D. Meade and J. D. Joannopoulos, "Design of three-dimensional photonic crystals at submicron length-scales.", *Appl. Phys. Lett.*, vol. 65, no. 11, pp. 1466–1468, 1994.

[Fil93] D.F. Filipovic, S.S. Gearhart and G.M. Rebeiz, "Double-slot antennas on extended hemispherical and elliptical silicon dielectric lenses.", *IEEE Trans. Microwave Theory Tech.*, vol. 41, no. 10, pp. 1738–1749, Oct. 1993.

[Gau00] G.P. Gauthier, J.P. Raskin and G.M. Rebeiz, "A 140-170 low-noise uniplanar subharmonic Schottky receiver.", *IEEE Trans. Microwave Theory Tech.*, vol. 48, no. 8, pp. 1416–1419, Aug. 2000.

[Gon99] R. Gonzalo, P.J.I. de Maagt and M. Sorolla., "Enhanced patch antenna performance by suppressing surface waves using pho-

tonic band-gap structures.", *IEEE Trans. Microwave Theory Tech.*, vol. 47, no. 11, pp. 2131–2138, Nov. 1999.

[Gon01] R. Gonzalo, I. Ederra, C.M. Mann and P.J.I. de Maagt, "Radiation properties of terahertz dipole antenna mounted on photonic crystal.", *Electron. Lett.*, vol. 37, no. 10, pp. 613–614, May 10 2001.

[Gon02] R. Gonzalo, B. Martínez, C.M. Mann, H. Pellemans, P. Haring Bolivar and P.J.I. de Maagt, "A low cost fabrication technique for symmetrical and asymmetrical layer by layer photonic crystal at submillimeter-wave frequencies.", *IEEE Trans. Microwave Theory Tech.*, vol. 50, no. 10, pp. 2384–2392, Oct. 2002.

[HB03] P. Haring-Bolivar, M. Bucherseifer, J. Gómez-Rivas, R. Gonzalo, I. Ederra, A.L. Reynolds, M. Holker and P. de Maagt, "Measurement of the dielectric constant and loss tangent of high dielectric-constant materials at terahertz frequencies.", *IEEE Trans. Microwave Theory Tech.*, vol. 51, no. 4, pp. 1062–1066, Apr. 2003.

[Ho94] K.M. Ho, C.T. Chan, C. Soukoulis, R. Biswas and M. Sigalas, "Photonic band gaps in three dimensions: New layer-by-layer periodic structure.", *Solid St. Comm.*, vol. 89, p. 413, 1994.

[Joa95] J.D. Joannopoulus, R.D. Meade and J.N. Finn. *Photonic Crystals: Molding the flow of light*. Princeton University Press, 1995.

[Joh87] S. John, "Strong localization of photons in certain disordered dielectric superlattices.", *Phys. Rev. Lett.*, vol. 58, no. 8, pp. 2486–2489, 1987.

[Joh00] S.G. Johnson and J.D. Joannopoulos, "Three-dimensionally periodic dielectric layered structure with omnidirectional band gap.", *Appl. Phys. Lett.*, vol. 77, pp. 3490–3492, Nov. 2000.

[Kan99] N. Kaneda, Y. Qian and T. Itoh. "A broadband microstrip-to-waveguide transition using quasi-Yagi antenna." *Proceedings of the IEEE MTT-S International Microwave Symposium*, vol. 4, pp. 1431–1434. Anaheim, CA, USA, Jun. 1999.

[Ker79] A.R. Kerr, "Noise and loss in balanced and subharmonically pumped mixers: Part i - theory & part ii - application.", *IEEE Trans. Microwave Theory Tech.*, vol. 27, no. 12, Dec. 1979.

[Kes96] M.P. Kesler, J.G. Maloney, B.L. Shirley and Smith G.S., "Antenna design with the use of photonic band-gap materials as all-dielectric planar reflectors.", *Microwave Opt. Technol. Lett.*, vol. 11, no. 4, pp. 169–174, Mar. 1996.

[Kor93] B.K. Kormanyos, P.H. Ostdiek, W.L. Bishop, T.W. Crowe and G.M. Rebeiz, "A planar wideband 80-200 GHz subharmonic receiver.", *IEEE Trans. Microwave Theory Tech.*, vol. 41, no. 10, pp. 1730–1737, Oct. 1993.

[Kra88] J.D. Kraus. *Antennas*. McGraw-Hill, 1988.

[Lai03] A. Laisné, "Harmonic balance simulation of a diode rectifier.", *Internal report ESA contract ITT AO/1-3760/01/NL/ND*, 2003.

[Let03] A.H. Lettington, D. Dunn, M. Attia and I.M. Blankson, "Passive millimetre-wave imaging architectures.", *J. Opt. A: Pure Appl. Opt.*, vol. 5, pp. S103–S110, 2003.

[Leu97] W.Y. Leung, R. Biswas and K.M. Ho, "Slot antennas on photonic band gap crystals.", *IEEE Trans. Antennas Propagat.*, vol. 45, no. 10, pp. 1569–1570, Oct. 1997.

[Maa93] S.A. Maas. *Microwave mixers*. Artech House, 1993.

[Man92] C.M. Mann. "A novel 183 subharmonic Schottky diode mixer." Ph.D. thesis, Queen Mary and Westfield College, University of London, 1992.

[Man03a] C.M. Mann, P. de Maagt, G. McBride, F. van de Water, A. Laisne, D. Castiglione, A. McCalden, L. Deias, J.P. O'Neill, J. Teniente Vallinas, I. Ederra, D. Haskett, D. Jenkins, A. Zinn, M. Ferlet and R. Edeson. "Silicon microfabrication of 3D terahertz waveguide and optical components." *Proc. of the 3rd ESA Workshop on Millimetre Wave Technology and Applications: circuits, systems, and measurement techniques*. Espoo, Finland, May 21-23 2003.

[Man03b] C.M. Mann, P.J.I. de Maagt, G. McBride, F. van de Water, D. Castiglione, A. McCalden, L. Deias, J.P. O'Neill, A. Laisne, J. Teniente Vallinas, I. Ederra, D. Haskett, D. Jenkins, A. Zinn, M. Ferlet and R. Edeson. "Microfabrication of 3D terahertz circuitry." *Proc. of*

the IEEE Int. Microwave Symp., pp. 129–134. Philadelphia, Pensilvania, USA, Jun. 11-13 2003.

[Mar04] B. Martínez. "3-D Electromagnetic Band Gap structures at millimetre wave frequencies: design, fabrication and measurements." Ph.D. thesis, Universidad P´ˇblica de Navarra, Pamplona, Spain, 2004.

[Meh98] I. Mehdi, S.M. Marazita, D.A. Humphrey, T.-H. Lee, R.J. Dengler, J.E. Oswald, A.J. Pease, S.C. Martin, W.L. Bishop, T.W. Crowe and P.H. Siegel, "Improved 240-GHz subharmonically pumped planar Schottky diode mixers for space-borne applications.", *IEEE Trans. Microwave Theory Tech.*, vol. 46, no. 12, pp. 2036–2042, Dec. 1998.

[Möt00] V.S. Möttönen, P. Piironen, J. Zhang, A.V. Räisänen, C.-I. Lin, A. Simon and H.L. Hartnagel, "Subharmonic waveguide mixer at 215 GHz utilizing quasivertical Schottky diodes.", *Microwave Opt. Technol. Lett.*, vol. 2, no. 27, pp. 93–97, 2000.

[Moy98] B.P. Moyna, C.M. Mann, B.N. Ellison, M.L. Oldfield, D.N. Matheson and T.W. Crowe. "Broadband space-qualified subharmonic mixers at 183 GHz with low local oscillator power requirements." *Proc. 2nd ESA Workshop on Millimetre Wave Technology and Applications: Antennas, Circuits and Systems*. Espoo, Finland, May 1998.

[Net03] A. Neto, P. de Maagt and S. Maci, "Optimized basis functions for slot antennas excited by coplanar waveguides.", *IEEE Trans. Antennas Propagat.*, vol. 51, no. 7, pp. 1638–1646, Jul. 2003.

[Oli99] A.A. Oliner. "Periodic structures and photonic band-gap terminology: Historical perspectives." *Proc. 29th Eur. Microwave Conf*, pp. 295–298. Munich, Germany, Oct. 1999.

[Orl03] J.C. Orlhac and B. Thomas. "Design and characterization of a 330-350 GHz sub harmonically pumped mixer with circular RF waveguide based on Schottky barrier diodes." *Proceedings of the 3rd ESA Workshop on Millimetre Wave Technology and Applications: Circuits, Systems, and Measurement techniques*, pp. 623–628. Espoo, Finland, May 21-23 2003.

[Poz83] D.M. Pozar, "Considerations for millimeter wave printed antennas.", *IEEE Trans. Antennas Propagat.*, vol. 31, no. 9, pp. 740–747, Sep. 1983.

[Reb92] G.M. Rebeiz, "Millimetre-wave and terahertz integrated circuit antennas.", *Proc. IEEE*, vol. 80, no. 11, pp. 1748–1770, Nov. 1992.

[Rut82] D.B. Rutledge and M.S. Muha, "Imaging antenna arrays.", *IEEE Trans. Antennas Propagat.*, vol. 30, no. 4, pp. 535–540, Jul. 1982.

[Sie93] P.H. Siegel, R.J. Dengler, I. Mehdi, J.E. Oswald, W.L. Bishop, T.W. Crowe and R.J. Mattauch, "Measurements on a 215-GHz subharmonically pumped waveguide mixer using planar back-to-back airbridge Schottky diodes.", *IEEE Trans. Microwave Theory Tech.*, vol. 41, no. 11, pp. 1913–1921, Nov. 1993.

[SIE99a] "Special issue on electromagnetic crystal structures, design, synthesis and applications.", *IEEE Trans. Microwave Theory Tech.*, vol. 47, no. 11, Nov. 1999.

[Sie99b] D.F. Sievenpiper, L.J. Zhang, R.F.J. Broas, N.G. Alexopulous and E. Yablonovitch, "High-impedance electromagnetic surfaces with a forbidden frequency band.", *IEEE Trans. Microwave Theory Tech.*, vol. 47, pp. 2059–2074, 1999.

[Sig96] M.M. Sigalas, R. Biswas and K.M. Ho, "Theoretical study of dipole antennas on photonic band-gap materials.", *Microwave Opt. Technol. Lett.*, vol. 13, no. 4, pp. 205–209, Nov. 1996.

[Sig97] M.M. Sigalas, R. Biswas, Q. Li, D. Crounch, W. Leung, R. Jacobs-Woodbury, B. Lough, S. Nielsen, S. McCalmont, G. Tuttle and K.M. Ho, "Dipole antennas on photonic band-gap crystals- experiment and simulation.", *Microwave Opt. Technol. Lett.*, vol. 15, no. 3, pp. 153–158, Jun. 20 1997.

[Sig99] M.M. Sigalas, R. Biswas, K.M. Ho, W. Leung, G. Tuttle and D. Crounch, "The effect of photonic crystals on dipole antennas.", *Electromagnetics, Special issue: Theory and applications of photonic band-gap materials*, vol. 19, no. 3, pp. 291–303, May-June 1999.

[Sim01] R.N. Simons. *Coplanar waveguide circuits, components, and systems*. John Willey & Sons, 2001.

[Sin01] G.N. Sinclair, R.N. Anderton and R. Appleby, "Passive millimetre-wave concealed weapon detection.", *Proc. SPIE*, vol. 4232, pp. 142–151, 2001.

[SIQ93] "Special issue on quasi-optical techniques.", *IEEE Trans. Microwave Theory Tech.*, vol. 41, no. 10, Oct. 1993.

[SIQ02] "Special issue on electromagnetic crystal structures connected to the PECS-III conference.", *IEEE J. Quantum Electron.*, vol. 37, no. 7, Jul. 2002.

[Smi99] S.G. Smith, P.M. Kesler and J.G. Maloney, "Dipole antennas used with all-dielectric woodpile photonic bandgap reflectors: Gain, field patterns and input impedance.", *Microwave Opt. Technol. Lett.*, vol. 21, no. 3, pp. 191–196, May 5 1999.

[Söz94] H.S. Sözuer and J.P. Dowling, "Photonic band gap calculations for woodpile structures.", *J. Mod. Opt.*, vol. 41, p. 231, 1994.

[Tah83] R.S. Tahim, G.M. Hayashibara and K. Chang, "Design and performance of W-band broadband integrated circuit mixers.", *IEEE Trans. Microwave Theory Tech.*, vol. 31, no. 3, pp. 277–283, 1983.

[The99] M. Thevènot, C. Cheype, A. Reineix and B. Jecko, "Directive photonic-bandgap antennas.", *IEEE Trans. Microwave Theory Tech.*, vol. 47, no. 9, pp. 2115–2122, Sep. 1999.

[Ueh92] K. Uehara, K. Miyashita, K. Natsume, K. Hatakeyama and K. Mizumo, "Lens-coupled imaging array for the millimeter- and submillimeter-wave region.", *IEEE Trans. Microwave Theory Tech.*, vol. 40, no. 5, pp. 806–811, May 1992.

[vdV99] M.J.M. van der Vorst. "Integrated lens antennas for submillimetre wave applications." Ph.D. thesis, Eindhoven University of Technology, Eindhoven, The Netherlands, 1999.

[Woo03] R.M. Woodward, V.P. Wallace, D.D. Arnone, E.H. Linfield and M. Pepper, "Terahertz pulsed imaging of skin cancer in the time and frequency domain.", *J. Bio. Phys.*, vol. 29, pp. 257–261, 2003.

[Yab91] E. Yablonovitch, Gmitter T.J. and K. M Leung, "Photonic band structure: The face-centered-cubic case employing nonspherical atoms.", *Phys. Rev. Lett.*, vol. 67, p. 2295, 1991.

[Yan99] F.R. Yang, K.P. Yang, Y.X. Qian and T. Itoh, "A uniplanar compact photonic-bandgap (UC-PBG) structure and its applications for microwave circuits.", *IEEE Trans. Microwave Theory Tech.*, vol. 47, no. 8, Aug. 1999.

[Yan03] F. Yang and Y. Rahmat-Samii, "Reflection phase characterizations of the EBG ground plane for low profile wire antenna applications.", *IEEE Trans. Antennas Propagat.*, vol. 51, no. 10, pp. 2691–2703, Oct. 2003.

[Yuj03] L. Yujiri, M. Shoucri and P. Moffa, "Passive millimeter-wave imaging.", *IEEE Microwave Magazine*, vol. 4, no. 3, pp. 39–50, Sep. 2003.

List of Publications

Journal papers

1. P. Haring Bolívar, M. Brucherseifer, R. Gonzalo, **I. Ederra**, A. Reynolds, M. Holker and P. de Maagt, "Measurement of the dielectric constant and Loss Tangent of High Dielectric Constant Materials at Terahertz Frequencies", IEEE Transactions on Microwave Theory and Techniques, vol. 52, No. 4, pp. 1062-1067, April 2003

2. R. Gonzalo, **I. Ederra**, C.M. Mann and P. de Maagt, "Radiation properties of terahertz dipole antenna mounted on photonic crystal", Electronics Letters, Vol. 37, No 10, pp. 613-615, May 2001

Invited international conferences

1. **I. Ederra**, R. Gonzalo, Chris Mann, A. Moroz y P. de Maagt, "(Sub)mm-Wave Components and Subsystems based on EBG Technology", International Conference on Electromagnetics in Advanced Applications, ICEAA'03, Turn, Italy, Sept. 2003

2. **I. Ederra**, R. Gonzalo, Chris Mann, and P. de Maagt, "(Sub)mm-Wave Components and Subsystems based on PBG Technology", 2003 IEEE AP-S International Symposium and USNC/URSI National Radio Science Meeting, Columbus, Ohio, EEUU, June 2003

3. C. M. Mann, P. de Maagt, G. McBride, F. van de Water, A. Laisne, D. Castiglione, A. McCalden, L. Deias, J.P. O'Neill, J. Teniente Vallinas, **I. Ederra**, D. Hasket, D. Jenkins, A. Zinn, M. Ferlet and R. Edeson, "Microfabrication of 3D Terahertz Circuitry", IEEE International Microwave Symposium, Philadelphia, Pennsylvania, June 2003

4. P. de Maagt, B. Arredondo Conchillo, L. Minelli, **I. Ederra**, R. Gonzalo and A.L. Reynolds, "Photonic BandGap Antennas and Components for Microwave and (Sub)millimeter Wave Applications" XXVIIth General Assembly of the International Union of Radio Science, Maastricht, Holanda, August 2002

International conferences

1. B. de Hon, M. C. van Beurden, R. Gonzalo, B. Martínez, **I. Ederra**, C. del Río, L. Azcona, B. Alderman, P. G. Huggard, L. Marchand and P. de Maagt, "Domain Integral Equations for Electromagnetic Band-Gap Slab Simulations", 2004 URSI EMTS: Electromagnetic Symposium, Pisa, Italia, May 2004

2. **I. Ederra**, R. Gonzalo, B. Martínez, C. del Río, L. Azcona, B.E.J. Alderman, P.G. Huggard, B. P. de Hon, M.C. van Beurden, L. Marchand and P. de Maagt, "Sub-millimetre Wave Imaging Array Configurations using EBG Technology", 27th ESA Antenna Technology Workshop on Innovative Periodic Antennas: Electromagnetic Bandgap, Left-handed Materials, Fractal and Frequency Selective Surfaces, Santiago de Compostela, Spain, March 2004

3. L. Azcona, B.E.J. Alderman, P.G. Huggard, R. Gonzalo, B. Martínez, **I. Ederra**, C. del Río, B. P. de Hon, M.C. van Beurden, L. Marchand and P. de Maagt, "Manufacture of wide bandwidth 3-D EBG crystals for sub-millimetre antenna substrates", 27th ESA Antenna Technology Workshop on Innovative Periodic Antennas: Electromagnetic Bandgap, Left-handed Materials, Fractal and Frequency Selective Surfaces, Santiago de Compostela, Spain, March 2004

4. B. P. de Hon, M.C. van Beurden, R. Gonzalo, B. Martínez, **I. Ederra**, C. del Río, L. Azcona, B.E.J. Alderman, P.G. Huggard, L. Marchand and P. de Maagt, "A dedicated numerical technique for field simulations of antennas on electromagnetic band-gap substrates", 27th ESA Antenna Technology Workshop on Innovative Periodic Antennas: Electromagnetic Bandgap, Left-handed Materials, Fractal and Frequency Selective Surfaces, Santiago de Compostela, Spain, March 2004

5. L. Azcona, B. Alderman, P.G. Huggard, R. Gonzalo, B. Martínez, **I. Ederra**, C. Del Río, B. de Hon, M. Van Beurden, L. Marchand and P. De Maagt, "EBG technology for imaging arrays at the sub-mm range: designs, materials and precision micromachining techniques", Metamaterials for Microwave and (Sub) millimetre Wave applications: Photonic Bandgap and Double Negative Designs, Components and Experiments, London, UK, Nov. 2003

6. B. Alderman, L. Azcona, D. Matheson, P. Huggard, B. de Hon, M. van Beurden, B. Martínez, **I. Ederra**, C. Del Río, R. Gonzalo, L. Marchand and P. de Maagt, "Micromachined Electromagnetic Bandgap Crystals as Antenna Substrates for 500 GHz Imaging Arrays", 4th Round Table on Micro/Nano Technologies for Space, Noordwijk, The Netherlands, May 2003

7. P. de Maagt, C.M. Mann, G. McBride, F. van de Water, A. Laisne, D. Castiglione, A. McCalden, L. Deias, J.P. O'Neill, J. Teniente Vallinas, **I. Ederra**, D. Hasket, D. Jenkins, A. Zinn, M. Ferlet and R. Edeson, "Silicon microfabrication of 3D terahertz waveguide and optical components", 4th Round Table on Micro/Nano Technologies for Space, Noordwijk, The Netherlands, May 2003

8. **I. Ederra**, L. Azcona, R. Gonzalo, B.E.J. Alderman, P.G. Huggard, C.M. Mann, P. Haring-Bolívar and P. de Maagt, "Measurements of Sub-mm and mm-Wave Components and Subsystems based on EBG Technology", 3rd ESA Workshop on Millimetre Wave Technology and Applications, Espoo, Finland, May 2003

9. **I. Ederra**, F. van de Water, A. Laisne, C. M. Mann, P. de Maagt, G. McBride, D. Castiglione, A. McCalden, L. Deias, J.P. O'Neill, J. Teniente Vallinas, D. Hasket, D. Jenkins, A. Zinn, M. Ferlet and R. Edeson, "EBG Millimetre-wave Components Design", 3rd ESA Workshop on Millimetre Wave Technology and Applications, Espoo, Finland, May 2003

10. C.M. Mann, P. de Maagt, G. McBride, F. van de Water, A. Laisne, D. Castiglione, A. McCalden, L. Deias, J.P. O'Neill, J. Teniente Vallinas, **I. Ederra**, D. Hasket, D. Jenkins, A. Zinn, M. Ferlet and R. Edeson, "Silicon microfabrication of 3D terahertz waveguide and optical

components", 3rd ESA Workshop on Millimetre Wave Technology and Applications, Espoo, Finlandia, May 2003

11. R. Gonzalo, C. Sagaseta, **I. Ederra**, B. Martínez, H.P.M Pellemans, P. Haring Bolívar, C.M. Mann and P. De Maagt, "A 3-D Photonic Crystal used as Substrate in an Antenna Configuration at Sub-millimetre Wave Frequencies", ERC on Electromagnetic Crystal Structures, St. Andrews, UK, June 2001

12. R. Gonzalo, C. Sagaseta, **I. Ederra**, B. Martínez, H.P.M. Pellemans, P.H. Bolívar, C. Mann, P. de Maagt, "The effect of a Woodpile Photonic Cristal at Sub-Millimetre Wave Frequencis used as Substrate in a Dipole Configuration", 24th ESTEC Antenna Workshop on Innovative Periodic Photonic BandGap, Fractal and Frequency Selective Structures, ESA-ESTEC, Noordwijk, Holanda, May-June, 2001